Birgit Pichler, BSc.

Synthesis of PtFe/C Catalysts for the Oxygen Reduction Reaction in High-Temperature PEM Fuel Cells

MASTERARBEIT

zur Erlangung des akademischen Grades eines

Diplom-Ingenieur

in

Technische Chemie

[gemeinsames Studium im Rahmen von NAWI Graz]

eingereicht an der

Technischen Universität Graz

Betreuer

Assoc.Prof. Dipl.-Ing. Dr.techn. Viktor Hacker

Institut für Chemische Verfahrenstechnik und Umwelttechnik

Technische Universität Graz

Graz, Mai 2014

Abstract

A prerequisite for the commercialization of high-temperature polymer electrolyte membrane fuel cells (HT-PEMFC), developed to supply single-family homes with electricity and heat, is the cost reduction of the system. As high loadings of the scarce and expensive noble metal platinum are required to catalyze the kinetically slow oxygen reduction reaction (ORR) on the cathode, combining Pt with inexpensive and abundant metals, such as Fe, is a viable route in order to lower the Pt loading and raise the catalyst's activity toward the ORR.

In this work PtFe nanoparticles on a high surface area carbon support were synthesized by an inexpensive and straightforward preparation method. Pre-prepared gas diffusion electrodes were impregnated with a precursor solution containing Pt and Fe salts. After the reduction to the respective PtFe nanoparticles, the catalyst sheets were post-treated with acid leaching and mild heat-treatment. The optimization of the synthesis parameters and the post-preparation treatment were the main objective of this work in order to manufacture PtFe/C catalysts with good catalytic properties and high stability.

Ex-situ characterization and accelerated stress tests were carried out by means of cyclic voltammetry using the thin-film rotating disk electrode method. In-situ single cell testing in HT-PEMFC operating conditions was performed as well.

Kurzfassung

Die erfolgreiche Markteinführung der für die Energie- und Wärmeversorgung von Einfamilienhäusern entwickelten Hochtemperatur Polymerelektrolytmembran Brennstoffzelle (HT-PEMFC) setzt eine Kostenreduktion des Gesamtsystems voraus. Als Katalysator für die kinetisch stark gehemmte Sauerstoffreduktionsreaktion (ORR) auf der Kathodenseite der Brennstoffzelle wird üblicherweise das teure und seltene Edelmetall Platin in einer relativ hohen Beladung von über $1\,\mathrm{mg\,cm^{-2}}$ eingesetzt. Ein Weg, um sowohl die Platinbeladung zu senken als auch die katalytische Aktivität in Bezug auf die ORR zu erhöhen, besteht darin, Platin mit einem zweiten günstigeren und reichlich vorhandenen Metall wie Eisen zu kombinieren.

Im Zuge dieser Arbeit wurden auf Kohlenstoff geträgerte PtFe-Nanopartikel mittels einer günstigen und unkomplizierten Synthesemethode hergestellt. Dafür wurden zuvor hergestellte Gasdiffusionelektroden mit einer Imprägnierlösung behandelt, die sowohl ein Platin- als auch ein Eisensalz enthielt. Nach der Reduktion der Salze zu den entsprechenden PtFe-Nanopartikeln wurde die fertige Katalysatorschicht mittels Säurebad und milden Temperaturprogrammen nachbehandelt. Die Entwicklung der Syntheseschritte und die Optimierung der einzelnen Herstellungsparameter war das Hauptziel dieser Arbeit. Im Zuge dieser konnten PtFe/C Katalysatoren mit guten katalytischen Eigenschaften und hoher Stabilität hergestellt werden.

Ex-situ Charakterisierung und beschleunigte Stresstests wurden mittels Cyclovoltammetrie unter Verwendung der Dünnschichtmethode auf einer rotierenden Disk-Elektrode durchgeführt. Außerdem wurde der Katalysator in-situ in einer Brennstoffzelle unter HT-PEMFC Arbeitsbedingungen getestet.

Deutsche Fassung:
Beschluss der Curricula-Kommission für Bachelor-, Master- und Diplomstudien vom 10.11.2008
Genehmigung des Senates am 1.12.2008

EIDESSTATTLICHE ERKLÄRUNG

Ich erkläre an Eides statt, dass ich die vorliegende Arbeit selbstständig verfasst, andere als die angegebenen Quellen/Hilfsmittel nicht benutzt, und die den benutzten Quellen wörtlich und inhaltlich entnommenen Stellen als solche kenntlich gemacht habe.

Graz, am ……. ……..
(Unterschrift)

Englische Fassung:

STATUTORY DECLARATION

I declare that I have authored this thesis independently, that I have not used other than the declared sources / resources, and that I have explicitly marked all material which has been quoted either literally or by content from the used sources.

……. ……..
date (signature)

Danksagung

An dieser Stelle möchte ich Univ. Prof. Viktor Hacker für die Möglichkeit diese Masterarbeit zu verfassen und für seine Unterstützung während dieser Zeit danken.

Einen großen Dank möchte ich DI Alexander Schenk und DI Christoph Grimmer aussprechen, die mir mit viel Einsatz und Geduld immer weiterhelfen konnten. Durch ihre engagierte Betreuung war es mir möglich viel Neues in dieser Zeit zu lernen. Selbstverständlich gilt der gesamten Brennstoffzellen-Arbeitsgruppe für das freundschaftliche und lockere Arbeitsklima mein Dank. Die Summer School mit euch in Japan war eine unglaublich tolle und bereichendere Erfahrung und ich bin sehr froh, dass ich daran teilnehmen konnte.

Meinen Eltern und meiner Großmutter danke ich für ihre andauernde moralische wie finanzielle Unterstützung während meiner Studienzeit. Ihr habt mir ideale Studienbedingungen ermöglicht, so dass ich mich immer voll auf mein Studium konzentrieren und die letzten Jahre wirklich genießen konnte.

Nicht zuletzt gilt mein Dank Christoph Staudinger, mit dem ich die Höhen und Tiefen dieses langen Studiums durchgestanden habe. Es ist fast unmöglich aufzuzählen, was wir alles an schönen Dingen in dieser Zeit zusammen erlebt und gesehen haben. Dafür und für deine immer vorhandene Unterstützung möchte ich dir danken.

Birgit Pichler Graz, Mai 2014

Contents

1 Introduction

In the face of an increasing world-wide energy demand and depleting fossil fuel resources, alternative methods of energy production are needed in order to stop environmental pollution by continued emission of green-house gases and to assure further economical growth and socio-ecological prosperity. A projected increase in the world's energy consumption of 56% between 2010 and 2040 (thereof about 90% in non-OECD countries such as China and India), has to be met with an increase of low-carbon energy sources (renewables and nuclear) [1]. Moreover, the change to renewables as primary energy sources is crucial to limit the man-made global warming to the 2 °C goal. Evidence of the human influence on the global warming is given by the correlation of the average surface temperature increase in the last decades with the increased CO_2 concentrations in the atmosphere, which exceed the pre-industrial level by 40%. This is primarily caused by the global fossil fuel consumption [2].

In the need of an environmental friendly energy conversion technology, fuel cells offer a promising alternative to combustion engines due to their efficient electrochemical energy conversion. Even when fuelled with oil or gas, the higher efficiency lowers CO_2 emissions significantly compared to conventional electricity generation via combustion [3].

Fuel cells can be used in a wide range of applications from portable devices to transportation and stationary units. A promising market are the small/medium-scale decentralised electricity generation units with combined heat and power production [3]. The main field of research are the polymer electrolyte membrane fuel cells (PEMFCs) and the so called high-temperature (HT-)PEMFCs working at temperatures above 100 °C. Despite the extensive research in the past decades on the development of the fuel cell key components, such as the electrodes and the membrane in the membrane electrode assembly (MEA), reaching of the cost targets and higher durability are still the main objectives against fuel cell commercialization [4]. Lowering the costs is only achievable by understanding and improving the electrocatalysis in the fuel cell, especially of the kinetically slow oxygen reduction reaction (ORR) on the cathode. Considering the high and broadly fluctuating world market prizes for Pt (March 2014 ~ 37 €/g [5]), about 30% to 50% of the stack cost are due to the use of the scarce precious metal Pt as the catalyst for both anode and cathode. Pt is thereby hard to replace, as it exhibits the highest catalytic

activity of all pure metals toward the ORR [6]. Therefore the synthesis of shape defined Pt based nanoparticle catalysts with a narrow size distribution is a promising way to improve catalytic performances [4]. The ideal catalyst would thereby consist of only a single layer of Pt (with the same activity as pure Pt) supported on a stable, inexpensive and abundant material [7], such as a second, non-noble metal (e.g. Fe, Co, Ni). A high dispersion and long-term stability of the catalyst particles are essential as well [7].

The second important goal in order to reach fuel cell commercialization on an industrial scale is the introduction of a simple, environmentally friendly production process [4]. Besides the challenge of manufacturing catalysts in sufficient quantities and qualities, focus in research has to lay on the improvement of PEMFC lifetime, on a cost reduction of the production process as well as on the reduced usage of Pt in the catalyst layers. To achieve this, not only the catalyst system has to be improved, but the whole production pathway. This poses new challenges on the utilized materials and the process engineering [4].

In this work a straightforward synthesis method for the preparation of PtFe/C cathode catalysts is studied by varying production parameters and by introducing post-treatment steps of the prepared catalysts such as acid leaching and mild heat-treatment. The goal is to obtain catalysts with good catalytic properties toward the ORR and with a high stability.

2 Theory

2.1 Fuel Cell Fundamentals

In contrast to combustion engines, fuel cells are characterized by their ability to convert chemical energy directly into electricity and heat. This conversion occurs through an electrochemical reaction of the externally supplied fuel (e.g. H_2) with an oxidant (e.g. air or pure O_2) via two electrodes and an ion conducting electrolyte [3].

The five most common fuel cell technologies, which are categorized according to the utilized electrolyte, are [8, p. 1]:

- Polymer electrolyte membrane fuel cell (PEMFC)
- Alkaline fuel cell (AFC)
- Phosphoric acid fuel cell (PAFC)
- Molten carbonate fuel cell (MCFC)
- Solid oxide fuel cell (SOFC)

Among these the PEMFC is especially suited for portable and smaller-scale applications because it uses a quasi-solid membrane instead of a liquid electrolyte. Very important assets of this kind of fuel cell include the compact system and the low operating temperatures below 90 °C resulting in a high power density and an easy handling [8, p. 1].

The electrochemically interesting part of a PEMFC is the so called membrane electrode assembly (MEA) consisting of the proton conducting polymer electrolyte (usually a Nafion® membrane for this type of fuel cell) and the two electrodes separated by the membrane [8, p. 5]. Each of the electrodes is built up by a catalyst layer tightly connected to the membrane and by the gas diffusion layer, which provides support for the catalyst layer and enables gas diffusion into and water transport out of the MEA.

In the anode catalyst layer H_2 (though PEMFCs fuelled with MeOH and EtOH are possible as well) is oxidized with a platinum catalyst and the resulting protons move through the gas-tight

membrane to the cathode. The electrons however are transported over the external circuit generating an electrical current. Finally, the protons and electrons react with O_2 in the cathode catalyst layer via the so called oxygen reduction reaction (ORR) and form only H_2O and heat (see Table 2.1 and Fig. 2.1) [9].

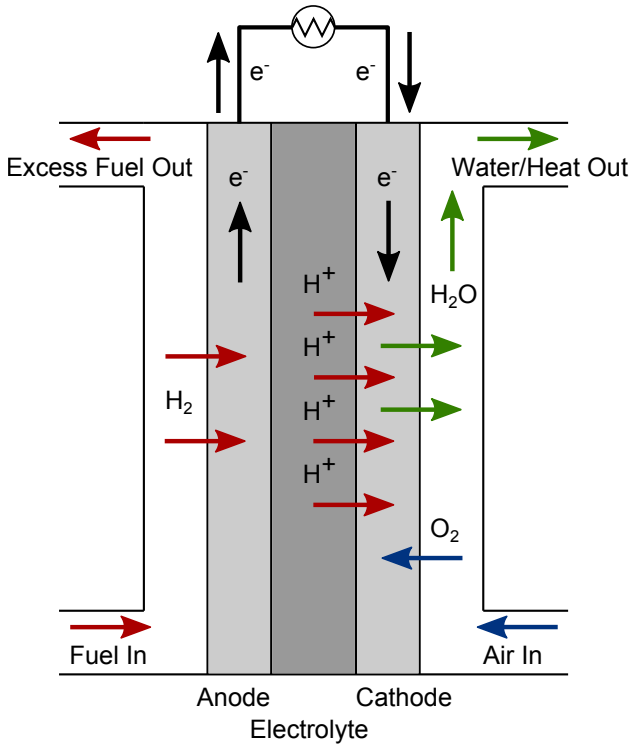

Figure 2.1: 2D schematic of a H_2/O_2 PEMFC (based on [10]).

Table 2.1: PEMFC Reactions [3]

Anode Reaction	Cathode Reaction	Overall Reaction
$H_2 \longrightarrow 2\ H^+ + 2\ e^-$	$0.5\ O_2 + 2\ H^+ + 2\ e^- \longrightarrow H_2O$	$H_2 + 0.5\ O_2 \longrightarrow H_2O$

The optimization of the anode and cathode catalyst layers is challenging, as they should provide electrical conductivity, fuel and oxidant diffusion and water removal [9]. The key is the formation of a so called three-phase boundary on the catalysts surface [4]. The electrochemical reaction can only take place, if the catalyst is connected electronically to the external circuit and to the proton conducting network. At the same time the catalyst's accessibility to gas molecules has to be maintained [11]. So far, highly dispersed platinum nanoparticles on an electron conducting carbon support, e.g. carbon blacks, carbon nanotubes or carbon nanofibers, are the most widely applied catalysts for both electrode reactions [9].

2.1.1 Electrochemical Characteristics

The theoretical thermodynamical cell voltage or the so called open circuit voltage of a H_2/O_2 fuel cell can be described by a combination of the two Nernst equations for the anode and cathode side leading to equation 2.1 [9, 12].

$$V_{theory}^{OCV} = E_{O_2/H_2O}^0 - E_{H_2/H^+}^0 + \frac{2.303RT}{2F} \cdot log\left(\frac{p_{H_2} \cdot p_{O_2}^{0.5}}{p_{H_2O}}\right) \tag{2.1}$$

with the two standard electrode potentials at 1.0 atm and 25 °C:

$$E_{H_2/H^+}^0 = 0\,V \tag{2.2}$$

$$E_{O_2/H_2O}^0 = 1.229\,V \tag{2.3}$$

Further included in this equation are the universal gas constant R ($8.314\,J\,K^{-1}\,mol^{-1}$), the Faraday constant F ($96\,487\,C\,mol^{-1}$), the temperature T and the respective partial pressures of the reagents and the product.

The performance of a fuel cell is characterized by several significant voltage losses, which lower the power output dramatically. The four main factors contributing to the reduction of cell potential are described in Eq. 2.7 [13].

$$E_{cell} = E_{rev(p_{H_2},p_{O_2},T)} - \Delta E_{ohmic} - \eta_{ORR} - \eta_{tx} \tag{2.4}$$

The reversible cell voltage E_{rev} describes the reduced theoretical OCV by considering the real partial pressures of the reactant and the operating temperature. The other three factors are the ohmic losses E_{ohmic} resulting from contact resistances between flow-fields and the diffusion media and from proton conduction, the mass-transport losses η_{tx} caused by slow O_2 transport (the anode side is negligible in this case) and the very significant overpotential losses η_{ORR} caused by the slow reaction kinetics of the oxygen reduction reaction (anodic side again of less importance). The contributions of each of these potential losses can be seen in Fig. 2.2, where the ORR overpotential loss of about 400 mV at $1.5\,A\,cm^{-2}$ stands out.

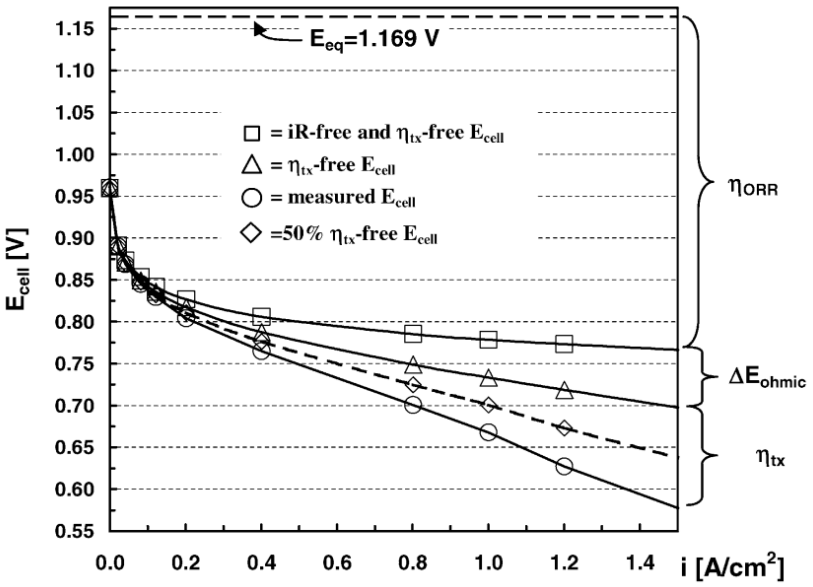

Figure 2.2: U/I curve for a 50 cm^2 single cell H_2/air fuel cell (80 °C, 150 kPa total pressure) corrected by the different voltage losses from Eq. 2.4 [13].

2.2 High-Temperature PEM Fuel Cells

Closely related to the PEMFC working below 90 °C is the so called high-temperature PEMFC (HT-PEMFC), which is usually operated at temperatures around 160 °C. It exhibits several advantages over the common PEMFC due to the significant influence of the higher working temperature on the cell performance. On the downside the theoretical OCV is lowered, however at the same time elevated temperatures enhance proton conductivity, mass transfer and the kinetics for both electrode reactions via increased anodic and cathodic exchange current densities [12].

As can be seen in Eq. 2.5 the reversible cell potential E_{rev} at constant pressure is dependant on the change of entropy ΔS, which is negative in the case of the H_2/O_2 reaction. Below 100 °C the reactant gases are formed into liquid water therefore E_{rev} decreases strongly with increasing temperature (slope of $\delta E_{rev}/\delta T = -0.85\,\mathrm{mV\,K^{-1}}$). Above 100 °C this effect is less pronounced as the water stays in its gaseous phase (slope $\delta E_{rev}/\delta T = -0.23\,\mathrm{mV\,K^{-1}}$).

$$\left(\frac{\delta E_{rev}}{\delta T}\right)_p = \left(\frac{\Delta S}{nF}\right)_p \tag{2.5}$$

Furthermore, the liquid water management is simplified, as the product water is removed in its gaseous phase resulting in less mass transport limitations and a simplified flow-field design.

Also the cooling system works more efficiently due to the higher temperature gradient between the fuel cell and the coolant. This allows a more compact heat-exchanger build-up, thereby raising the overall mass- and volume-specific power density of the system [14].

Another advantage of the HT-PEMFC is the higher contamination tolerance. Especially CO, which is always a trace amount impurity in steam-reformed H_2, can poison the Pt catalyst by its strong adsorption onto the surface and can lead to a significant performance loss even at CO concentration of only 10-20 ppm. To avoid this, reformate H_2 from organic fuels has to be further purified increasing both cost and complexity of the overall process [15]. As $Pt-CO$ formation shows a high negative entropy, raising the fuel cell's operating temperature causes a lower CO coverage on the surface and a higher contaminant tolerance (e.g. 1000 ppm at 130 °C [14])

However, higher temperatures can lead to increased H_2 cross-over rates through the membrane and have a deep impact on the stability of each of the utilized components and materials [12] (see section 2.2.1).

Therefore, the built up of a HT-PEMFC has to be adapted to the higher temperatures, which excludes the usage of the highly humidified Nafion® membranes. Instead, a phosphoric acid doped polybenzimidazole (PA-PBI) membrane is used. This type belongs to the acid-base polymer membranes and is characterised by an amorphous thermoplastic polymer with high thermal stability (T_g of about 430 °C) protonated with an excess of phosphoric acid to provide proton conductivity. Phosphoric acid works thereby as a "hopping" partner for the protonated nitrogen atom on the imidazole ring (see Fig. 2.3). This system allows operating temperatures as high as 200 °C without external humidification [15].

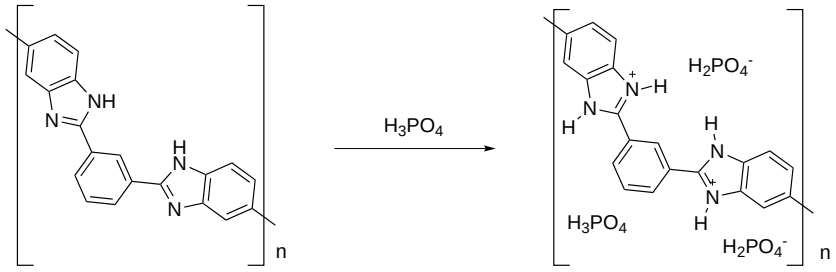

Figure 2.3: Doping of polybenzimidazole with phosphoric acid [15].

2.2.1 Stability of HT-PEMFCs

Long-term stability is one of the main issues and a major challenge concerning HT-PEMFC operation because of its very acidic (pH = 0) and oxidising operating conditions [7]. Especially

the stability of the catalyst and the membrane has to be assured to guarantee a lifetime of 5000 h and more without significant performance loss (degradation rates of only few $\mu V\,h^{-1}$ required) [13]. The main degradation problems for conventional Pt/C catalysts are [11]:

- Ostwald ripening based particle coarsening at voltages $> 0.8\,V$ (high Pt solubility)
- Pt crystal migration and coalescence at low voltages $< 0.7\,V$ (less pronounced effect)
- Detachment and carbon corrosion induced agglomeration of Pt particles at voltages $> 1.1\,V$
- Dissolution and reprecipitation of Pt particles in the membrane via a chemical reduction of Pt^{2+} with cross-over H_2

These effects depend on the applied voltage and are more pronounced when the voltage is cycled. Under normal acidic PEMFC operating conditions (about 0.7 V) the solubility of Pt is rather small depending on the shape of the catalyst, but increases dramatically up to 1.1 V [16]. The dissolution is even more prominent for nanoparticles $< 4\,nm$, because of the high number of surface atoms with a weaker cohesive binding. Also under-coordinated Pt atoms exhibit higher solubility compared to bulk Pt [7].

At higher potentials the formation of an oxide layer (Pt−O) effectively protects further dissolution [6], although high potential cycling can promote corrugation of Pt (e.g. formation of edges and steps) [7]. The effect of particle size growth and broader particle size distribution can be seen in Fig. 2.4, where images of a Pt/C catalyst before and after a 600 h lifetime test are shown [17].

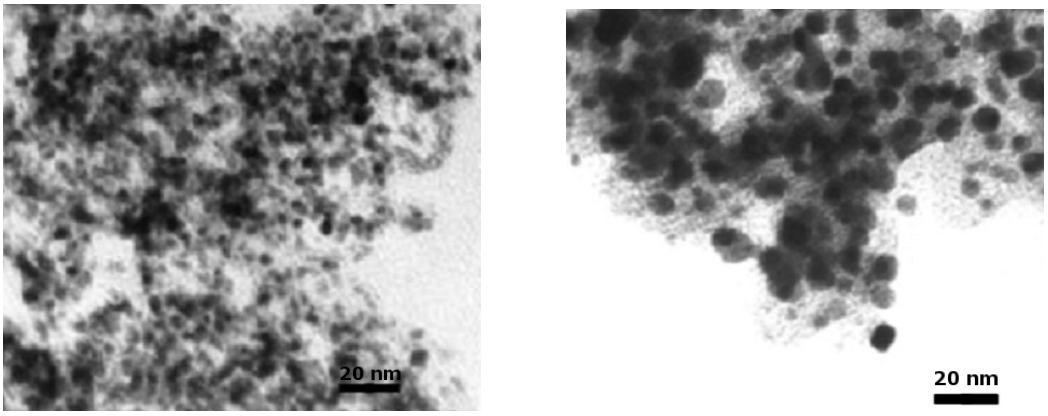

(a) Fresh TKK 46.2% Pt/C catalyst finely dispersed.

(b) Pt/C catalyst at cathode after 600 h lifetime test exhibiting big agglomerations.

Figure 2.4: TEM images of a Pt/C catalyst before and after a 600 h lifetime test at 150 °C (current denstiy $714\,mA\,cm^{-2}$) [17].

Besides the loss of active Pt surface area the so called carbon corrosion is the second important process, which lowers the operating lifetime of a PEMFC. It describes the effect of carbon oxidation to CO_2 at voltages higher than 1.1 V resulting in loss of electrical contact [4, 7]. Although under normal operating voltages this effect is less pronounced due to its kinetic hindrance, it can occur at high start/stop potentials. Nevertheless carbon is still the best choice as support material, as it has high electronic conductivity ($> 1\,\mathrm{S\,cm^{-1}}$) and a high specific surface area (50 to $800\,\mathrm{m^2\,g^{-1}}_{carbon}$) with a highly porous structure (pore sizes of 20-100 nm) [4]. By way of comparison graphitized carbon exhibits a higher corrosion resistance than amorphous carbon. However, good Pt dispersion is thereby harder to achieve as graphitized carbon has a smaller surface area [4, 15].

The operating environment of an HT-PEMFC is quite comparable to a PAFC, namely the high temperatures and the phosphoric acid environment. Besides enhanced Pt agglomeration due to dissolution and redepositioning, leaching of H_3PO_4 and increased H_2-crossover caused by membrane degradation play also an important role in HT-PEMFC lifetime reduction [17]. Liu et al. [17] showed that a beforehand swelled H_3PO_4 doped PBI membrane was even thinner than an undoped membrane after a long-time test. They concluded that an attack of $HO^{\bullet}$ and $HO_2^{\bullet}$ radicals formed by an incomplete oxygen reduction reaction on the cathode caused the oxidative degradation of the PBI matrix, resulting in an increased loss of H_3PO_4 and reduced proton conductivity.

2.3 Catalysis of the Oxygen Reduction Reaction

The oxygen reduction reaction (ORR) on the cathode is one of the most extensively studied electrocatalytic reactions and its optimization is one of the biggest challenges toward big-scale PEMFC commercialization. The reason for this are the sluggish kinetics of this reaction resulting in overpotential losses of 0.3-0.4 V. This amounts to roughly two thirds of the whole overpotential [7] and reduces the thermal efficiency from 83% at 1.23 V (relative to the theoretical enthalpic cell potential) to 43% at 0.7 V [18] (see Fig. 2.2 on page 6).

For this whole multi-electron reaction process, which involves several different reaction intermediates, pure Pt exhibits the highest activity of all metals and is therefore the most widely applied catalyst [4]. Furthermore, only metallic bulk Pt shows - besides Au, Ir and Pd - thermodynamical stability up to 0.9 V [19, 20]. However, the activity of Pt toward the ORR is rather poor (exchange current density $= 10^{-9} - 10^{-8}\,\mathrm{A\,cm^{-2}}$) compared to its activity toward the hydrogen oxidation reaction on the anode (exchange current density $= 10^{-4} - 10^{-3}\,\mathrm{A\,cm^{-2}}$).

Therefore, the cathode needs a much higher catalyst loading and states the limiting factor for the overall reduction of Pt utilization [13, 15].

Although the reaction itself seems to be rather simple, the reaction mechanism is in fact quite complex and important aspects such as the rate determining step or reaction intermediates are still under debate. Density functional theory (DFT) is one method to simulate the ORR on a Pt(111) surface, but due to the complex environment in a fuel cell (e.g. adsorbed solvent molecules, effect of electric field in double layer) modelling gets very complicated [7, 21]. Nevertheless DFT calculations offer the possibility to predict catalytic trends regarding the ORR activity [19].

The ORR can take place via a dissociative or an associative mechanism depending on when the O−O bond is split (see Table 2.2). The first mechanism (dissociative) describes the O−O bond splitting right after O_2 adsorption, followed by two proton/electron transfer steps for each of the two oxygen atoms (overall four e^--transfer). In the second mechanism (associative) the dissociation occurs not until the adsorbed O_2 is hydrogenated for the first time. After splitting to O* and OH*, those two species are further hydrogenated to H_2O. In the third mechanism (associative) the splitting of the O−O bond occurs even another step later than in mechanism 2, forming adsorbed hydrogen peroxide as an intermediate before two H_2O molecules are produced via a third and fourth proton/electron transfer [21].

Table 2.2: The dissociative and the two different associative mechanisms of the oxygen reduction on a Pt surface [21].

Dissociative	**Associative**	
Mechanism 1	Mechanism 2	Mechanism 3
$O_2 + * \longrightarrow O_2{}^*$	$O_2 + * \longrightarrow O_2{}^*$	$O_2 + * \longrightarrow O_2{}^*$
$O_2{}^* + * \longrightarrow 2\ O^*$	$O_2{}^* + H^+ + e^- \longrightarrow OOH^*$	$O_2{}^* + H^+ + e^- \longrightarrow OOH^*$
$O^* + H^+ + e^- \longrightarrow OH^*$	$OOH^* + * \longrightarrow O^* + OH^*$	$OOH^* + H^+ + e^- \longrightarrow HOOH^*$
$OH^* + H^+ + e^- \longrightarrow H_2O + *$	$O^* + H^+ + e^- \longrightarrow OH^*$	$HOOH^* + * \longrightarrow 2\,OH^*$
	$OH^* + H^+ + e^- \longrightarrow H_2O + *$	$OH^* + H^+ + e^- \longrightarrow H_2O + *$

A graphical illustration of the different DFT-simulated energy changes occurring in the three reaction mechanisms can be seen in Fig. 2.5. In Fig. 2.5(a) at 1.23 V (theoretical OCV) the hydrogenation steps exhibit very positive energy changes and state the most difficult steps for all three mechanisms. In contrast to this, in the diagram in Fig. 2.5(b) at 0.8 V (operating potential) these limiting steps have become much easier requiring less energy, which explains the high overpotentials needed for the ORR [21]. In all cases the O_2 dissociation releases a

significant amount of energy with only an activation barrier of about 0.25 eV. This leads to the conclusion that the hydrogenation steps are limiting and that therefore all of the three mechanisms for the ORR are plausible. Thus a parallel mechanism, where both, dissociative and associative route, are combined depending on the metal and the potential applied, seems to be a good explanation for the ORR pathway [21, 22].

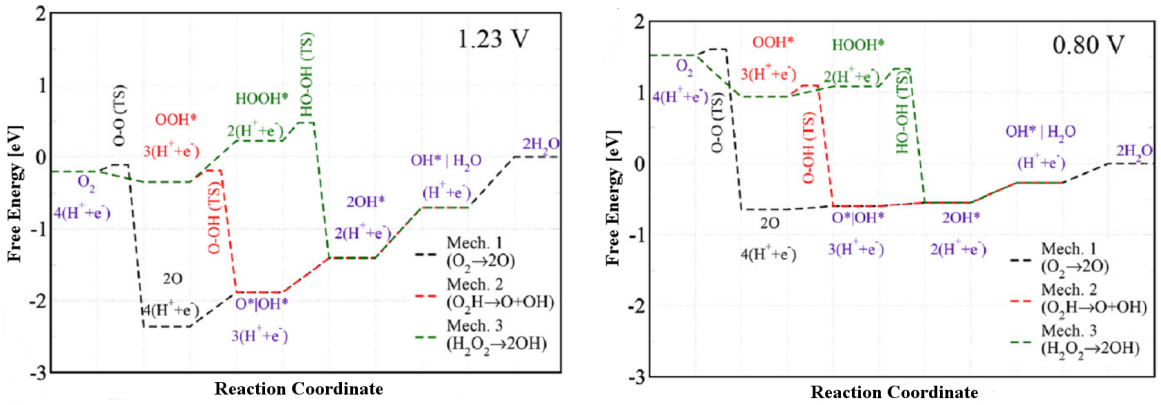

(a) The three mechanisms at 1.23 V: The proton and electron transfer is in all cases energetically steep uphill.

(b) The three mechanisms at only 0.8 V: in this case the proton/electron transfer is energetically much more favored.

Figure 2.5: DFT-calculated free energy diagrams of the ORR on a Pt(111) surface at equilibrium potential (1.23 V) and at operating potential (0.8 V) for all three mechanisms [21].

For Pt nanoparticles it is assumed that the active sites of the catalyst are found upon the terraces, whereof the (111) facets exhibit the highest activities. In contrast, under-coordinated sites such as edges show too strong adsorption toward the reaction intermediates [19]. Stephens et al. [7] conclude in their DFT studies that either the first proton/electron transfer to form HOO* (see Table 2.2 second equation of mechanism 2 and 3) or the last reaction, where free H_2O is generated via reduction of HO* (last reaction of all three mechanisms in Table 2.2), is the rate determining step in the ORR. Both steps (here depicted as ΔG_1 and ΔG_4, respectively) exhibit a positive uphill energy step at 1.23 V and only become downhill at 0.81 V, again explaining the significant voltage loss. Hence, an ideal catalyst should show a completely flat or negative energy diagram at the theoretical maximum cell voltage of 1.23 V with the whole four-electron reaction pathway going downhill. To achieve this, the catalyst has to be modified in a way to gain a stronger HOO* adsorption and a weaker O* and HO* bonding to promote H_2O desorption [7, 20]. However all three intermediates bind onto the surface via the oxygen atom making the adsorption energies nearly linearly dependant on each other. Both goals can not be achieved at the same time, resulting in a volcano shaped dependency of the catalytic activity of Pt on the binding energy of HO*. Depending on this binding energy the activity

is either determined by ΔG_1 or by ΔG_4, i.e. rate limited either by the transfer of H^+ and e^- or by the removal of surface oxides [7, 23]. For example, pure Pt adsorbs HO^* about 0.1 eV too strongly to achieve the maximum activity of the volcano curve [7]. This behavior is in accordance with the so called Sabatier principle which states that the most active catalyst for a reaction should bind the reaction intermediates neither too weakly nor too strongly [19, 23].

2.3.1 ORR on Nanoparticles

The most distinguishing characteristic of a nanoparticle with a size of 1-100 nm is its high surface to volume ratio (a nano-single crystal consists of only about 100-10000 atoms). As heterogeneous catalytic reactions are very sensitive to nano-scale and atomic-level structures, nanoparticles can exhibit very different catalytic properties compared to macroscopic crystals, especially when dispersed on a carbon support. Thermodynamically a nanoparticle always orders itself as to reach the lowest surface energies. This is achieved by forming low index planes, for example (111) and (100) surfaces for fcc metals such as Pt [24].

Pt catalysts go through a maximum in their catalytic activity with decreasing particle size. The extent of this so called particle size effect is still under debate because its evaluation provides experimental challenges and because the maximum of activity is dependant on the catalyst's shape and composition (Pt alloys see sec. 2.4) [4]. Theoretical models predict the peak to be found around 3 nm [7] to 4.5 nm [4, 25]. The importance of this effect was investigated by Gasteiger et al. [13], who determined for Pt in H_3PO_4 an activity decrease by a factor of about three when the particle sized was reduced from 12 to 2.5 nm.

An increase in Pt nanoparticle dispersion on carbon, which is done to obtain more active sites, goes hand in hand with a decrease in mean particle size. But due to this particle size effect there is a limit for activity enhancement at about $80\,m^2\,g^{-1}{}_{Pt}$. As the particle size decreases the number of under-coordinated sites such as steps, edges and kinks is raised in relation to the Pt(111) and Pt(100) facets. One explanation for the particle size effect states, that those sites provide even stronger binding sites for ORR intermediates (pronounced oxophilic behavior) and thus contribute to an even greater overpotential barrier for the ORR [7, 25].

2.3.2 Kinetics of the ORR

The so called Butler-Volmer equation describing the current-potential relationship, can be simplified for cases of high overpotentials of $> 60\,\text{mV}$ as it is the case for the ORR. This leads to the Tafel equation and is expressed in Eq. 2.6 for the cathode side. It shows that in a certain current density range the overpotential is linearly dependant on the logarithmic current density $log(i_{cathode})$ [8, pp. 58-60].

$$\eta_{cathode} = a - b \cdot log(i_{cathode}) = \frac{2.303 \cdot R \cdot T}{\alpha_O \cdot n_{a,O} \cdot F} \cdot log(i_{0,O_2}) - \frac{2.303 \cdot R \cdot T}{\alpha_O \cdot n_{a,O} \cdot F} \cdot log(i_{cathode}) \quad (2.6)$$

with

$$\eta_{cathode} = E_{cathode} - E^0 \quad (2.7)$$

In this equation $\eta_{cathode}$ describes the overpotential on the cathode, $i_{cathode}$ the current density on the cathode and i_{0,O_2} the cathodic exchange current density, which is the current density at $\eta_{cathode} = 0$. Further in this equation are the so called symmetry factor α_O (a value between 0 and 1 but usually assumed to be 0.5), the electron transfer coefficient for the ORR $n_{a,O}$, the Faraday constant F, the universal gas constant R and the temperature T.

The overpotential is defined as the difference between the cathode potential $E_{cathode}$ and the equilibrium potenial E^0 (Eq. 2.7). When the overpotential $\eta_{cathode}$ from Eq. 2.6 is plotted against $log(i_{cathode})$ (Tafel plot) the electron transfer coefficient can be obtained from the slope of the curve b. This gradient is called Tafel slope and the higher it is the slower are the reaction kinetics. Furthermore, the exchange current density i_{0,O_2} on the cathode can be evaluated in this plot from the intercept of the current density i at $\eta_{cathode} = 0$ (term a)[8, pp. 58-60] [9].

In the Tafel plot for the ORR on Pt the Tafel slope exhibits two different regions, changing its value at about 0.8 V (if plotted against $E_{cathode}$ instead of the $\eta_{cathode}$). This indicates that the kinetics of the ORR vary in the two different potential ranges depending on the coverage of adsorbed oxygen [26].

At potentials $< 0.8\,\text{V}$ (high current density region) the Tafel slope has a value of $60\,\text{mV}\,\text{dec}^{-1}$ as the reaction surface consists of pure Pt. This corresponds to a direct four e^- pathway and the kinetics follow a Langmuir isotherm (indicating that the heat of adsorption is independent on coverage) [8, p. 113][26].

At potentials $> 0.8\,\text{V}$ (low current density region) the Tafel slope shows a value of $120\,\text{mV}\,\text{dec}^{-1}$ because the surface consists of a mixture of Pt and PtO (pseudo two e^- process). This correlates to a Temkin isotherm, where the heat of adsorption is dependant on the surface coverage [8, p. 113][26].

Therefore the ORR usually exhibits a mixed 2- and 4-electron pathway depending on whether H_2O_2 is produced as a reaction intermediate [9]. The occurrence of H_2O_2 as reaction intermediate however is not desired, as it not only reduces the energy conversion efficiency but mainly because it can create damaging free radicals species in the catalyst layer through its high reactivity [8, p. 32].

2.4 Pt Alloy Catalysts

Basically there are two ways to raise the mass activity of a Pt catalyst: either by obtaining a higher number of active sites by increasing the dispersion while reducing the particle size to 3 nm and the surface up to a maximum of $80\,m^2\,g^{-1}{}_{Pt}$ (see particle size effect sec. 2.3.1), or by improving the intrinsic activity of the catalyst. The latter can be achieved by alloying Pt with less noble late 3d transition metals such as Fe, Co and Ni [7]. They show the highest improvements in regard to the catalytic activity [27], but also Pt−Mn, Pt−Cu, Pt−Cr, Pt−V and other alloys are of interest [26].

Pt alloy catalysts were first developed for PAFCs in the 70s and 80s [4] and exhibit an about 3 to 4-fold specific activity and an approximately 2-fold mass activity improvement [16]. Besides the advantage of enhanced catalytical activity, alloying Pt with a more abundant and more inexpensive metal could contribute to a significant cost reduction of the whole electrocatalytic system [26]. For this purpose the electrode structures should be optimized to avoid losses other than the kinetically predicted overpotential. Furthermore, the catalyst should exhibit its best performance at voltages $\geqslant 0.65\,V$ to reach a high energy conversion efficiency [13].

However, difficulties arise in determining the effects of alloying on Pt catalysts, especially on a carbon support, as there are several different parameters affecting its activity. Depending on the catalyst's microstructure such as particle size, shape and composition and/or its synthesis method including post-treatment steps, the Pt nanoparticle's activity can differ significantly compared to plain Pt bulk surfaces [23]. Also the electrolyte components, especially the solvent and the respective ions, have an influence on the activity and further complicate the interactions between catalyst's surface, reactants, intermediates and electrolyte [24].

Compared to pure Pt, Pt alloys exhibit slightly weaker adsorption toward O^*, HO^* and HOO^*, and are therefore closer to the optimal adsorption strength in the activity volcano plot, though slightly off on the other side of the peak than pure Pt [7]. DFT simulations showed this change in binding energies for a Pt monolayer on Fe, Ni and Co, whereof all three catalyst variations showed slightly different binding energies. The ΔE_{OH} and ΔE_O binding energies for Pt on Fe gave values of 0.85 eV and 2.06 eV respectively compared to 1.05 eV and 1.57 eV for a pure Pt surface [22].

2.4.1 Catalytic Enhancement Effects of Pt Alloys

The catalytic enhancement of Pt alloys compared to pure Pt is caused by several effects all influencing each other. Although the extent of each parameter is still under discussion in literature they can be categorized as listed below and the first three effects are described in more detail [13, 28]:

- Leaching out of 3d metals i.e. surface sensitive factors
- Electronic factors
- Structural and geometrical factors
- Particle size effect (because of particle size growth due to coalescence (see sec. 2.3.1))
- Other factors such as change in wettability of the catalyst system and redox processes involving the 3d metals

Surface Sensitive Factors – Leaching

Pt alloy catalysts undergo severe structural modifications under the acidic HT-PEM fuel cell operating conditions, as the non-noble metal (Fe, Co or Ni) show low stability at higher voltages and in an acidic environment. The most prominent effect is the leaching of the non-noble metals resulting in an increase of the catalyst's surface and thus its activity through a roughening effect (see Fig. 2.7). Not even alloying the two metals at high temperatures can completely prevent the leaching at high voltages, as the PEMFC cathode is operated at potentials above the dissolution potential of the non-noble metal [7, 13]. At 3d metal contents $< 60\,\text{atom}\%$ the dissolution is more or less restricted to the upper layers, whereas at higher contents the bulk is also affected [16].

When leaching occurs in-situ the solute metal cations can poison the membrane and lead to degradation (see Fig. 2.7). Furthermore, during voltage cycling the dissolution of the 3d metal and the formation of a thick outer Pt "shell" can suppress the enhancing effect of the alloying metal [16]. Therefore pre-leaching steps of the catalyst can be introduced to selectively modify the surface, consequently avoiding unwanted processes which can lower the fuel cells performance [7].

Electronic Factors

The so called d-band center – the average energy level of the metal d states – can describe the strength of the metal-adsorbate interaction and is one of the key parameters determining the

ORR kinetics. It states a general measure of surface reactivity [19, 23], as it correlates with the ΔG of O_2 adsorption and with the fractional coverage of OH^* present on the surface [23].

Generally in heterogeneous catalysis, the adsorption energy of a reactant on a metal catalyst's surface is determined by the catalytic structure and varies with the type of metal. Especially the coupling of the valence orbitals of the adsorbate, in case of the ORR the O_2 2p states, with the d-states of the catalyst metal (Pt 5d) contributes to the differences in adsorption energy. Of importance is the energy level of the metal d-states relative to the Fermi energy (the highest occupied state). The higher the d-band center lies, the higher is the energy of the antibonding states (thus they are becoming less occupied), and the bond between catalyst and adsorbate is strengthened. The lower the energy level the weaker the bond interaction, as the antibonding states become more filled [27, 29]. In case of pure Pt as ORR catalyst the d-band center is too close to the Fermi level and thus the adsorption of oxygen species is too strong. This explains why the high surface coverage by HO^*/anions in proportion to the number of free active sites is limiting for Pt [23].

The electronic structure of an active catalyst can be modified by its neighboring atoms when alloyed with a second metal. This so called ligand effect appears to be more pronounced when the non-noble metal atoms are found in the adjacent second layer and gets rather negligible when the alloying metal atoms are farther away than the fourth layer [19]. An illustration of this effect can be seen in Fig. 2.6. The down-shift of the d-band center as well as the differences between the three low-index surfaces, (111), (100) and (110) respectively, are pronounced when comparing the specific activity of a pure Pt surface to a well-characterized Pt_3Ni-skin single-crystal electrode surface prepared and analyzed under ultrahigh vacuum conditions. Especially the $Pt_3Ni(111)$ surface exhibits extraordinary activity under these conditions giving proof of the positive effect of alloying. However, the challenge still remains to transfer these promising properties to a nanoparticle catalyst for applications under real fuel cell conditions [18].

Structural and Geometrical Factors

Pt exhibits a fcc (face centered cubic) lattice of 3.93 Å. Substituting or underlying Pt with a second metal with a smaller atomic dimension can lead to a lattice contraction in the Pt atomic structure. This results in the so called strain effect, which describes the reduction of Pt−Pt interatomic distance by a compressive strain parallel to the catalyst's surface. This compressive strain weakens the Pt interaction with the ORR intermediates by providing more favorable sites for the dissociative adsorption of O_2 [13, 19]. On the opposite, a tensile strain on the geometric surface would strengthen the adsorption of oxygen species [19]. The strain effect

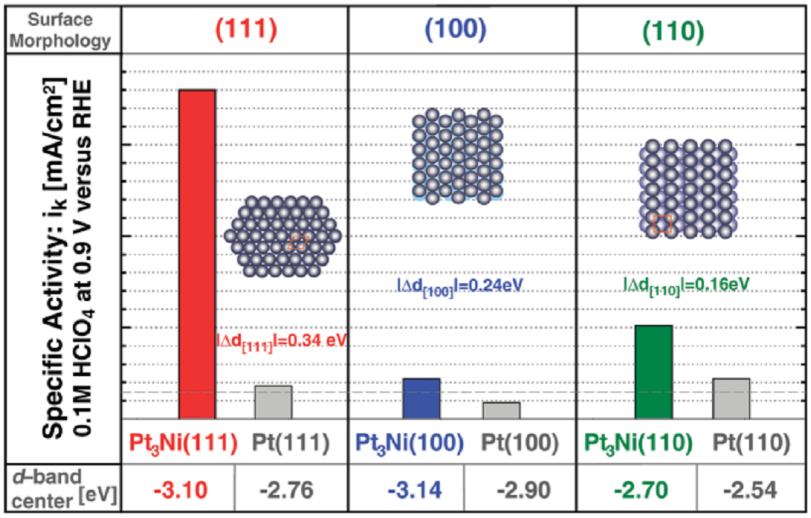

Figure 2.6: Influence of alloying with Ni and of the surface morphology on the activity of a Pt catalyst in correlation to the d-band center [18].

appears more pronounced the higher the content of the second metal. When raising the 3d metal's atomic ratio, a reduction of the lattice constant and thus a decrease in Pt−Pt distance can be measured [30].

Furthermore, the type of electrolyte in contact with the catalyst's surface affects the reaction rates as well. For example, in H_2SO_4 the activity is decreased in comparison to $HClO_4$ because present HSO_4^- anions block the active sites for O_2 adsorption [31]. Moreover in the weakly adsorbing $HClO_4$ electrolyte the Pt(111) surface is more reactive than the Pt(100) whereas in H_2SO_4 Pt(111) shows the lowest activity (again because of adsorption of HSO_4^- anions) [32].

2.4.2 Morphology and Composition of Pt Alloys

Leaching of the 3d metals as described in sec. 2.4.1 results in the formation of so called Pt-skeleton surfaces (see Fig. 2.7 middle top schematic). This increases the overall Pt surface but leads at the same time to a higher number of edges and steps, which are more prone to dissolution and Pt migration. Further heat-treatment of the catalyst induces a nano-segregation of Pt onto the particle surface forming the so called Pt-skin surface. This restructuring smooths the surface and lowers the number of under-coordinated sites, which in turn enhances catalytic activity [33]. The two main differences between Pt-skin and Pt-skeleton structures are the morphology of the surface atoms (Pt-skeleton type exhibits a more corrugated surface) and the composition. Compared to the Pt-skeleton type, which keeps a bulk alloy-composition up to the surface Pt layer, the Pt-skin type shows an oscillating concentration profile [23].

In their studies Wang et al. [25] illustrate the significance of the set temperature for the heat-treatment. At high temperatures the sintering and agglomeration of particles results in a reduced Pt surface area due to particle size growth. This effect starts at about 500 °C and can result, for example, in 20 nm sized particles when heat-treated at 800 °C. Below 500 °C particle sintering is not promoted significantly, but a reduction of surface roughness can still be detected by a slight decrease in Pt surface area. However the activity of this catalyst is increased due to smoothing out of under-coordinated sites and because of surface relaxation. This process can already be initiated at temperatures below 300 °C. Furthermore, low-temperature heat-treated catalysts exhibit an enhanced stability due to atomic bulk diffusion, which leads to a Pt segregation onto the surface. This protects the 3d metal from further dissolution, promoting in turn electronic enhancement effects of the alloying metal enriched subsurface [25].

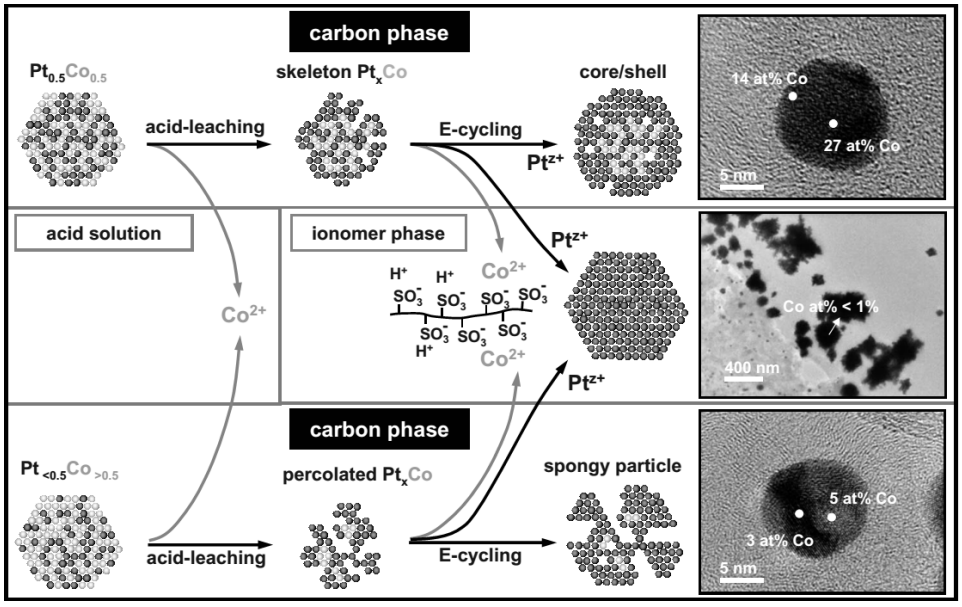

Figure 2.7: Schematic presentation of PtCo/C catalysts and its morphology changes under acidic conditions in a PEMFC depending on its composition and corresponding TEM images as illustrations [16].

As can be seen in Fig. 2.7 (upper section) a core-shell structure consisting of a Pt layer and an alloy core is formed after leaching and electrochemical dealloying via the Ostwald ripening mechanism. The middle section illustrates the dissolution of 3d metal to free cations and the formation of pure Pt particles in the PEMFC membrane (see sec. 2.2.1) [16]. For catalysts with high 3d metal content Chen et al. [16] propose the transformation of the particle into a "spongy" type after acid-leaching and potential cycling (bottom section of Fig. 2.7). This type is characterized by a very low 3d metal content and a high Pt surface area.

Another very interesting catalyst morphology modification was proposed by Dubau et al. [34], who found so called "hollow" nanoparticles. These were generated when Pt core-shell catalysts were slowly cycled in a wide potential range inducing Co diffusion to the surface, especially at high potentials. Analysis of these particles revealed a thick compact Pt shell and a hollow cavity-like core with no or nearly none 3d metal present. Interestingly they exhibited even higher ORR activities than the initial Pt-alloy despite the complete loss of 3d metal [7, 34].

2.5 PtFe/C Catalysts

Besides Co and Ni, Fe is one of the most studied 3d alloying metals. This PtFe mixture shows one of the greatest activity improvements for the ORR compared to Pt/C [26, 27]. To illustrate the effects discussed in the previous chapters some examples for PtFe catalysts from literature are described in this section.

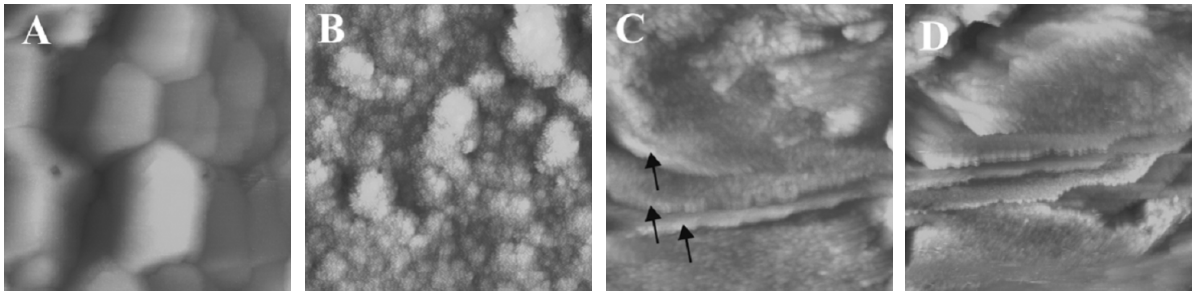

(a) Fresh PtFe film in N_2 (b) After 5 min in 0.1 M $HClO_4$ (c) after 10 potential cycles in 0.1 M $HClO_4$ (d) 40 min after potential cycling in 0.1 M $HClO_4$

Figure 2.8: Scanning tunnelling microscopy (STM) images showing the changes of a PtFe sputtered surface before and after cycling between 0.05 and 0.95 V in 0.1 M $HClO_4$, the potential was then held at 0.5 V; scan area 300x300 nm [35].

The significant surface modifications caused by acid leaching and potential cycling can be seen in Fig. 2.8. The smooth sputtered PtFe surface becomes roughened when exposed to an acidic environment. Potential cycling leads to leaching of Fe atoms resulting in a pure Pt skin layer with edges (indicated by arrows in Fig. 2.8(c)). Those edges become oriented crystalline steps after a 40 min hold at 0.5 V and form a closed packed Pt(111) surface [35]. This predicted behavior is in agreement with Toda et al. [36], who showed that the surface of a PtFe sputtered film consisted of pure Pt after cycling up to 1.1 V. Their best PtFe catalyst had a Fe content of 50% and exhibited a fcc structure like pure Pt (pure Fe is characterized by a hexagonal structure [30]). Malheiro et al. [37] described in their studies on PtFe/C catalysts the relationship between increasing Fe content and decreasing Pt−Pt atomic distance, giving

evidence for structural modifications of the Pt. Moreover, for a Pt surface on a PtFe(111) layer with high Fe content Stephens et al. [7] calculated an increased dissolution potential of about 0.16 V relative to Pt(111).

Another way to modify PtFe catalysts is by heat-treating/annealing them at several hundred degrees Celsius promoting the formation of Pt-rich surfaces, decomposing remaining organic residues on the surface and raising the degree of alloying. The downside of this method is the increase of particle size and the broadening of particle size distribution induced by the high temperatures [26, 38]. However Stamenkovic et al. [23] showed in their studies that the d-band center of a Pt_3Fe sputtered surface with a value of -2.89 eV is further down-shifted when the surface is annealed (-3.05 eV). Both values deviate strongly from a Pt bulk surface with a d-band center at -2.54 eV.

2.5.1 Synthesis Methods

In this work a simple and easily up-scalable manufacturing process was studied in order to synthesize PtFe/C catalysts for the cathode. The first step was the impregnation of a prepared carbon gas diffusion electrode with Pt and Fe precursor salts, followed by a reduction step of the respective metal ions to nanoparticles. Further catalytic enhancement was achieved by post-treatment steps, such as leaching and heat-treatment.

However, in literature there are several different methods described for PtFe/C synthesis. This leads to a broad variety of catalysts with very different properties. Important characteristics such as particle size and distribution, degree of alloying (especially after thermal treatment) and composition are determined by the synthesis method [39]. In general metal precursor salts are reduced with an appropriate reducing agent to form catalytic nanoparticles. Thereby Pt^{2+} with a reduction potential of +1.2 V is reduced more easily than the alloying non-noble 3d metals with much more negative reduction potentials (-0.2 to -0.4 V) [40].

Some of the important approaches, which are also often employed in combination, are listed below [39][8, pp. 448-463]:

- *Sputter deposition*: Simultaneous sputtering of Pt and Fe in Ar-plasma in ultra-high vacuum by using radio frequency-magnetron sputtering equipment [30, 35]. This method is often applied to synthesize unsupported extended PtFe films to study surface processes.
- *Two-step method*: In this method a commercially available Pt/C catalyst is modified by adding 3d metal precursor salt. After drying and grinding steps the catalyst is reduced at high temperatures under H_2 atmosphere [6].

- *(Reversed) Microemulsion method*: A stable oil in water or water in oil emulsion is generated with the help of a surfactant. In the micelles of this emulsion PtFe nanoparticles are selectively grown from precursor solutions with $NaBH_4$ as reducing agent [39].
- *Impregnation method*: Dispersed carbon support is impregnated with precursor salts, filtered and the resulting slurry reduced at several hundred degrees in H_2-atmosphere [41]. Because this method is easy to apply it is one of the most used techniques. Liquid reducing agents i.e. $NaBH_4$ can be used as well [8, 450f.].
- *Polyol synthesis*: The reduction of metal salt precursors is performed with diol reagents at about 200 °C. The obtained nanoparticles are then deposited on a carbon support [33]. Ethylene glycol is often utilized as it is inexpensive, non-toxic and serves at the same time as solvent for the reaction [8, p. 461].
- *Bönnemann's method*: In this method tetraoctylammoniumtriethylhydroborate serves as reducing agent and stabilizer to synthesize nanoparticles from the respective metal precursor salts. However it needs about 300 °C to remove this reagent [8, p. 462].

2.6 Characterisation via Cyclic Voltammetry

A big advancement in fuel cell catalyst research was achieved via cyclic voltammetry by the development of the thin-film rotating ring-disk electrode technique in 1998 [4]. Besides being well suited for studying reaction kinetics it can be applied for potential cycling to evaluate a catalyst's stability [4] (see sec. 2.6.3). Testing of catalysts by means of rotating disk electrode (RDE) measurements shows comparable results for ORR kinetics in regard to PEMFC testing while avoiding time consuming MEA optimization and with the advantage of being faster, easier, inexpensive and more reproducible [7, 16]. Furthermore, the RDE methodology only needs small quantities of the Pt catalyst [42], which means a significant reduction of research cost. Also the rough characterization of catalyst layer surfaces is simplified using the RDE method, as inspection of the surfaces by, for example, TEM imaging is expensive, time and labor consuming and often not representative for the whole synthesized catalyst batch [24].

2.6.1 Principles of Cyclic Voltammetry

Cyclic voltammetry is an often applied method for studying electrode processes. In principle the potential is cycled up and down in a set potential range and over a set time span, and the resulting current response recorded in a current-potential-diagram. Reproducibility of the results is thereby dependant on several parameters such as purity of the electrolyte, type of metal, choice of potential reversal points and scan rate (usually in $mV\,s^{-1}$) [43, pp. 275-276].

2.6.2 Thin-Film Rotating Disk Electrode Experiments

For RDE measurements a regular three-electrode set-up is used consisting of working, counter and reference electrode. A known amount of catalyst is deposited as a thin-film onto the glassy carbon working electrode (ring disk electrode (RDE)). Particularly the even and homogeneous drying of the thin-film is of great importance for acquiring reproducible data. The Pt loading should be between 7 and 30 µg cm^{-2} for a 10-50 wt% Pt/C catalyst as a too thick ($\leqslant 0.1\,\mu$m) film can lead to higher mass-transport resistances [44, 45]. As electrolyte 0.1 M $HClO_4$ is often used as it generates only non-adsorbing anions (ClO_4^-). This gives the utilization of $HClO_4$ a clear advantage over the usage of H_2SO_4, which generates adsorbing sulfate anions (HSO_4^- and SO_4^{2-}) lowering the electrocatalytic activity [44].

The overall quality of the measurements is significantly influenced by the cleanliness of glassware and electrodes, the thin-film quality on the RDE and the type and purity of the utilized electrolyte [44]. Furthermore, the tested catalyst's surface has to be "cleaned" by several potential cycles in order to obtain a steady current/potential diagram. Important to note is thereby that the non-noble alloying metal is mostly leached out of the surface (if no prior ex-situ leaching step was performed).

CV scans in N_2-saturated electrolyte allow the evaluation of the so called electrochemical surface area (ECSA) from the Pt−H desorption area (see upper left peak in Fig. 2.9(a) with the dashed green line as the new baseline). The first peak between 0.1 V and 0.2 V is thereby assigned to the Pt(110) surface and the broad shoulder-like peak at 0.3 V to the Pt(100) surface, respectively [46].

In O_2-saturated electrolyte and with a rotating electrode (often at 1600 rpm) the polarization curves of the ORR can be obtained 2.9(b). By quantifying the measured current at 0.9 V_{RHE} two important parameters characterizing the ORR kinetics can be calculated from that curve: the Pt normalized area-specific activity and the mass-specific activity of the catalyst (in this work denoted as specific current density (SCD) and mass activity (MA)) [16, 44]. The mass activity (normalisation based on Pt loading) presents an important factor for evaluating the economical viability of a catalyst as it gives the absolute amount of Pt needed in a fuel cell. The specific activity is normalized based on the Pt surface area (ECSA) and states therefore a measure of intrinsic catalytic activity analogous to the turnover frequency [16, 45]. The detailed description for data processing and for the evaluation of these characterization parameters including all formulas can be found in the experimental section on page 83.

The two current-potential diagrams in Fig. 2.9 illustrate a typical CV curve for Pt in a N_2-saturated electrolyte (Fig. 2.9(a)) and an ORR polarization curve with O_2 in the electrolyte

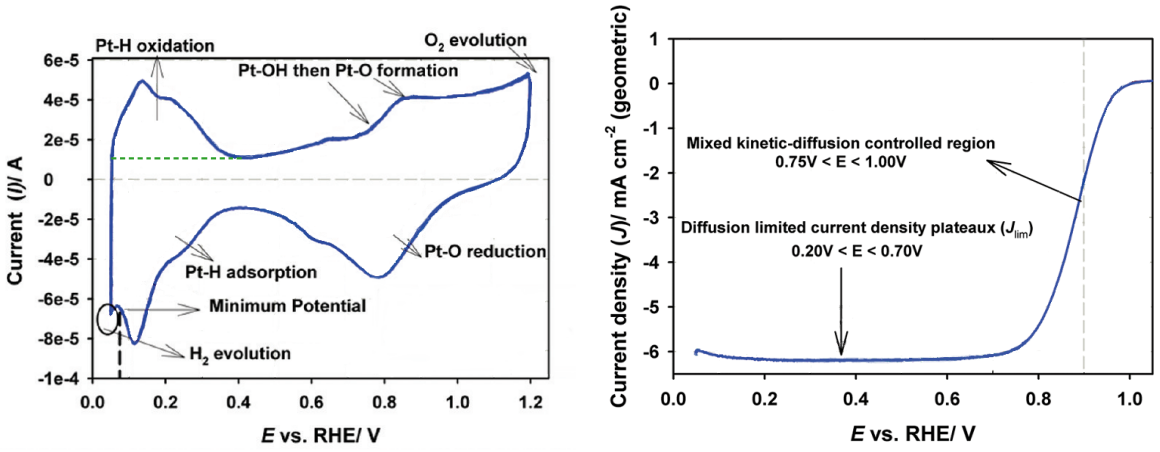

(a) CV of Pt in N_2-saturated 0.1 M $HClO_4$ depicting all important chemisorption processes.

(b) ORR curve in O_2-saturated 0.1 M $HClO_4$ with rotated disk electrode (1600 rpm), Pt loading 20 µg cm^{-2}

Figure 2.9: Characterisation of a Pt-type catalyst via cyclic voltammetry (modified from [44]).

(Fig. 2.9(b)). In N_2-saturated electrolyte only water is available for electrochemical reactions and therefore only Pt−H adsorption and desorption and the Pt−O and Pt−OH formation and reduction can be observed. The onset potential of Pt−O formation can thereby give information about the oxophilicity of the catalyst, which is an important factor for ORR activity (less oxophilic the higher the onset potential [33]). At potentials higher than 1.2 V O_2 evolution and at potentials below 0 V H_2 evolution occurs [43, 44].

In the ORR curve (Fig. 2.9(b)) the important potential range to evaluate the MA and SCD is the mixed kinetic-diffusion controlled region between 0.75 and 1.00 V_{RHE}. This region is also used to calculate the Tafel slope (see sec. 2.3.2). For Pt catalysts the potential at 0.9 V_{RHE} is often selected to calculate the two activity parameters (vertical dashed grey line) as it lies within 10 and 80% of the diffusion limited current, which in turn is dependant on the rotation speed of the RDE (1600 rpm is a often selected value) [44, 45].

2.6.3 Stability Testing

To evaluate catalyst stability the RDE method can be used to perform accelerated stress tests (AST). The AST can be designed to expose the catalyst to numerous potential cycles and/or a high constant potential. For example the Pt particle sintering phenomena can be studied with potential cycling between 0.6 V and 1.2 V, where Pt exhibits the highest dissolution rates [47]. If the potential is raised quickly in the positive sweep the Pt−O formation is too slow to effectively shield Pt from dissolution. When Pt−O is reduced, Pt^{2+} is released either via

an electrochemical or chemical reaction (see Table 2.3) [16]. It is important to note that Pt dissolution rates are thereby dependant on the AST design i.e the upper and lower reversal potentials and the applied voltage profile [16].

Table 2.3: Pt dissolution reactions induced by potential cycling (negative sweep direction) [16].

Electrochemical Pt Dissolution	Chemical Pt Dissolution
$PtO_2 + 4\ H^+ + 2\ e^- \longrightarrow Pt^{2+} + 2\ H_2O$	$PtO + 2\ H^+ \longrightarrow Pt^{2+} + H_2O$

At constant potential above 1.2 V carbon corrosion with acclerated CO_2 formation can be observed [47]. However, the degradation effects are generally more severe under potential cycling than under constant potential stress.

It is important to note, that a RDE accelerated stress test can only show trends for the catalyst stability, as the real fuel cell environment is much more complex. Parameters such as pressure, temperature, pH, type of acid in the fuel cell and the duration of the test in a half cell or a complete fuel cell affect the stability of a Pt/C or Pt-alloy catalyst [6].

3 Results and Discussion

The results presented in the master thesis of Christoph Grimmer [48] on the synthesis of PtCo/C catalysts were used as a starting point for this work. The focus was on adapting the simple and up-scalable production process studied in this previous work for PtFe/C catalysts and on its subsequent optimization.

In general, the PtFe/C catalysts for the ORR were manufactured by a simple impregnation procedure (Fig. 3.1). Pre-prepared gas diffusion electrodes (GDE) provided by elcomax GmbH München, which consisted of a knife-coated carbon layer on a gas-permeable carbon-based support, were impregnated with a precursor solution containing Pt and Fe salts and a reducing agent, here ethylene glycol. The precursor salts were then reduced to PtFe nanoparticles at elevated temperatures. During the reduction process two important processes direct the particle formation - nucleation and particle growth. Nucleation occurs when the system is far from equilibrium, and particle growth is important at near equilibrium conditions [38].

The catalysts were then modified by post-treatment steps such as leaching and heat-treatment to optimize their catalytic activity.

One of the biggest advantages of this method are its simple and variable production steps performed at rather low temperatures between 200 and 300 °C, which can be put together to a completely continuous and scalable manufacturing process. Most other processes include complicated batch reactions with several more or less expensive chemicals (see sec. 2.5.1). Usually with other methods the synthesis of the Pt catalyst on carbon and the manufacture of the electrode sheet is thereby done in two separate steps. In the method presented in this work, the resulting catalyst sheet can be instantly pressed to a MEA. Furthermore, as a long catalyst sheet can be manufactured in a continuous process, production of catalyst sheets for a

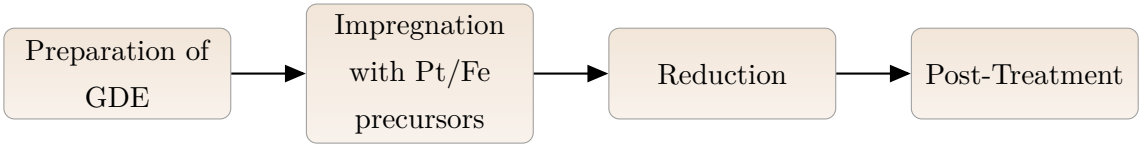

Figure 3.1: Simplified scheme of the synthesis procedure.

whole fuel cell stack is much less time-consuming. However, compared to batch reactions, the distribution of the precursor salts is more challenging in this method, because the carbon is not dispersed through mixing. Therefore the focus was on the optimization of the precursor solution composition and of the synthesis process.

Characterization of the prepared PtFe/C catalysts was performed with cyclic voltammetry by means of thin-film rotating disk electrode measurements. The results of the different experimental series are discussed in the following chapters. The CVs in N_2, the ORR curves in O_2 and the Tafel plots are shown for each of the experimental sets. The diagrams are all scaled the same, so that not only the curves in one plot, but all obtained curves can be compared with each other. The voltage is always given in regard to the reversible hydrogen electrode (RHE).

The three important factors to quantify the catalyst activities are the electrochemical surface area (ECSA), the specific current density (SCD) and the mass activity (MA), which are listed in tables for all samples. Furthermore the Tafel slope calculated by a linear fit in the range of 0.88 V and 0.96 V is given in the result tables as well. However, because the ORR curves were recorded with a rather high scan rate of $50\,\mathrm{mV\,s^{-1}}$ (whereat equilibrium conditions can not be guaranteed), the resulting Tafel slope values are mainly only comparable with each other.

After optimization of the nanoparticle synthesis accelerated stress tests (AST) were performed to test the catalyst's stability toward high potential cycling. The results given in % loss of the initial ECSA after each of the three cycles (with 555 cycles each) are depicted in separate tables.

3.1 Sample Preparation

As precursor salts $H_2PtCl_6 \cdot 6\,H_2O$ and $Fe(NO_3)_3 \cdot 9\,H_2O$ were chosen due to their excellent solubility in water, which resulted in a clear impregnation solution. With 2-propanol and ultra-pure water as solvents, and the slightly viscous reducing agent ethylene glycol in the ratio 1:1:1.4 an even impregnation film over the whole surface of the GDE-sheets could be obtained. Moreover the tenside polyoxyethylene-4-lauryl ether, traded under the name Brij30®, was added to the impregnation solution in order to prevent agglomeration of the nanoparticles at the reduction step. This non-ionic surfactant has the advantage of being liquid at room temperature, making it easier to process compared to other surfactants of this class, which have a more wax-like consistency.

Impregnation was done by carefully pipetting the appropriate amount of precursor solution onto the sheet. It was important that there occurred no loss of impregnation solution by spilling over the edge of the pad or by wetting through the sheet. The uniform vaporization of the

solvents was assured by careful manual distribution of the solution during the drying step (see fig 3.2(a)).

The reduction was performed in a muffle oven under N_2 atmosphere at temperatures between 200 and 300 °C. From previous studies it was concluded that 10 min reduction time were sufficient to reduce the Pt and Fe cations. The resulting pad had usually a dry, more rough surface than the non-impregnated GDE sheets (see Fig. 3.2(b)). With some samples, parts of the carbon layer crumbled off at the edges after the reduction indicating too fast vaporization of remaining solvent or too high temperatures. Therefore, complete drying of the sheet before the reduction step proved to be of importance. Generally, the whole manufacturing process was restricted to temperatures < 300 °C due to the limited thermal stability of the carbon layer of the GDE pads.

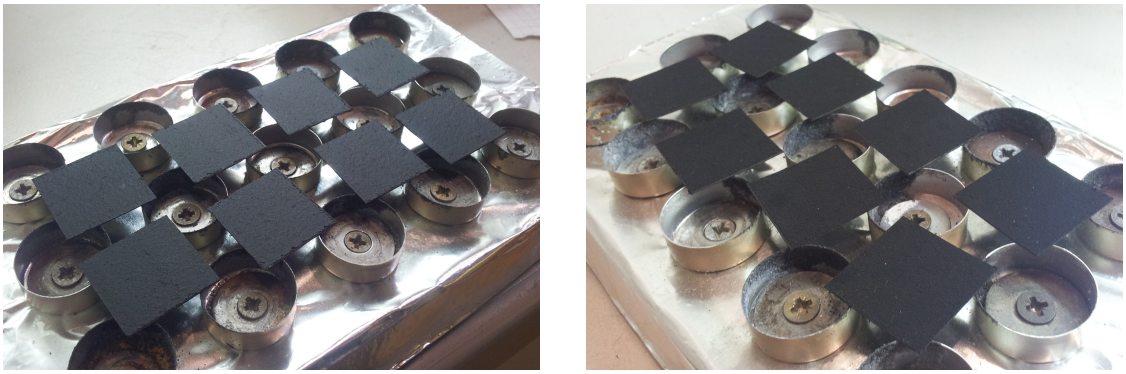

(a) After drying (b) After reduction

Figure 3.2: Impregnated GDE sheets after the drying step and after the reduction, exhibiting different surface appearances.

Afterwards the prepared catalysts were washed for 30 min in 2-propanol/ultra-pure water 1:1 and then thoroughly rinsed with fresh 2-propanol/ultra-pure water 1:1 to wash off remains of the reduction process. The washing solution was usually colored light orange probably indicating some loss of Fe. Washing was done with samples, which were heat-treated as (first) post-treatment step and with samples with no further treatment. The samples were then dried overnight at room temperature.

Leaching procedures were performed by putting the samples 30 min into a 2-propanol/ultra-pure water 1:1 solution with 10% acid. Afterwards the samples were washed in the same manner as the unleached ones in order to avoid contaminations on the catalyst by adsorbed ions from the acids. Again, the samples were then dried overnight at room-temperature.

Heat-treatment in the muffle oven in N_2 atmosphere presented another post-treatment step, subjecting the catalysts to varying temperature programs up to 300 °C. Higher heat-treating temperatures up to several hundred degrees in order to reach a higher degree of alloying of the two metals (often described in literature [38], see sec. 2.4.2), could not be applied for this catalysts synthesis method, because the thermal stability of the GDE sheets stated a limiting factor. However structural changes and a "cleaning"-effect (removal of surfactant and organic remains of the reduction process [38]) could be observed even at these rather low temperatures. The heat-treatment step was performed before or after the leaching or as the only post-treatment step.

To optimize the catalytic activity of the synthesized PtFe/C catalysts the manufacturing procedure and the settings and the order of the two post-treatment steps were varied.

3.2 Characterization Procedure

In preparation of the RDE measurements carried out in a 3-electrode set-up (see Fig. 3.3), a 16 mm circle was stamped out of the GDE pad and dispersed in a defined amount of 2-propanol (usually 3-4 mL) in an ultrasonic bath until a homogeneous suspension was obtained. Thereby a sonication time of about 15 to 30 min seemed to be sufficient as too long sonication resulted in larger carbon particles and a less homogeneous dispersion. After shaking the dispersion, 10 μL were pipetted carefully onto the glassy carbon centre of the electrode tip without wetting any of the surrounding Teflon®. This task became rather difficult, as no water, which forms a defined droplet on the glassy carbon and which does not wet the Teflon®, was added to the dispersion solution. Therefore the 10 μL were put onto the glassy carbon in two 5 μL portions with complete drying of the first portion in between. This stationary drying did not lead to a so-called "coffee-ring" [42] appearance of the thin-film (see Fig 3.6(a)). A reason for this could be the more hydrophobic composition of the carbon support, which could have caused an altered drying behavior compared to industrial Pt/C catalysts. Furthermore, as only 2-propanol was used as solvent, the drying was faster compared to solutions containing water.

Nevertheless, the quality of the film is crucial in order to obtain reliable measurements. As Garsany et al. [42] pointed out in their research, the thickness and homogeneity of the film has a big impact on the O_2 diffusion and thus on the ORR curves. Compared to that, the CV curves in N_2 are influenced far less by the film quality. Generally, the quality of the film is dependant on the utilized alcohol and its content in the dispersion solution, the quality of Pt dispersion, the room temperature and ambient humidity [44].

Figure 3.3: Cyclic voltammetry 3-electrode set-up with gas inlets.

After drying, the final Pt loading on the RDE was 28 µg cm^{-2}. This is in the range of the by Garsany et al. [44] recommended amount of 7-30 µg cm^{-2} for 10-50 wt% Pt/C catalysts.

The addition of water to the dispersion solution is frequently described in literature [42, 44]. However for this synthesis method, experiments showed that water resulted in a bad dispersion and a visible agglomeration of carbon on the wall of the glass vial as can be seen in Fig. 3.4. This negative effect is also apparent in the experimental results shown in Fig. 3.5, where three circles of one bigger catalyst sheet were dispersed in three different solutions containing either none, one-third or two-thirds of ultra-pure water. Although application of the catalyst onto the glassy carbon was easier, a dramatical apparent ECSA loss of 53% and 87%, respectively, and a significantly flatter ORR curve with an undefined mixed kinetic-diffusion controlled region was obtained. Probably the high hydrophobic nature of the carbon slurry on the GDE sheets, which contains Teflon® as a binder, is the reason for this behavior. All samples were therefore dried 10 min at 100 °C prior to the sonication in order to avoid the negative effect of water on the measurements.

Figure 3.4: Dispersion solution of a catalyst prepared on a GDE sheet with water added.

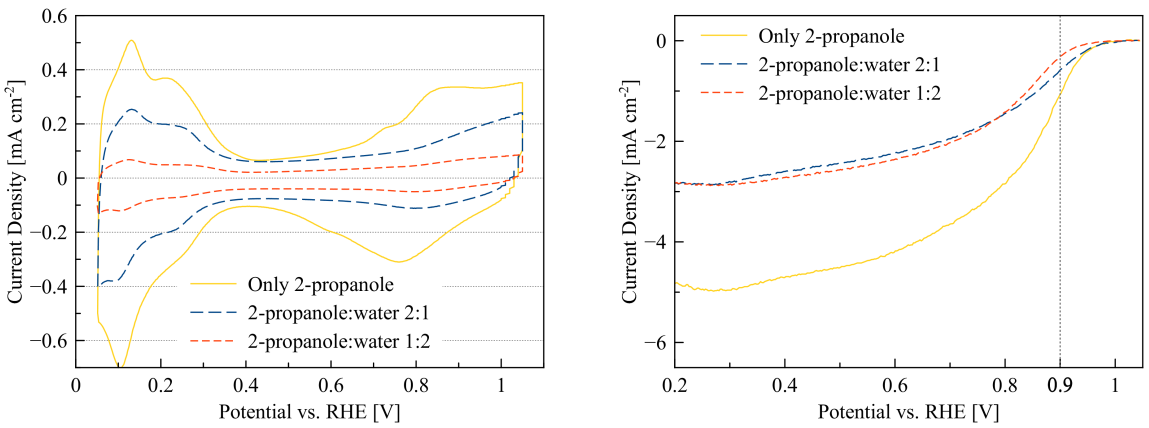

(a) CV curves in N_2

(b) ORR curves in O_2

Figure 3.5: Influence of the addition of water to the dispersion solution on the measurements of the same H_2SO_4 leached PtFe/C catalyst. The water content was varied thereby.

For the $NaBH_4$ batch synthesis method (described in sec. 3.10.2 and in the experimental section) a different approach was used in order to obtain a finely dispersed catalyst thin-film on the RDE. Because this PtFe catalyst was supported on carbon only with no additional Teflon® binder, ultra-pure water was added to the dispersion solution in the ratio water/2-propanol 70:30. As described in the work by Garsany et al. [42], the dispersion solution was pipetted onto a 180° turned-over RDE rotator and rotated at 700 rpm. With this "spin-coating"-like method a very even film could be obtained. Because of the addition of water, the droplet stayed on the glassy carbon area even when the RDE tip was rotated. A comparison of the films obtained with the two different catalyst application methods can be seen in Fig. 3.6.

(a) Static catalyst application (b) Catalyst application on rotated RDE

Figure 3.6: Applied PtFe/C catalyst films on the RDE.

3.2.1 Data Processing

Correction of the measured data curves is crucial in order to obtain reliable ECSA, SCD and MA values.

For the calculation of the ECSA from the integrated Pt−H desorption peak, the area must be corrected by the double-layer formation, which is the remaining current measured between 0.4 and 0.7 V_{RHE}. The correction is indicated in Fig. 2.9(a) in sec. 2.6.2 by a dashed green line. Furthermore, Stephens et al. [7] point out that for Pt alloy surfaces the coverage of adsorbed H* is not independent of surface structure and composition and appears to be lower than for pure

Pt due to the weaker Pt−H interaction. Despite this, measuring the ECSA with this method is still the easiest way, although the Pt alloy's ECSA can appear to be smaller than for pure Pt.

Also, the ORR curve must be corrected by several parameters, which have a big influence on the correctness of the obtained SCD and MA values. On one hand the measured ORR potentials have to be adjusted with the ohmic resistance of the measuring set-up and on the other with the real zero potential point of the reference hydrogen potential, which was measured frequently. As the conductivity of the electrolyte is temperature dependant, the ohmic resistance correction with the help of impedance spectroscopy becomes even more important [49]. However, in this work CV measurements were all carried out at room-temperature, so that the resistance was always around 30 Ω.

From the obtained ORR curve all currents, which are not caused by the oxygen reduction, have to be deducted. This means that the measured currents of the ORR curve are corrected by the currents of the CV curve in N_2-saturated electrolyte. The significance of this is demonstrated in Fig. 3.7, where a CV curve, an uncorrected and a corrected ORR curve are shown. Slight potential shifts have already a deep impact on the steep kinetically controlled region between 0.7 V and 1.0 V. Especially the current density at 0.9 V, which is important for the evaluation of the SCD and MA, is particularly affected.

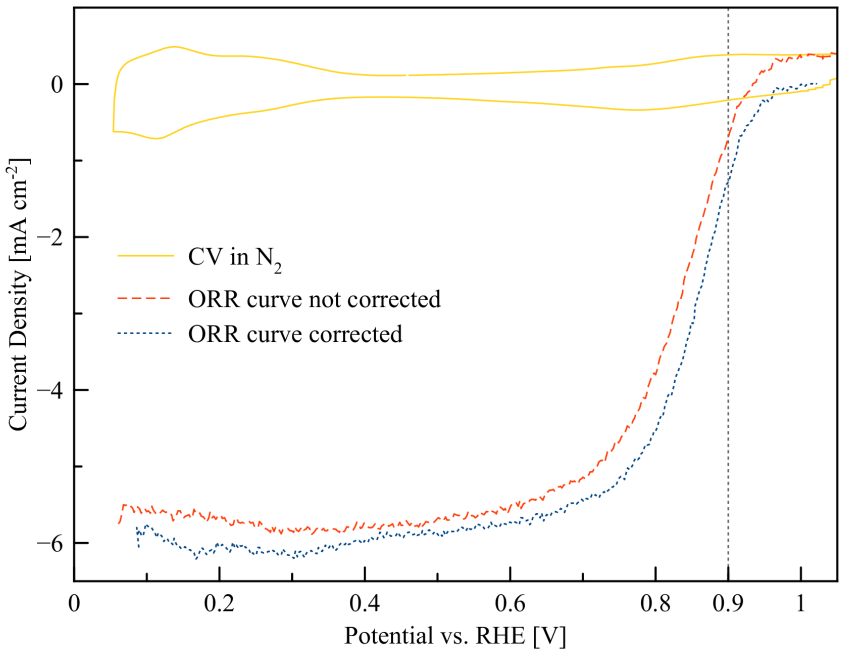

Figure 3.7: Influence of the ORR curve correction on the correctness of the measured catalytic properties.

3.3 Pt/Fe Ratio

In the first experimental set different molar ratios of Pt:Fe were studied. The Pt loading of $0.8\,\mathrm{mg\,cm^{-2}}$ was kept constant whereas the amount of Fe was varied. Although the amount of salt was varied, the solvent composition of the impregnation solution always was 1:1:1.4 2-propanol/ultra-pure water/ethylene glycol. A big excess of ethylene glycol to work as the reducing agent was thereby always assured (at least 10 electronic equivalents, e.g. for the Pt:Fe 1:10 sample). After the GDE impregnation, the salts were reduced for 10 min at 240 °C and washed afterwards. No post-treatment was done.

Samples with high Fe loading (no. 5 and 6) exhibited a distinctively rougher surface after the reduction. After washing the washing solution of samples no. 3 (Pt:Fe 1:3), no. 4 (Pt:Fe 1:5), and no. 5 (Pt:Fe 1:7) were colored the darkest orange as expected due to the higher Fe loading. The solutions of samples no. 1 (Pt:Fe 3:1) and no. 2 (Pt:Fe 1:1) showed nearly no coloring.

Table 3.1: Measured catalytic properties of samples with different Pt:Fe ratios.

No.	Ratio	Reduction	Post-Treatment	ECSA	SCD	MA	Tafel Slope
				$[\mathrm{cm^2\,mg^{-1}}]$	$[\mathrm{mA\,cm^{-2}}]$	$[\mathrm{A\,mg^{-1}}]$	$[\mathrm{mV\,dec^{-1}}]$
1	3:1	240 °C	-	91	0.309	0.028	70
2	1:1	240 °C	-	74	0.262	0.019	72
3	1:3	240 °C	-	85	0.414	0.035	66
4	1:5	240 °C	-	119	0.289	0.034	70
5	1:7	240 °C	-	110	0.287	0.032	68
6	1:10	240 °C	-	106	0.236	0.025	72

The CV curves for the catalysts with different ratios can be seen in Fig. 3.8. Although all of them exhibited ECSAs of only around $100\,\mathrm{cm^2\,mg^{-1}}_{Pt}$, the SCD and MA values are relatively high. Especially the MA of $> 0.035\,\mathrm{A\,mg^{-1}}_{Pt}$ for the Pt:Fe ratios 1:3, 1:5 and 1:7 indicated promising catalytic behavior for the PtFe/C system. Also the results of the Tafel plot seemed to be promising. All samples showed nearly the same slope indicating similar catalytic pathways on the surface [45]. The Tafel slope in this set was around $70\,\mathrm{mV\,dec^{-1}}$, which is only a little higher than the ideal slope of $60\,\mathrm{mV\,dec^{-1}}$ indicating a desired direct 4 e^- pathway (see sec. 2.3.2) as it is assumed for pure Pt [31]. However, the step in all ORR curves was rather undefined and the diffusion-limited current density small.

All in all, ratios with higher Fe content seemed to be more promising than the samples with low content (3:1 and 1:1), which exhibited a flat ORR curve and a very small ECSA with rather

undefined Pt adsorption/desorption peaks. On the opposite though, too high loading as with the 1:10 sample led to high mechanical stress on the carbon layer, making the whole process unreliable. Therefore, the ratios 1:5 and 1:7 were chosen for the following experiments.

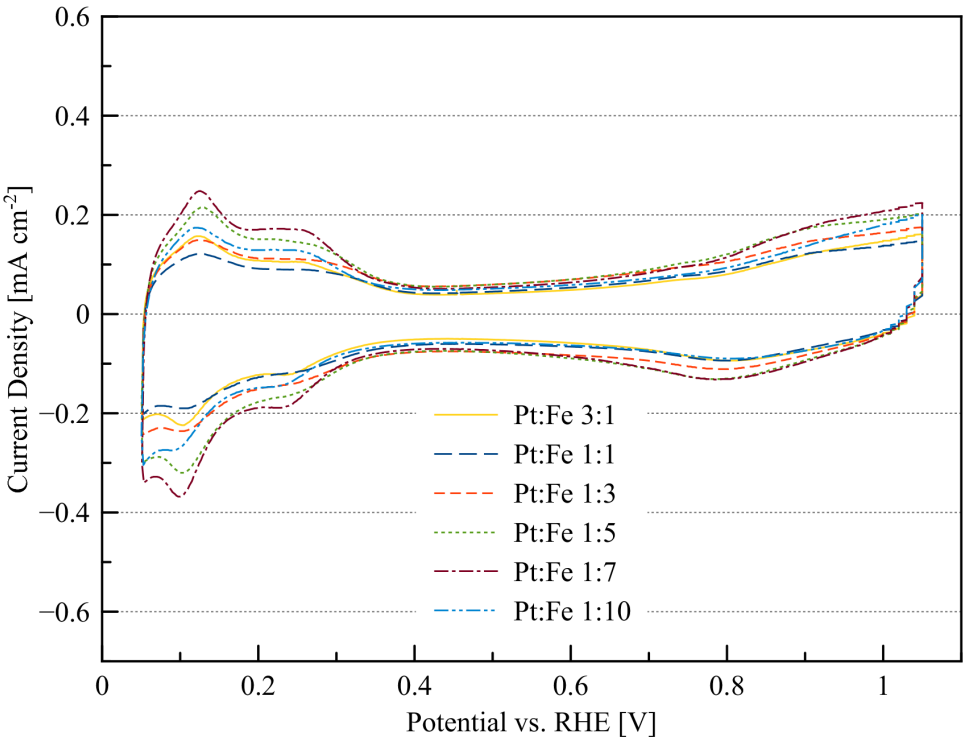

Figure 3.8: CV curves in N_2 of samples with different Pt:Fe ratios

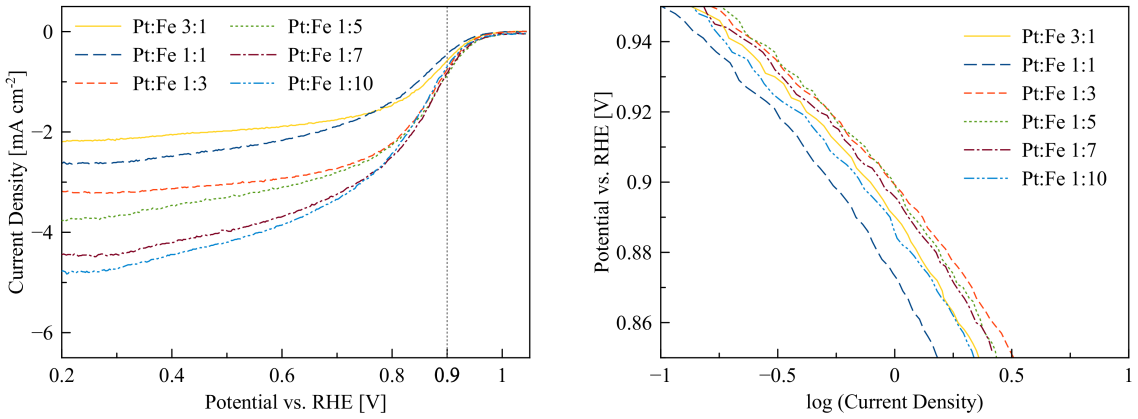

(a) ORR curves in O_2

(b) Tafel plot

Figure 3.9: ORR curves in O_2 and the corresponding Tafel plots of samples with different Pt:Fe ratios.

3.4 Reduction Temperature

In the first series the reduction temperature was set to 240 °C, based upon the results of the previous research on PtCo/C catalysts [48]. To validate if reduction temperature variations have an effect on the catalyst, samples with the chosen Pt:Fe ratios of 1:5 and 1:7 were prepared and reduced at temperatures between 210 and 280 °C. No post-treatment was done.

3.4.1 Pt/Fe 1:5

The 1:5 samples (No. 7, 4 and 8) showed all a similar ECSA of about 120 $cm^2\,mg^{-1}{}_{Pt}$ and also the ORR curves varied only a little as can be seen in Fig. 3.10 and 3.11. Change in reduction temperatures resulted in no significant improvement of catalytic performance.

Table 3.2: Measured catalytic properties of 1:5 samples reduced at different reduction temperatures.

No.	Ratio	Reduction	Post-Treatment	ECSA [$cm^2\,mg^{-1}$]	SCD [$mA\,cm^{-2}$]	MA [$A\,mg^{-1}$]	Tafel Slope [$mV\,dec^{-1}$]
7	1:5	210 °C	-	124	0.232	0.029	70
4	1:5	240 °C	-	119	0.289	0.034	70
8	1:5	280 °C	-	121	0.194	0.023	64

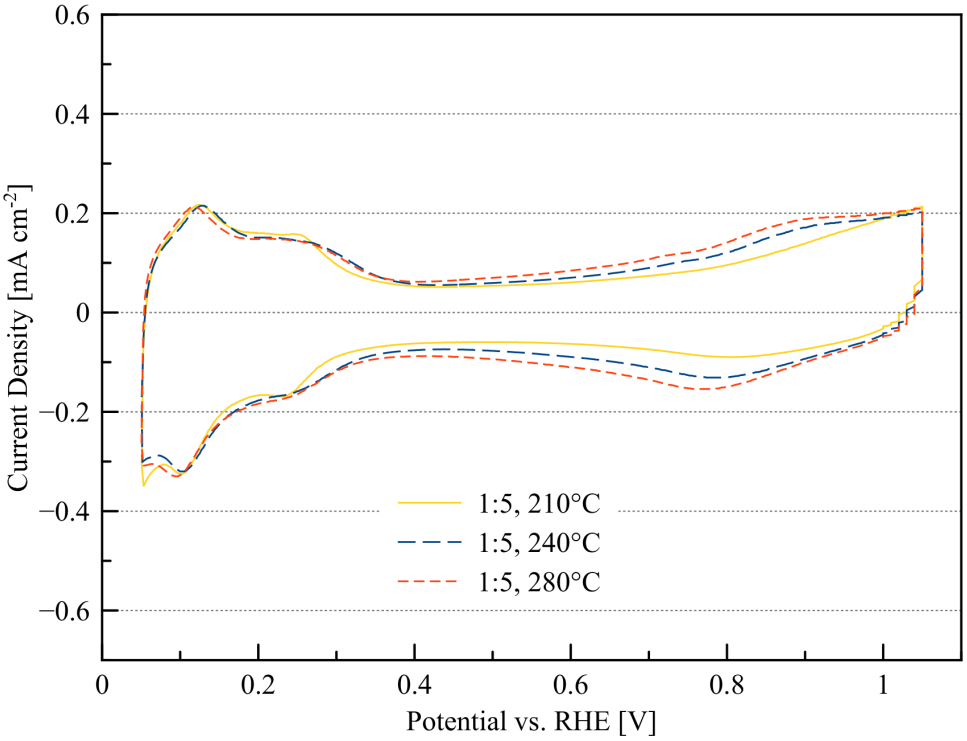

Figure 3.10: CV curves in N_2 of 1:5 samples reduced at different reduction temperatures.

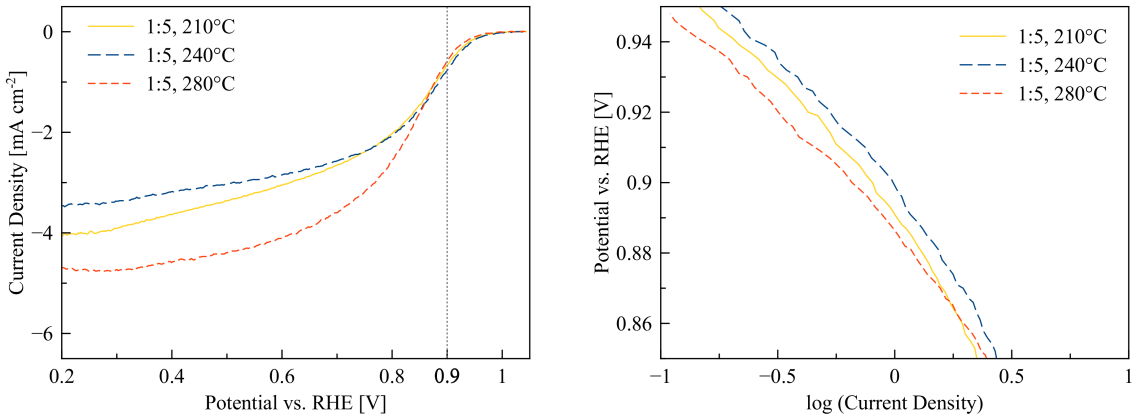

(a) ORR curves in O_2

(b) Tafel plot

Figure 3.11: ORR curves in O_2 and the corresponding Tafel plots of 1:5 samples reduced at different reduction temperatures.

3.4.2 Pt/Fe 1:7

Compared to the 1:5 samples described in sec. 3.4.1, the 1:7 samples had a much rougher surface. Especially with samples reduced at higher temperatures (280 °C, No. 12), crumbling of the carbon layer occurred. Some catalysts had to be prepared a second time in order to obtain a representative sample for CV measurements.

However, compared to the 1:5 samples, an influence of the reduction temperature on the catalytic activity and the ECSA was measured. Higher reduction temperatures lead to a significant increase in ECSA and MA as the results for samples no. 11 and 12 show. However, there are some inconsistencies such as the sudden ECSA increase of sample no. 11 compared to no. 10 or the wide range of the Tafel slope values, indicating that there are further important processing parameters to be considered. Furthermore, the high reduction temperatures lead to uneven and at some parts crumbled catalyst pads. This effect has to be completely avoided as it, complicates possible up-scaling of the process.

As the results were not completely conclusive and there is no clear trend between catalytic activity and reduction temperature, 240 °C and the higher reduction temperature of 280 °C were considered in the following experimental sets.

Table 3.3: Measured catalytic properties of 1:7 samples reduced at different reduction temperatures.

No.	Ratio	Reduction	Post-Treatment	ECSA	SCD	MA	Tafel Slope
				$[cm^2\,mg^{-1}]$	$[mA\,cm^{-2}]$	$[A\,mg^{-1}]$	$[mV\,dec^{-1}]$
9	1:7	210 °C	-	77	0.203	0.016	69
5	1:7	240 °C	-	110	0.287	0.032	68
10	1:7	250 °C	-	97	0.214	0.021	71
11	1:7	260 °C	-	230	0.166	0.038	62
12	1:7	280 °C	-	285	0.139	0.040	82

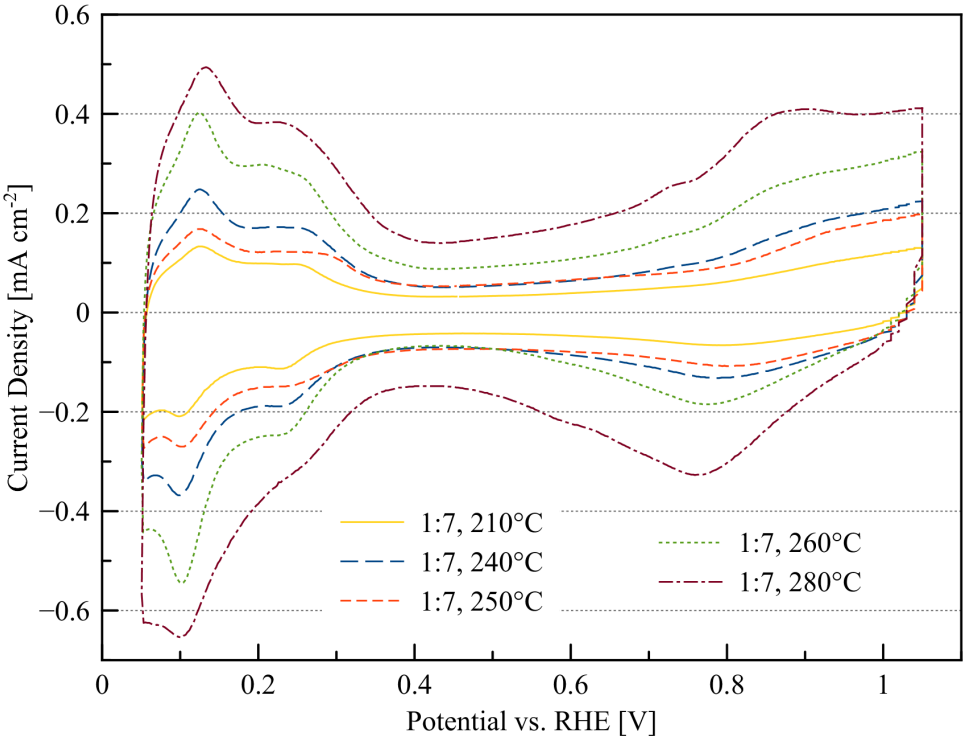

Figure 3.12: CV curves in N_2 of 1:7 samples reduced at different reduction temperatures.

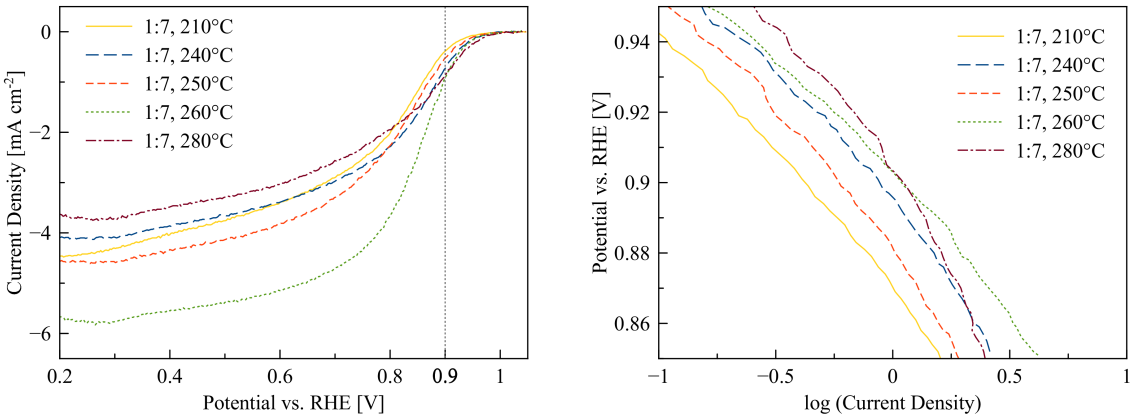

(a) ORR curves in O_2

(b) Tafel plot

Figure 3.13: ORR curves in O_2 and the corresponding Tafel plots of 1:7 samples reduced at different reduction temperatures.

3.5 Leaching

As described in section 2.4.1, leaching can have a significant influence on the PtFe nanoparticles by modifying their composition and surface. The effects induced by leaching were studied in several experimental sets on Pt:Fe 1:5 and 1:7 samples using H_2SO_4 and HCl as leaching acids. Previous studies on PtCo/C catalysts showed that a 10% solution of these acids in 2-propanol/ultra-pure water 1:1 yielded good results [48]. After 30 min of leaching the samples were put for 30 min in 2-propanol/ultra-pure water 1:1 and then thoroughly rinsed with these solvents in order to remove all acid remains.

3.5.1 Leaching of Pt:Fe 1:5 with H_2SO_4 and HCl (0.8 mg cm^{-2} Pt loading)

Although changing the reduction temperatures alone did not improve the catalytic activity of 1:5 samples as described in sec. 3.4.1, further experiments with 1:5 catalysts were performed to study the influence of the reduction temperature together with the leaching step. The samples were reduced either at 240 °C or 280 °C. The high temperature of 280 °C was chosen due to the promising results of sample no. 12 (1:7) (see Table 3.3). The catalysts were post-treated by leaching, either in diluted H_2SO_4 or HCl. With sample no. 17 both leaching acids were used one after the other with a washing step in between. The H_2SO_4 leaching solution usually were colored orange, whereas the HCl solutions turned instantly to a bright yellow, possibly due to the formation of iron chloride.

Table 3.4: Measured catalytic properties of 1:5 samples synthesized at different reduction temperatures and post-treated with different leaching acids.

No.	Ratio	Reduction	Post-Treatment	ECSA [cm^2 mg^{-1}]	SCD [mA cm^{-2}]	MA [A mg^{-1}]	Tafel Slope [mV dec^{-1}]
13	1:5	240 °C	H_2SO_4	156	0.118	0.018	67
14	1:5	240 °C	HCl	152	0.150	0.023	63
15	1:5	280 °C	H_2SO_4	154	0.233	0.036	64
16	1:5	280 °C	HCl	123	0.144	0.018	61
17	1:5	280 °C	H_2SO_4+HCl	120	0.195	0.023	62

As can be seen in Fig. 3.14, there is no significant improvement of ECSA, neither for samples reduced at low temperatures nor at high temperatures. Also the type of acid seems to have only little impact on the ECSA. For samples no. 13-14 the ECSA is only about 30 cm^2 mg^{-1} bigger than the ECSA of unleached 1:5 samples (no. 7, 4 and 8; see Table 3.2). For the other two

leached samples the ECSA is nearly the same as for the unleached. Again the ORR curves were rather flat and with the exception of sample no. 15 all MAs were $\leq 0.023\,\mathrm{mA\,cm^{-2}}$. However, all Tafel slopes were slightly lower than for the unleached samples, which probably indicates a positive effect of leaching on the catalytical behavior of the nanoparticle's surface. All in all, the effect of reduction temperature and acid was not conclusive. For all Pt:Fe 1:5 samples no significant improvement in catalytic activity through the leaching process could be observed.

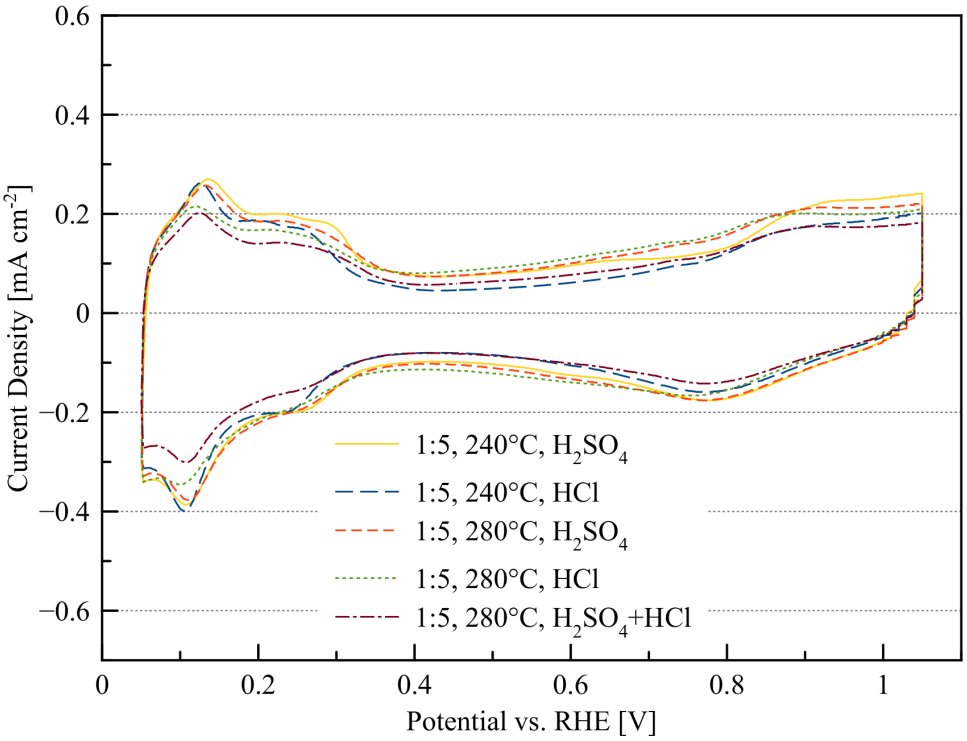

Figure 3.14: CV curves in N_2 of 1:5 samples synthesized at different reduction temperatures and post-treated with different leaching acids.

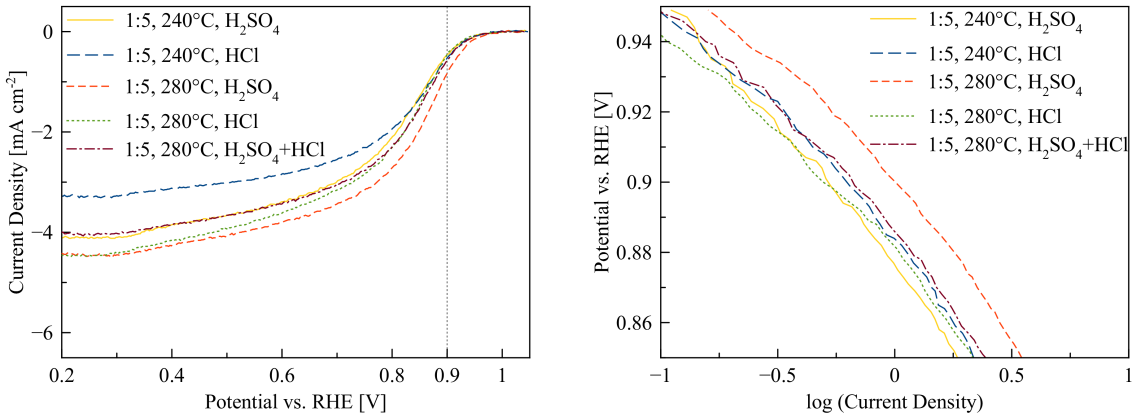

(a) ORR curves in O_2

(b) Tafel plot

Figure 3.15: ORR curves in O_2 and the corresponding Tafel plots of 1:5 samples synthesized at different reduction temperatures and post-treated with different leaching acids.

3.5.2 Leaching of Pt:Fe 1:7 with H_2SO_4 and HCl (0.8 mg cm^{-2} Pt loading)

Although the leaching of the 1:5 samples did not lead to a significant catalytic improvement, leaching experiments were performed with the second promising Pt:Fe ratio of 1:7. Figure 3.16 shows a comparison of 1:7 samples, which were all reduced at 240 °C but leached differently.

Samples no. 18 and 19, leached for 30 min in H_2SO_4 and HCl, respectively, exhibited high ECSAs of 318 and 271 cm^2 mg$^{-1}{}_{Pt}$, which means a two to three-fold increase of the catalytic surface area compared to the unleached catalyst (sample no. 5, see Table 3.1). Probably a big amount of Fe was leached from the unalloyed PtFe nanoparticles, leaving behind a "Pt-skeleton" type surface, as described in sec. 2.4.2. This surface type is characterized by a Pt-rich composition and a highly corrugated surface.

Longer leaching times (samples no. 20 and 21) were tried as well by leaving the pads in the acid solutions overnight. However, the results indicate that long leaching periods did not have a positive effect on the catalysts. Especially the H_2SO_4-leached sample lost two-thirds of its ECSA and half of its MA, when compared to the sample leached for only 30 min. Probably this is caused by an increased blocking of free catalyst sites by adsorbed sulfate ions, which could not be removed sufficiently enough by the washing procedure after the leaching. Also degradation and modification effects by the acidic environment e.g. on the carbon support could be an explanation. Both long-time leached samples showed a late onset of oxygen reduction indicated by a shift of the ORR curve towards lower potentials. In the corresponding Tafel plot (see Fig. 3.17) the two 24 h leached samples can be seen clearly shifted to lower current

densities in contrast to the samples leached only for 30 min. In conclusion, longer leaching time did not lead to an improvement of catalytic behavior, but instead to a dramatic decrease.

Similar to the 1:5 samples, using both acids one after another resulted in a decrease in catalytic activity compared the samples leached in only one acid. Perhaps the long leaching time (two times 30 min with a washing step in between) and/or remaining acid ions adsorbed on the surface could cause this effect. However, compared to the unleached sample, even this leaching process yielded a slightly improved catalytic performance, giving proof of the positive modifying effects of acid leaching on the PtFe/C catalysts.

When comparing both acids with each other, HCl-leached samples show a more defined step in the ORR curve, a steeper mixed kinetic-diffusion limited region and a well-defined diffusion-limited plateau. The flatter ORR curve of H_2SO_4-leached samples could be caused by blocking of catalysts surface by adsorbed sulphate anions. This is again an indication for the importance of a thoroughly washed catalyst and a clean, uncontaminated measuring set-up. However, sample no. 18 still exhibited the best results so far, thus H_2SO_4 was used a leaching acid in the next experimental set.

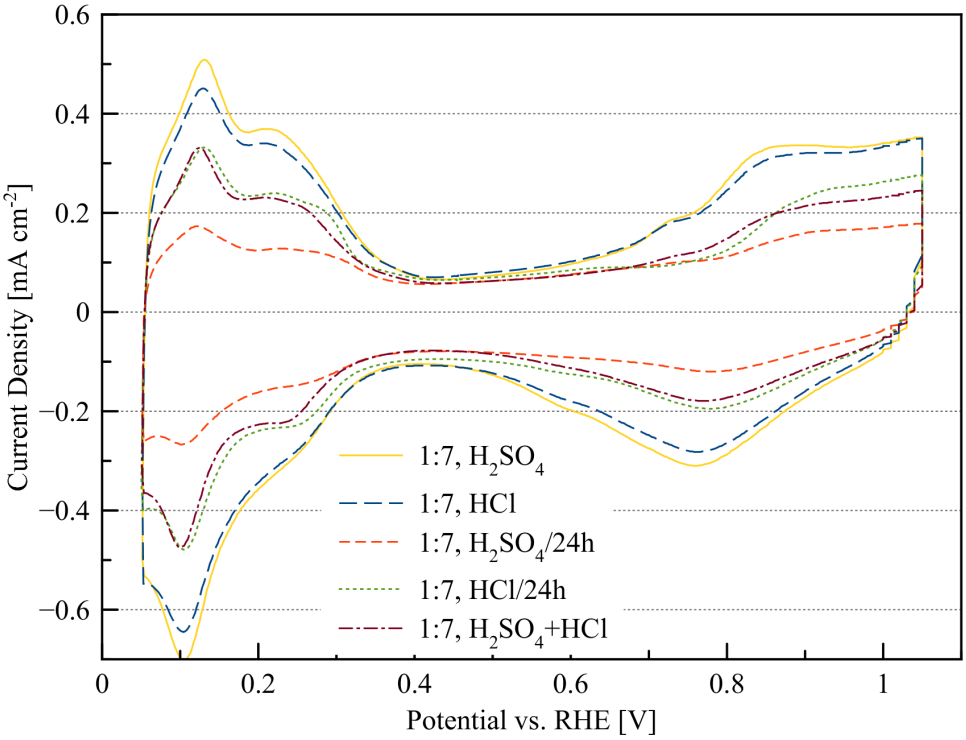

Figure 3.16: CV curves in N_2 of 1:7 samples (reduced at 240 °C) post-treated with different leaching acids.

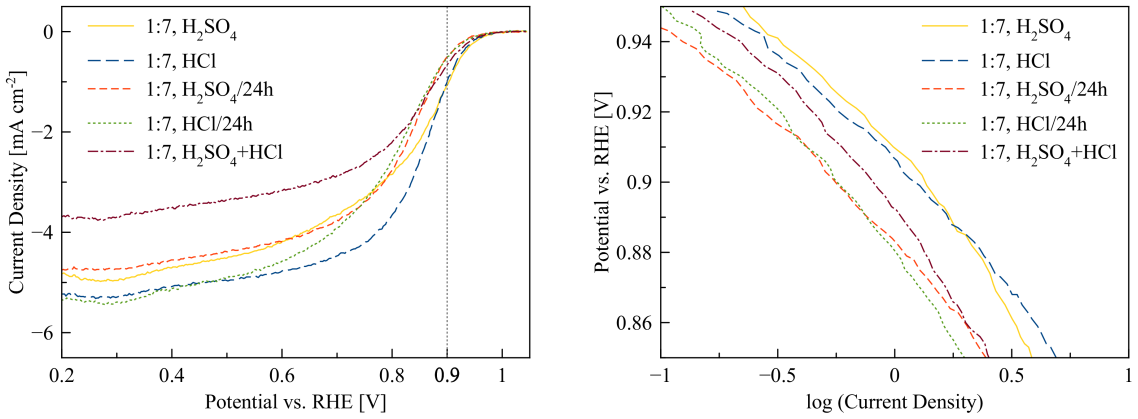

(a) ORR curves in O_2

(b) Tafel plot

Figure 3.17: ORR curves in O_2 and the corresponding Tafel plots of 1:7 samples (reduced at 240 °C) post-treated with different leaching acids.

Table 3.5: Measured catalytic properties of 1:7 samples (reduced at 240 °C) post-treated with different leaching acids.

No.	Ratio	Reduction	Post-Treatment	ECSA [$cm^2\,mg^{-1}$]	SCD [$mA\,cm^{-2}$]	MA [$A\,mg^{-1}$]	Tafel Slope [$mV\,dec^{-1}$]
18	1:7	240 °C	H_2SO_4	318	0.150	0.048	65
19	1:7	240 °C	HCl	271	0.161	0.044	60
20	1:7	240 °C	H_2SO_4/24h	101	0.203	0.020	62
21	1:7	240 °C	HCl/24h	197	0.107	0.021	68
22	1:7	240 °C	H_2SO_4+HCl	191	0.148	0.028	67

3.5.3 Varying Reduction Temperature for Pt:Fe 1:7/H_2SO_4 (0.8 mg cm^{-2} Pt loading)

The influence of reduction temperature on the catalysts was not conclusive in the first experiments and did not follow a clear trend. To optimize the reduction process samples reduced at different temperatures and leached in H_2SO_4 were compared.

As can be seen in Fig. 3.18 sample no. 18 reduced at 240 °C exhibits still the most defined CV curve with the highest ECSA. Interestingly, samples reduced at higher temperatures (no. 24 and 25) showed an increased double-layer formation in the potential region between 0.4 and 0.7 V. Although the reduction was performed in a N_2-flushed oven chamber (100 L h^{-1}), traces of oxygen could have possibly led to an increased surface oxidation of the high surface area carbon.

This effect can also be seen in already discussed samples such as no. 11 and 12 (see Fig. 3.12), which were reduced at 260 °C and 280 °C. Also the leached 1:5 samples in section 3.5.1 exhibited a slightly broader double-layer region when reduced at 280 °C, although the effect there is less pronounced due to the overall small ECSA of these samples.

As with previously mentioned H_2SO_4-leached samples, the ORR curves do not show a distinctive step, but rather a continuous slope between 0.2 and 0.8 V. Though the values taken at 0.9 V resulted in good SCDs and MAs, the Tafel slope has values $> 70\,\mathrm{mV\,dec^{-1}}$, which indicates a less favorable ORR pathway. Again, a higher ratio of adsorbed oxides on the surface could give an explanation for this behavior, as a Tafel slope closer to $> 120\,\mathrm{mV\,dec^{-1}}$ is associated with Pt−O formation (described in sec. 2.3.2).

From this experimental set it was concluded that reduction at higher temperatures can modify the catalyst sheets unfavorably by changing the carbon support and by stressing and crumbling the carbon layer. Two samples reduced at 280 °C crumbled too much to be measured, illustrating clearly the thermal limitations of the GDE sheets for this catalyst manufacturing method. Moreover, the ECSA and MA were slightly lowered and the Tafel slope rose clearly. Therefore, the reduction temperature was set to 240 °C for the following optimization steps.

When comparing the two Pt:Fe ratios (1:5 and 1:7), the 1:7 experimental series yielded overall significantly better results than the 1:5 set. There was a trend that leaching has a bigger influence on the 1:7 samples than on the 1:5 samples, which is probably caused by the higher Fe content. For all the following experiments the Pt:Fe ratio was thus set to 1:7.

Table 3.6: Measured catalytic properties of 1:7 samples reduced at different reduction temperatures and leached in H_2SO_4.

No.	Ratio	Reduction	Post-Treatment	ECSA	SCD	MA	Tafel Slope
				$[\mathrm{cm^2\,mg^{-1}}]$	$[\mathrm{mA\,cm^{-2}}]$	$[\mathrm{A\,mg^{-1}}]$	$[\mathrm{mV\,dec^{-1}}]$
18	1:7	240 °C	H_2SO_4	318	0.150	0.048	65
23	1:7	250 °C	H_2SO_4	159	0.193	0.031	73
24	1:7	260 °C	H_2SO_4	249	0.177	0.044	74
25	1:7	270 °C	H_2SO_4	243	0.141	0.034	79

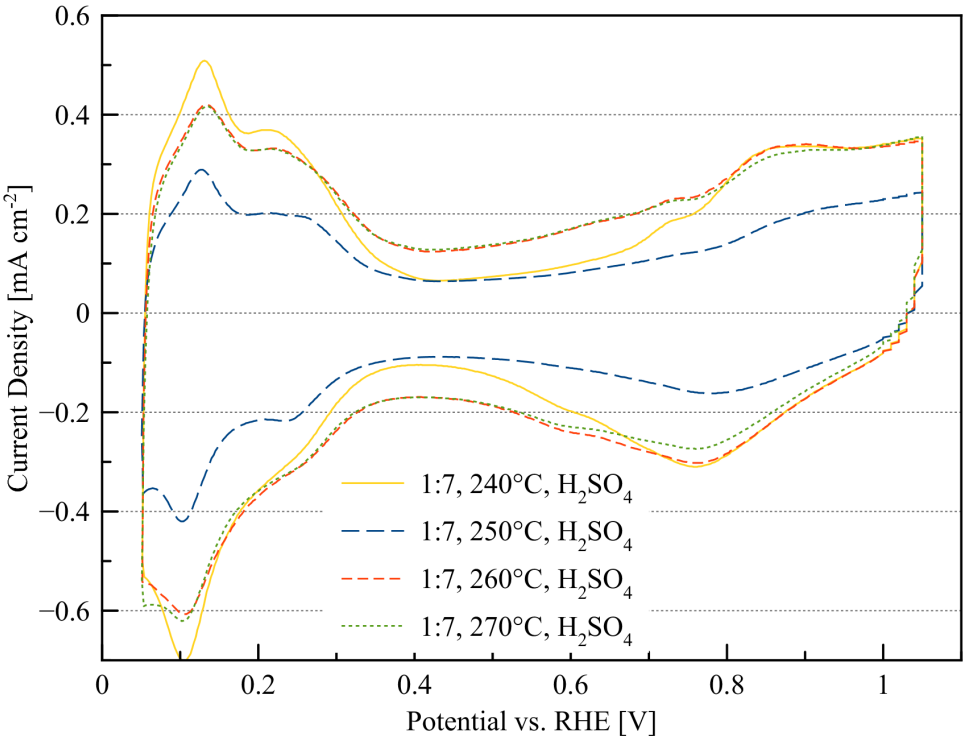

Figure 3.18: CV curves in N_2 of 1:7 samples reduced at different reduction temperatures and leached in H_2SO_4.

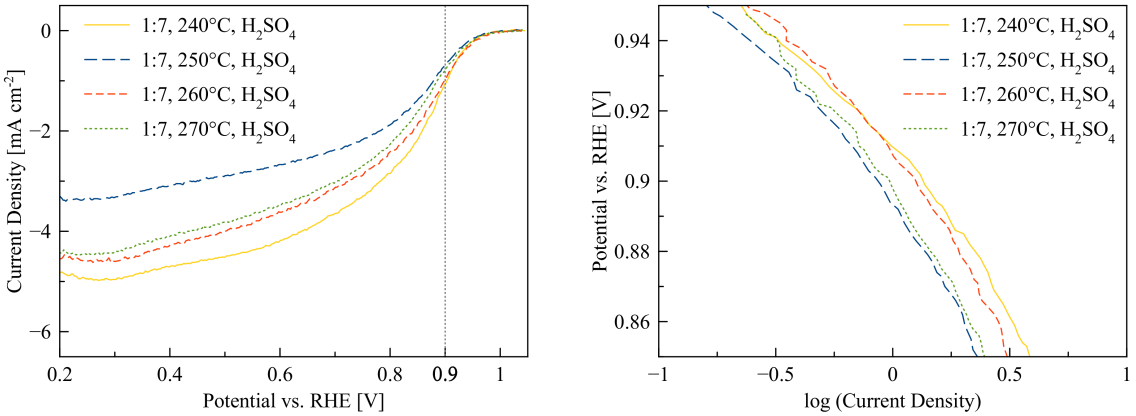

(a) ORR curves in O_2

(b) Tafel plot

Figure 3.19: ORR curves in O_2 and the corresponding Tafel plots of 1:7 samples reduced at different reduction temperatures and leached in H_2SO_4.

3.5.4 Leaching of Pt:Fe 1:7 with H_2SO_4 and HCl (1.0 mg cm^{-2} Pt loading)

All samples in the previous sets were manufactured with a Pt loading of 0.8 mg cm^{-2} on the GDE. For comparison the PtCo/C catalysts studied in the master thesis of Christoph Grimmer were synthesized with a Pt loading of 1.0 mg cm^{-2}. However, it was suspected that this reduction could have a negative effect on the suitability of the catalysts sheets for in-situ testing in HT-PEM fuel cells. Therefore, the Pt loading was raised to 1.0 mg cm^{-2} for the following experimental sets. The amount of Fe was raised accordingly, however the solvent's quantity stayed the same in order to impregnate the GDEs with the same amount of solution. Although both salts were still completely soluble, the impregnation solution became a little bit more viscous due to the higher salt content. The amount of solvent for the dispersion solution was raised in order to obtain the same Pt loading on the RDE of 28 µg cm^{-2}, thus making all CV measurements and the normalized activity parameters comparable with each other.

In this series the catalytic performance of the catalysts synthesized with the altered impregnation solution and the influence of the leaching acid on these samples was studied. As done in previous experiments the samples were leached in H_2SO_4 (no. 26), and in H_2SO_4 and HCl one after another with a washing step in between (no. 28). Sample no. 27 was leached in a solution containing both, 10% H_2SO_4 and 10% HCl.

The CV curves shown in Fig. 3.20 are nearly identical for all three samples and also the ORR activity is nearly the same. Although these samples had a different Pt loading, they exhibited similar ECSAs and MAs as the catalyst with lower Pt content (see sample no. 18) indicating no big change of the catalyst system by the higher amount of Pt on the GDE.

Although these samples were leached in H_2SO_4, the ORR curves shown in Fig. 3.21 exhibited a defined step and a flat diffusion controlled region. It seems that either these samples were washed more thoroughly with less unwanted adsorbed anions, and/or the catalyst system with the higher Pt loading is more robust to contamination - a property, which could be an advantage for fuel cell applications. Moreover, all three Tafel slopes were close to the ideal value of 60 mV dec^{-1}. These results clearly indicate, that it is unnecessary to a apply a more complicated leaching process and that just using H_2SO_4 for leaching already improves the catalysts significantly.

In addition, degradation experiments (AST) were performed in order to evaluate the stability of the catalysts after leaching. Because all three samples had ECSAs of $> 250\,\mathrm{cm^2\,mg^{-1}}_{Pt}$, evaluation of the ECSA loss in % was possible. The results are shown in Table 3.8. For all three samples the loss after the third AST cycle was about 30% indicating again no major influence of the applied leaching procedures.

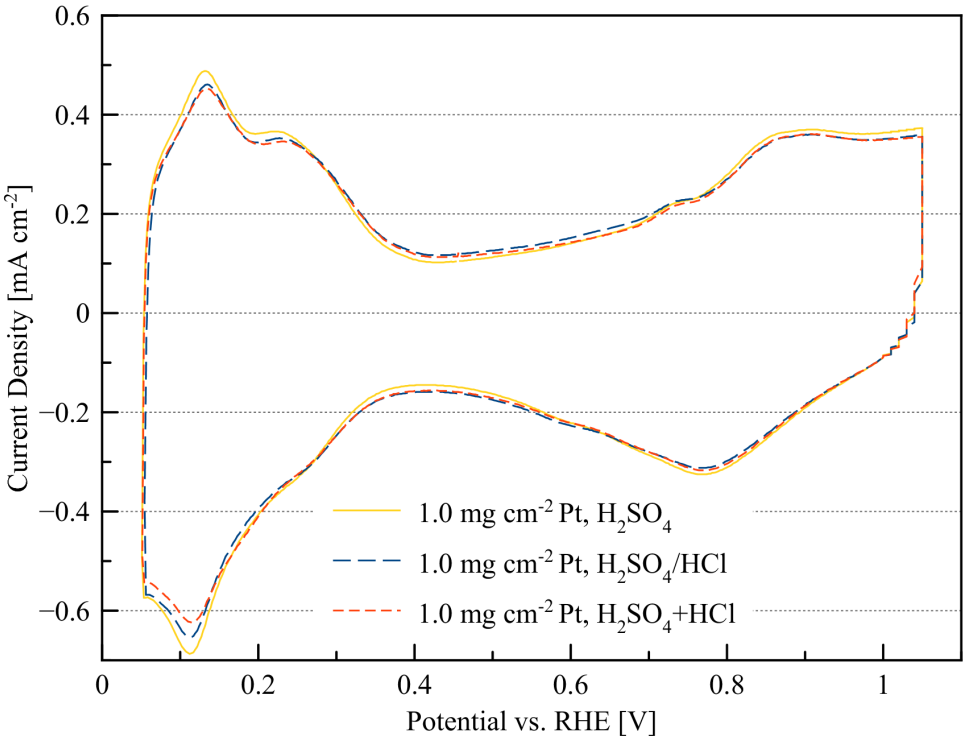

Figure 3.20: CV curves in N_2 of 1:7 samples (1.0 mg cm^{-2} Pt loading) post-treated with different leaching acids.

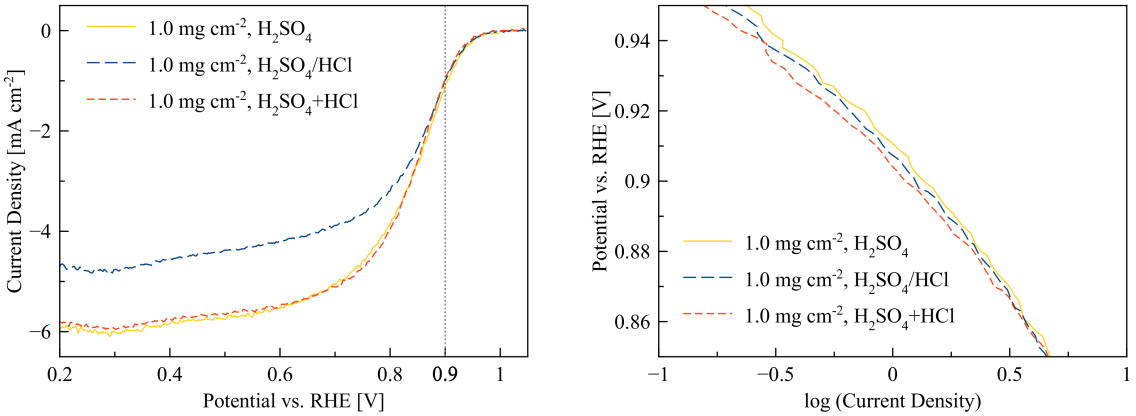

(a) ORR curves in O_2

(b) Tafel plot

Figure 3.21: ORR curves in O_2 and the corresponding Tafel plots of 1:7 samples (1.0 mg cm^{-2} Pt loading) post-treated with different leaching acids.

Table 3.7: Measured catalytic properties of 1:7 samples (1.0 mg cm^{-2} Pt loading) post-treated with different leaching acids.

No.	Ratio	Reduction	Post-Treatment	ECSA [cm^2 mg^{-1}]	SCD [mA cm^{-2}]	MA [A mg^{-1}]	Tafel Slope [mV dec^{-1}]
26	1:7	240 °C	H_2SO_4	300	0.159	0.048	64
27	1:7	240 °C	H_2SO_4/HCl	282	0.160	0.045	62
28	1:7	240 °C	H_2SO_4+HCl	274	0.147	0.040	60

Table 3.8: AST results of 1:7 samples (1.0 mg cm^{-2} Pt loading) post-treated with different leaching acids.

No.	Post-Treatment	Initial ECSA [cm^2 mg^{-1}]	% Loss 1^{st} AST cycle	% Loss 2^{nd} AST cycle	% Loss 3^{rd} AST cycle
26	H_2SO_4	300	24%	28%	33%
27	H_2SO_4/HCl	282	16%	25%	31%
28	H_2SO_4+HCl	274	12%	21%	29%

3.5.5 Summary of the Leaching Experiments

Compared to the obtained electrochemical active surface area and the catalytic activity of the synthesized catalysts with no post-treatment, leaching caused a big improvement of catalytic performance. Especially the ECSA was nearly tripled when compared to the unleached 1:7 sample reduced at 240 °C. An explanation for this is the dissolution of a major portion of catalytically inactive Fe resulting in the formation of a "Pt-skeleton" surface. Thereby a bigger share of the Pt is exposed to the electrolyte.

Several parameters needed to be optimized. The Pt:Fe ratio of 1:5 was not used for further experiments as the leaching did not show any influence on the catalysts. Further experiments were hence focused on the ratio 1:7, which yielded significantly better results compared to the 1:5 samples. Variations in reduction temperatures and the leaching solutions led to a further optimized synthesis procedure. PtFe/C samples reduced at 240 °C and leached for 30 min in 10% H_2SO_4 exhibited the best activities. Raising the amount of Pt on the GDE to 1.0 mg cm^{-2} did not seem to change the catalytic properties significantly and the results were comparable to the 0.8 mg cm^{-2} samples.

3.6 Heat-Treatment

Besides leaching, heat-treatment was the second post-treatment approach applied on the PtFe/C catalysts with the aim to increase the stability of the catalysts. Again the research on PtCo/C catalysts [48] was used as a starting point for studying the effect of heat-treatment on PtFe/C, followed by the optimization of this step. This experimental set was done before the Pt loading was raised and hence all samples (no. 29 to 32) were still manufactured with a Pt loading of $0.8\,\mathrm{mg\,cm^{-2}}$. However, as the leaching experiments suggest, the results appear to be independent on the Pt loading. Therefore, it is possible to apply the results and conclusions of this set also to samples with a higher Pt loading of $1.0\,\mathrm{mg\,cm^{-2}}$.

After reducing the 1:7 samples at 240 °C, they were washed in 2-propanol/ultra-pure water 1:1 and dried overnight. Heat-treatment was performed in the muffle oven, again under N_2-atmosphere. In this experimental set the influence of different temperatures was studied, whereas the heat-treatment time was set to 1 h for all samples.

Table 3.9: Measured catalytic properties of 1:7 samples post-treated by heat-treatment at different temperatures.

No.	Ratio	Reduction	Post-Treatment	ECSA	SCD	MA	Tafel Slope
				$[\mathrm{cm^2\,mg^{-1}}]$	$[\mathrm{mA\,cm^{-2}}]$	$[\mathrm{A\,mg^{-1}}]$	$[\mathrm{mV\,dec^{-1}}]$
29	1:7	240 °C	200 °C/1h	146	0.115	0.017	62
30	1:7	240 °C	220 °C/1h	150	0.130	0.020	71
31	1:7	240 °C	240 °C/1h	182	0.116	0.021	58
32	1:7	240 °C	260 °C/1h	134	0.123	0.016	68

In contrast to the leached samples, which exhibited much bigger ECSAs compared to untreated samples, no big improvement of the ECSAs for the heat-treated catalysts was measured. Because the applied heat-treatment temperatures were rather low, no major rearrangement effects of the nanoparticles could be observed. As described in sec. 2.4.2 much higher temperatures (several hundred degrees) are needed to properly alloy both metals and also for significant sintering effects the temperatures were probably too low. The slight increase of the ECSAs can probably be explained by a temperature-induced cleaning effect of the surface, whereat remaining impurities and leftovers of the reduction process were removed. However, the corresponding ORR curves (Fig. 3.23) show a very late onset of the oxygen reduction for all four samples regardless of the applied temperature. This results in quite low mass activities and also the Tafel slope values are spread broadly.

Although the aim of this series was to study if heat-treatment could enhance the stability of the catalysts, no AST experiments could be performed. This was due to the small measured ECSAs, which did not allow meaningful and reliable evaluation of the ECSA loss.

In conclusion, this series showed that heat-treatment as the only post-treatment did not improve the PtFe/C catalysts. Although they exhibited slightly bigger ECSAs, the SCDs and MAs were significantly decreased.

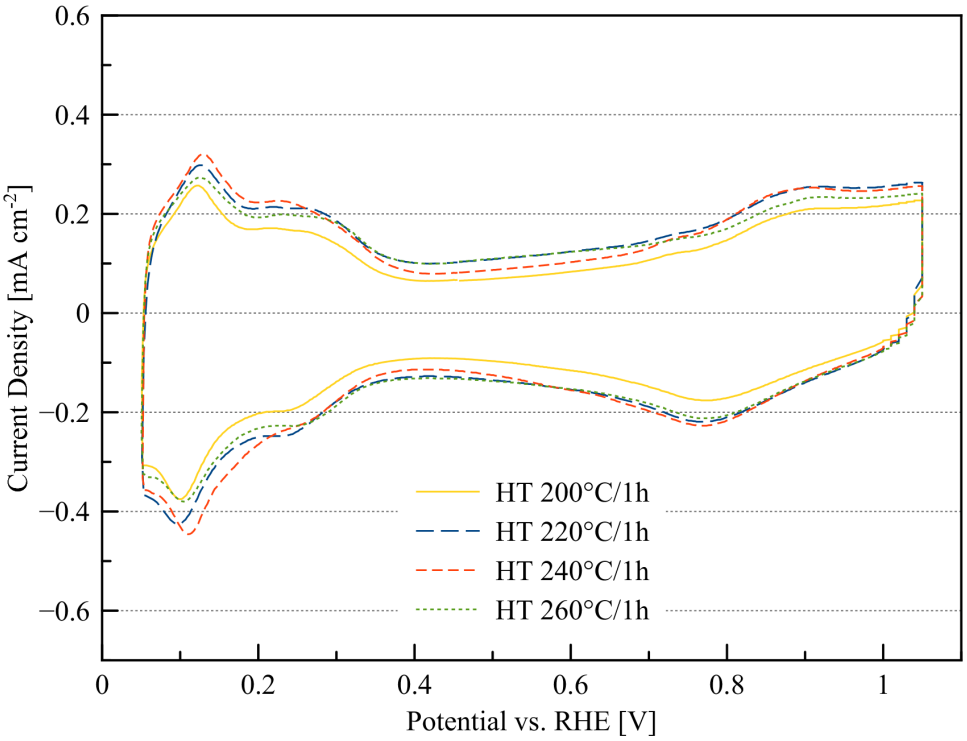

Figure 3.22: CV curves in N_2 of 1:7 samples post-treated by heat-treatment at different temperatures.

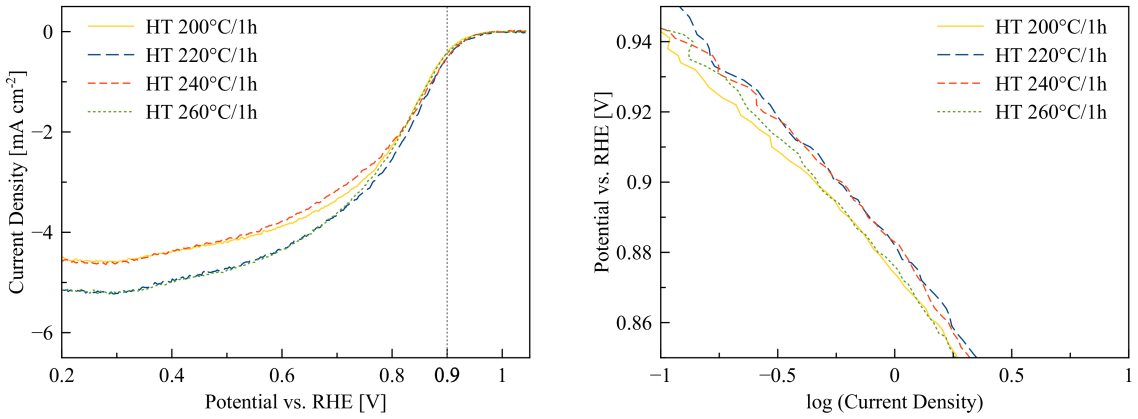

(a) ORR curves in O_2

(b) Tafel plot

Figure 3.23: ORR curves in O_2 and the corresponding Tafel plots of 1:7 samples post-treated by heat-treatment at different temperatures.

3.7 Leaching + Heat-Treatment

As leaching significantly improved the activity of the PtFe/C catalysts, the next goal was to raise the stability of the catalysts by introducing an additional heat-treatment step. In the experimental set with heat-treatment as the only post-treatment step, its effect on the catalyst's stability could not be measured due to the small ECSAs. Therefore, it was still necessary to study the effect of heat-treatment on the catalyst's stability. In the following experiments H_2SO_4-leached catalysts were treated in a second post-treatment set with different temperature programs under N_2-flow. AST experiments were performed to evaluate the stability.

All of the following catalysts were manufactured with a Pt loading of $1.0\,\mathrm{mg\,cm^{-2}}$ on the GDE.

3.7.1 With Ramped Heat-Treatment

In contrast to the only heat-treated samples described in sec. 3.6, which were put into the preheated oven, the samples in this series were treated with a temperature ramp. This was done in order to induce less stress on the carbon sheet. Thereby the temperature in the oven was raised slowly with a gradient of $5\,^{\circ}\mathrm{C\,min^{-1}}$ starting from room temperature. The final temperature between 200 °C and 260 °C was then held for 1 h.

Samples no. 33 and 36, heat-treated at 200 °C and 260 °C respectively, exhibited a significant decrease in ECSA (see Fig. 3.24) compared to the only leached samples. Also the MAs were lower. However, the ECSAs of samples no. 34 and 35, heat-treated at 220 °C and 240 °C

respectively, were only slightly decreased and especially the high MA of sample no.35 with a value of $0.054\,\mathrm{A\,mg^{-1}}_{Pt}$ is noteworthy.

Likely, the small ECSA decrease of those two samples can be assigned to the formation of a "Pt-skin" surface. Thereby the Pt atoms on the nanoparticles surface are rearranged, thus forming again a smoother surface. At the same time the number of under-coordinated sites is lowered (see sec. 2.4.2) and the Pt should be less prone to dissolution. Further indication of this temperature induced rearrangement process is given by its effect on the Tafel slope. Compared to the only leached catalysts, these samples show bigger differences in the Tafel slope indicating slightly different nanoparticle surfaces for each sample. However all values are quite close to the ideal slope of $60\,\mathrm{mV\,dec^{-1}}$.

Table 3.10: Measured catalytic properties of 1:7 samples leached in H_2SO_4 and heat-treated with different temperature programs.

No.	Ratio	Reduction	Post-Treatment	ECSA	SCD	MA	Tafel Slope
				$[\mathrm{cm^2\,mg^{-1}}]$	$[\mathrm{mA\,cm^{-2}}]$	$[\mathrm{A\,mg^{-1}}]$	$[\mathrm{mV\,dec^{-1}}]$
33	1:7	240 °C	H_2SO_4, 200 °C ramp/1h	161	0.187	0.030	56
34	1:7	240 °C	H_2SO_4, 220 °C ramp/1h	265	0.132	0.035	64
35	1:7	240 °C	H_2SO_4, 240 °C ramp/1h	260	0.208	0.054	68
36	1:7	240 °C	H_2SO_4, 260 °C ramp/1h	215	0.150	0.032	61

Due to the quite big ECSA, AST experiments could be performed for the three samples with an ECSA $> 250\,\mathrm{cm^2\,mg^{-1}}_{Pt}$ (no. 34-36). However, the results presented in Table 3.12 show that again about 30% of the initial ECSA was lost during the AST cycles, which is about the same as for only leached samples.

Although the catalyst heat treated at 240 °C (no. 35) exhibited already a good catalytic performance, further parameters in the heat-treatment procedure were studied in order to optimize the process.

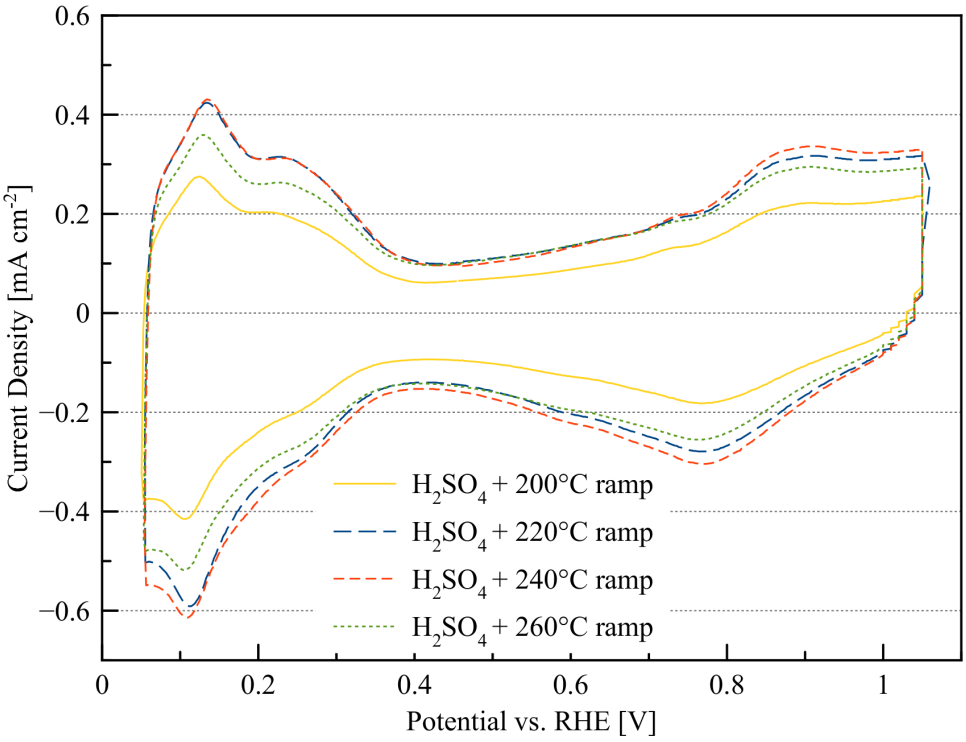

Figure 3.24: CV curves in N_2 of 1:7 samples leached in H_2SO_4 and heat-treated with different temperature programs.

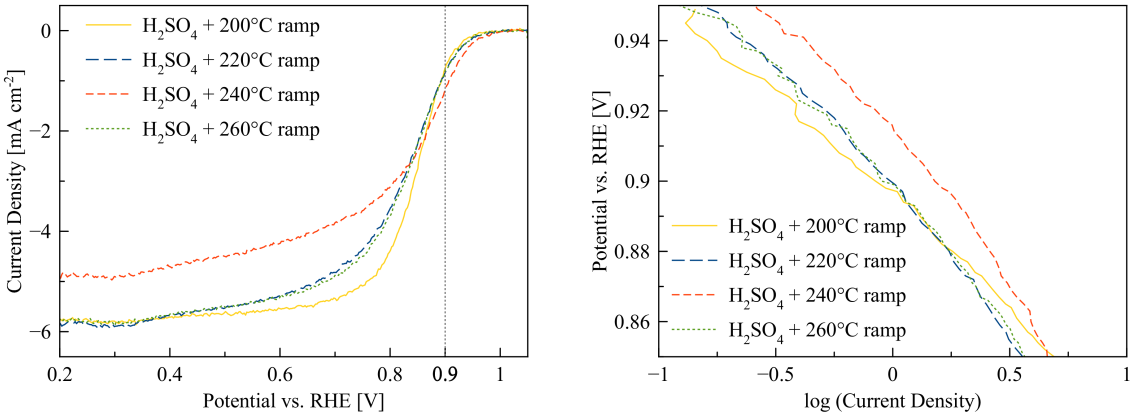

(a) ORR curves in O_2

(b) Tafel plot

Figure 3.25: ORR curves in O_2 and the corresponding Tafel plots of 1:7 samples leached in H_2SO_4 and heat-treated with different temperature programs.

3.7.2 Different Length of Heat-Treatment

For the following samples lower temperatures for the heat-treatment were used and also the difference between 1 h heat-treatment and 6 h was studied. After the leaching process in H_2SO_4, the samples in this set were heat-treated in the pre-heated oven without a temperature ramp.

As listed in Table 3.11, the catalysts heat-treated at lower temperatures (no. 37 and 38) had a rather small ECSA, but exhibited rather high SCDs and MAs. The two corresponding ORR curves were well-defined with a very steep mixed kinetic-diffusion controlled region (shown in Fig. 3.27). Interestingly, both samples yielded quite similar results, although sample no. 37 was heat-treated six times longer.

The influence of the length of heat-treatment can be evaluated more conclusively, when comparing samples no. 39 and 40 with each other. Both samples were treated the same, except that the latter was heat-treated 6 h instead of only 1 h. Interestingly, both samples exhibit nearly the same catalytic activity, with nearly identical CV and ORR curves. The only difference can be seen after the AST experiments, where sample no. 39, heat-treated for 1 h, had only an ECSA loss of only 18% after the third AST cycle. So far, this is the catalyst with the highest stability. But also the other sample (no. 40) with a loss of 25% was more stable toward high potential cycling than the only leached samples. Long-time heat-treatment does not seem to be better than heat-treatment for just 1 h. As it seems that 1 h is sufficient, it is not necessary to make the heat-treatment more complicated and time-consuming.

Concerning the parameters determining the catalysts activity and stability, further optimization has to be done. As the results suggest, there are several effects occurring at leaching (e.g. rearrangement of Pt atoms on nanoparticles, cleaning of the catalyst's surface, etc.), which need to be further studied in order to establish a reliable manufacturing process. However, according to the experimental results, heat-treatment at 240 °C yielded a good ECSA, ORR activity and especially a high stability. This higher stability gives proof of the usefulness of the heat-treatment, which - with further optimization - could render PtFe/C catalysts more durable for the highly acidic HT-PEMFC environment.

Table 3.11: Measured catalytic properties of 1:7 samples leached in H_2SO_4 and heat-treated at different temperatures for varying time lengths.

No.	Ratio	Reduction	Post-Treatment	ECSA	SCD	MA	Tafel Slope
				$[cm^2\,mg^{-1}]$	$[mA\,cm^{-2}]$	$[A\,mg^{-1}]$	$[mV\,dec^{-1}]$
37	1:7	240 °C	H_2SO_4, 160 °C/6h	157	0.257	0.040	62
38	1:7	240 °C	H_2SO_4, 200 °C/1h	161	0.209	0.034	56
39	1:7	240 °C	H_2SO_4, 240 °C/1h	268	0.147	0.040	70
40	1:7	240 °C	H_2SO_4, 240 °C/6h	260	0.170	0.044	66

Table 3.12: AST results of 1:7 samples leached in H_2SO_4 and heat-treated at different temperatures for varying time lengths.

No.	Post-Treatment	Initial ECSA	% Loss	% Loss	% Loss
		$[cm^2\,mg^{-1}]$	1^{st} AST cycle	2^{nd} AST cycle	3^{rd} AST cycle
34	H_2SO_4, 220 °C ramp/1h	265	26%	32%	36%
35	H_2SO_4, 240 °C ramp/1h	260	17%	26%	29%
36	H_2SO_4, 260 °C ramp/1h	215	16%	25%	30%
39	H_2SO_4, 240 °C/1h	268	6%	11%	18%
40	H_2SO_4, 240 °C/6h	260	10%	22%	25%

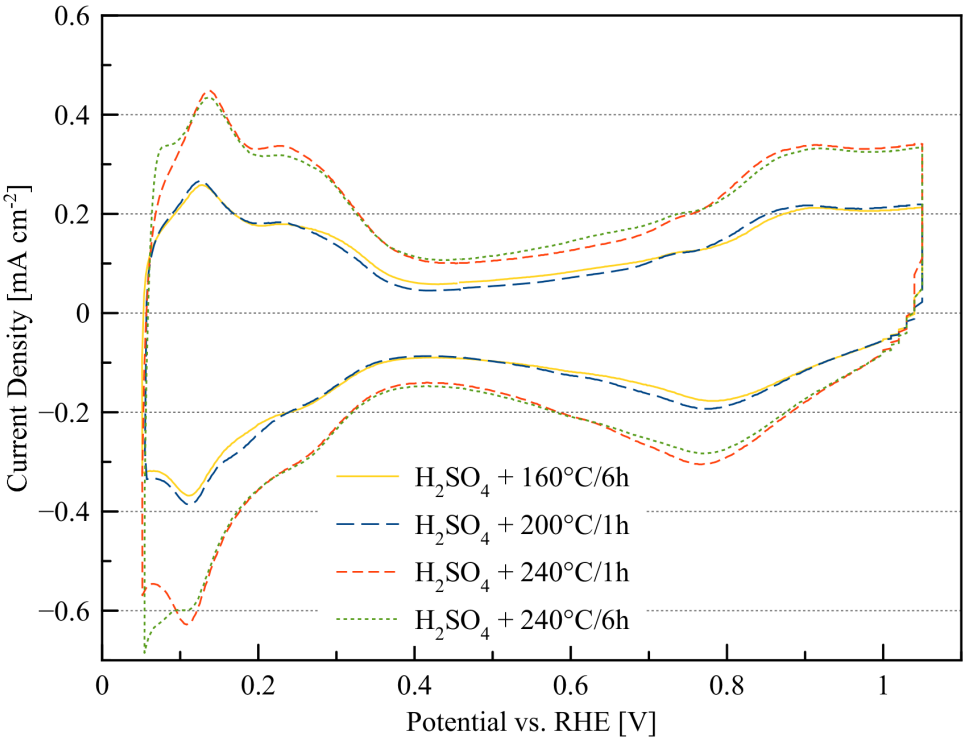

Figure 3.26: CV curves in N_2 of 1:7 samples leached in H_2SO_4 and heat-treated at different temperatures for varying time lengths.

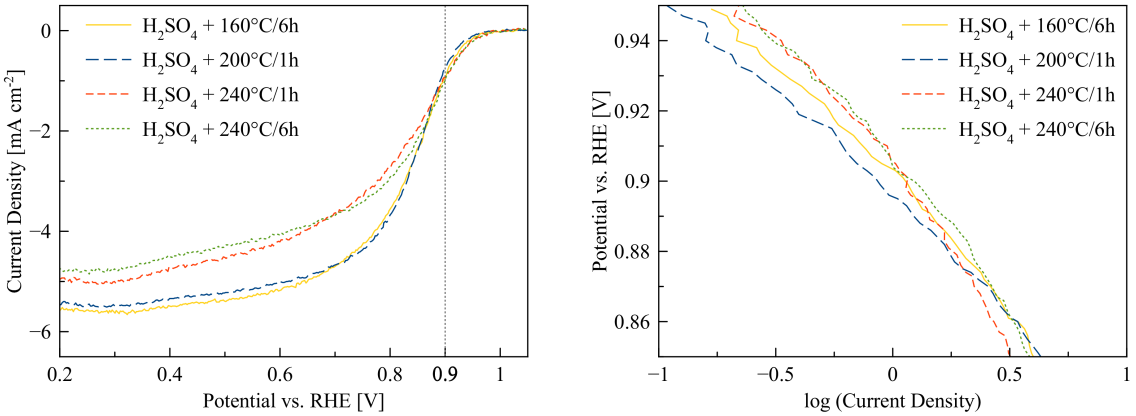

(a) ORR curves in O_2

(b) Tafel plot

Figure 3.27: ORR curves in O_2 and the corresponding Tafel plots of 1:7 samples leached in H_2SO_4 and heat-treated at different temperatures for varying time lengths.

3.8 Heat-Treatment + Leaching

In the previous chapter post-treatment with a leaching step followed by a heat-treatment step was studied. In this series, samples were prepared with those two post-treatment steps the other way round. Again Pt:Fe 1:7 samples were reduced at 240 °C. Afterwards they were washed and dried overnight. The samples were then heat-treated with different temperature programs before they were finally leached in H_2SO_4.

In this set all samples exhibited an ECSA $> 200\,cm^2\,mg^{-1}{}_{Pt}$ and a very good current density at 0.9 V causing very high ORR activities (see Table 3.13). Samples no. 41-43 exhibited even MAs $> 0.05\,A\,mg^{-1}{}_{Pt}$. However, when compared to the leached+heat-treated catalysts, these samples show a less clear step in the ORR curve (Fig. 3.29). This could be due to acid impurities, because leaching in H_2SO_4 was the last step of the synthesis procedure and there was no final temperature-induced cleaning of the surface before the measurements.

The Tafel slope values differed somewhat when comparing these samples, again indicating that temperature program used for heat-treatment seems to have an effect on the surface morphology. However, as leaching is the final synthesis step, the leaching of Fe atoms and the formation of a Pt-skeleton surface should primarily determine the catalysts properties.

The results of the AST experiments shown in Table 3.14 give no clear trend on the catalysts stability. The ECSA loss after the third cycle was in the same range as for the previous samples with around 30%. However, sample no. 42, heat-treated at 240 °C, exhibited an ECSA loss of only 22%.

Overall these catalysts show good catalytic properties and acceptable stabilities, even though not all causes of the occurring effects and modifications seem to be clear. Because leaching is the finial step, it is assumed that the surface modifications by the acid define the properties of the catalysts the most. With this post-treatment order the heat-treatment process has less influence on the catalyst, yet the heat-treatment step seems to offer more opportunities for optimization than the leaching step. Although this synthesis way (heat-treatment + leaching) must not be neglected, using leaching + heat-treatment still seems to be the more promising way for further improvement of the catalyst's properties.

Table 3.13: Measured catalytic properties of 1:7 samples first heat-treated with different temperature programs and then leached in H_2SO_4.

No.	Ratio	Reduction	Post-Treatment	ECSA [$cm^2\,mg^{-1}$]	SCD [$mA\,cm^{-2}$]	MA [$A\,mg^{-1}$]	Tafel Slope [$mV\,dec^{-1}$]
41	1:7	240 °C	220 °C ramp/1h, H_2SO_4	263	0.213	0.056	62
42	1:7	240 °C	240 °C ramp/1h, H_2SO_4	289	0.199	0.058	71
43	1:7	240 °C	240 °C/1h, H_2SO_4	201	0.268	0.054	66
44	1:7	240 °C	260 °C ramp/1h, H_2SO_4	286	0.114	0.032	64

Table 3.14: AST results of 1:7 samples first heat-treated with different temperature programs and then leached in H_2SO_4.

No.	Post-Treatment	Initial ECSA [$cm^2\,mg^{-1}$]	% Loss 1^{st} AST cycle	% Loss 2^{nd} AST cycle	% Loss 3^{rd} AST cycle
41	220 °C ramp/1h, H_2SO_4	263	23%	31%	32%
42	240 °C ramp/1h, H_2SO_4	289	15%	19%	22%
43[a]	240 °C /1h, H_2SO_4	201	–	29%	35%
44	260 °C ramp/1h, H_2SO_4	286	16%	23%	25%

[a] degraded in O_2-saturated electrolyte (higher degradation rates expected)

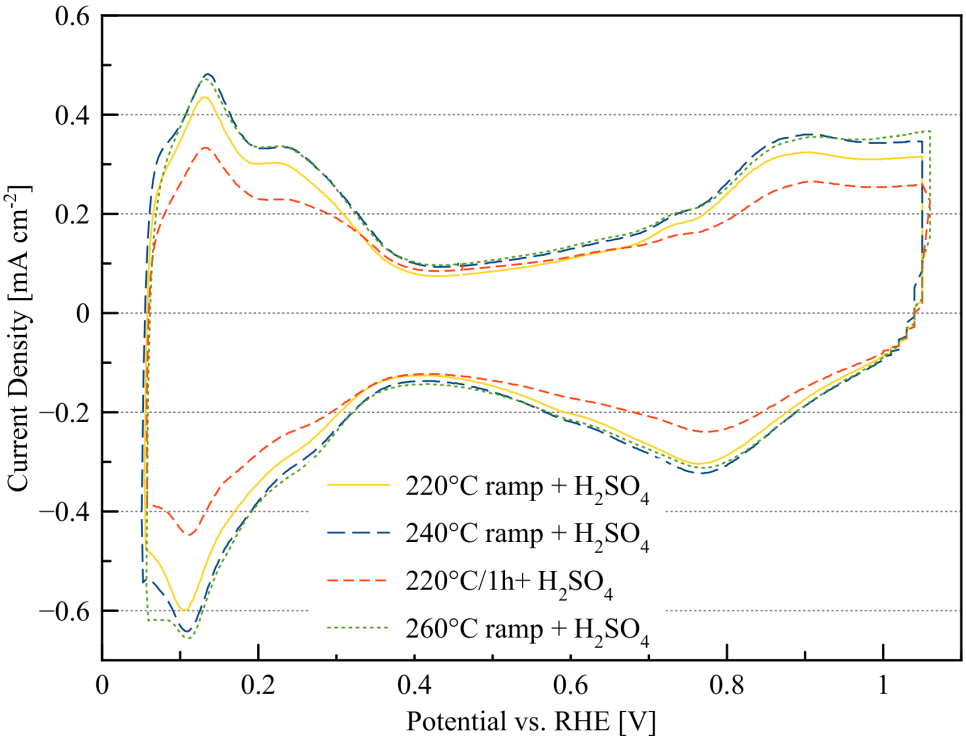

Figure 3.28: CV curves in N_2 of 1:7 samples first heat-treated with different temperature programs and then leached in H_2SO_4.

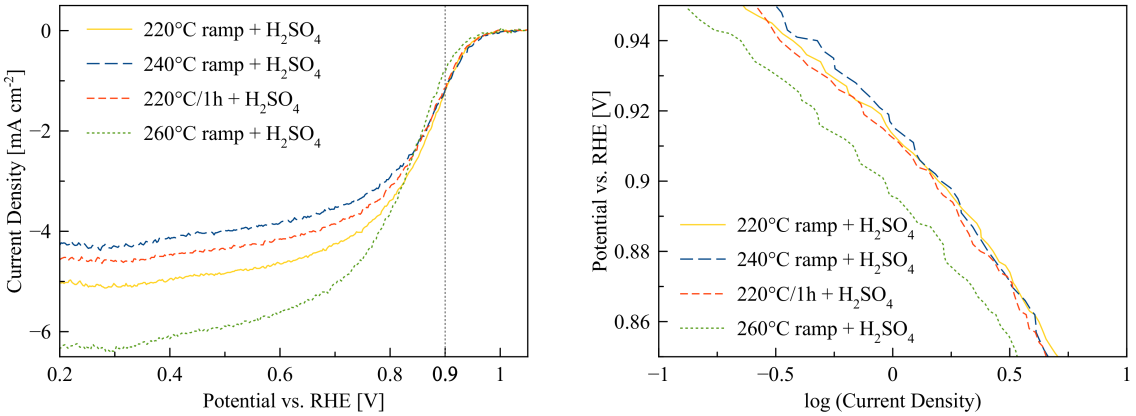

(a) ORR curves in O_2

(b) Tafel plot

Figure 3.29: ORR curves in O_2 and the corresponding Tafel plots of 1:7 samples first heat-treated with different temperature programs and then leached in H_2SO_4.

3.9 Gas Diffusion Electrode Type II

During the studies on the PtFe/C catalysts, the industrial partner elcomax GmbH München developed an altered gas diffusion electrode sheet. The new GDE, here depicted as Type II, had a much thinner carbon layer and the sheet consisted of turbostratic carbon instead of crystalline, resulting in a higher surface area. In this experimental series it was looked into the effects the new GDE sheets had on our so far optimized PtFe/C catalyst system and if the optimized synthesis parameters could be adapted to obtain about the same activities.

In the production process a difference in the impregnation behavior could be observed. Because the new Type II GDEs were much thinner, the impregnation solution did not wet the sheet as well. After some time a little soaking through of the solution through the carbon supporting layer could be observed. This indicates that the amount of solution pipetted onto the GDE (so far 250 μL) needs perhaps to be reduced.

Again the sample leached in H_2SO_4 and heat-treated at 240 °C (no. 47) showed the best catalytic performance with an ECSA of $> 300\,cm^2\,mg^{-1}{}_{Pt}$ and a well-defined ORR step. Similar to the leaching + heat-treatment samples in sec. 3.7, the ECSAs and MAs of samples heat-treated above and below 240 °C were not as good. The only leached sample however exhibited good ORR properties, having the second highest MA of these samples. The shape of all ORR curves is a little flat. Probably this could have been caused by remaining impurities on the GDE. As the carbon of new Type II GDE has a higher surface area than the old one (Type I), it is harder to completely remove all surface contaminations.

The catalytic properties of the Type II catalysts are comparable to the leached + heat-treated samples with the old GDE Type I indicating no big change in the whole catalyst system. The biggest difference between the catalysts with GDE Type I and II is their stability. As the results from AST experiments show (see Table 3.16) is the ECSA loss after the third cycle with around 35% a little bit higher than of the old samples. This could be because of the aforementioned higher surface area of the carbon, which could be more prone to high potential cycling than the Type I carbon. Because not only the PtFe nanoparticles dissolute but also the carbon support is prone to degradation (thereby influencing the nanoparticles), this could be the cause of the higher overall ECSA loss.

Still further testing of the new materials needs to done. However, the results suggest that the catalyst synthesis process is applicable without significant modifications.

Table 3.15: Measured catalytic properties of 1:7 samples synthesized on GDE Type II and post-treated differently.

No.	Ratio	Reduction	Post-Treatment	ECSA [$cm^2\,mg^{-1}$]	SCD [$mA\,cm^{-2}$]	MA [$A\,mg^{-1}$]	Tafel Slope [$mV\,dec^{-1}$]
45	1:7	240 °C	H_2SO_4	251	0.138	0.035	64
46	1:7	240 °C	H_2SO_4, 220 °C ramp/1h	207	0.093	0.019	66
47	1:7	240 °C	H_2SO_4, 240 °C ramp/1h	332	0.148	0.049	68
48	1:7	240 °C	H_2SO_4, 260 °C ramp/1h	271	0.106	0.029	62

Table 3.16: AST results of 1:7 samples synthesized on GDE Type II and post-treated differently.

No.	Post-Treatment	Initial ECSA [$cm^2\,mg^{-1}$]	% Loss 1^{st} AST cycle	% Loss 2^{nd} AST cycle	% Loss 3^{rd} AST cycle
45	H_2SO_4	251	25%	32%	37%
46	H_2SO_4, 220 °C ramp/1h	207	20%	27%	32%
47	H_2SO_4, 240 °C ramp/1h	332	18%	27%	35%
48	H_2SO_4, 260 °C ramp/1h	271	16%	25%	27%

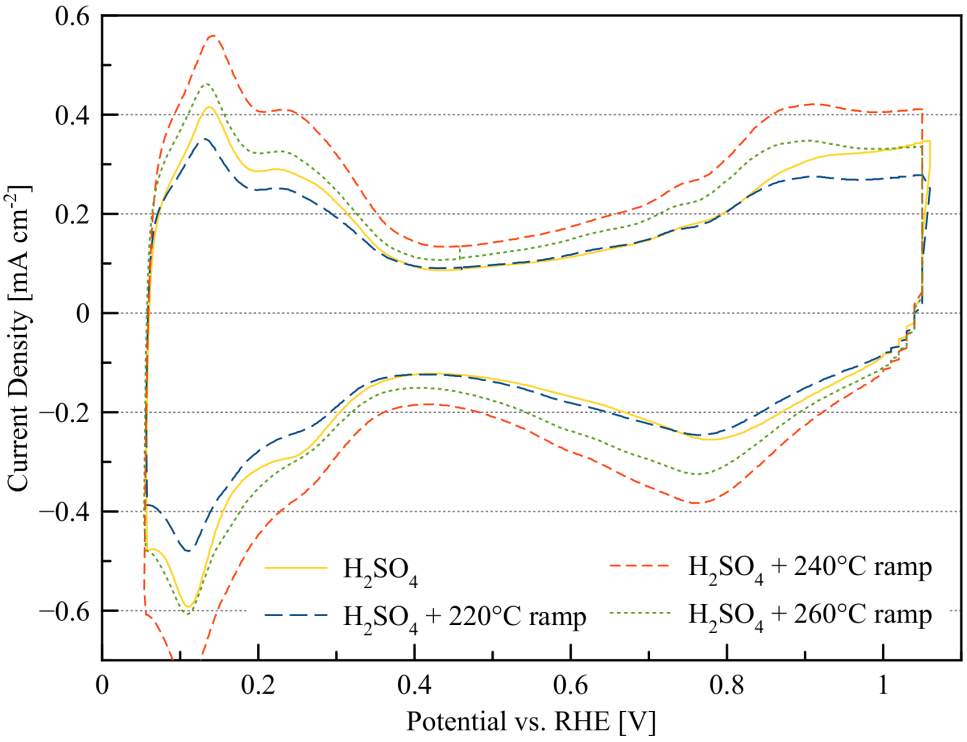

Figure 3.30: CV curves in N_2 of 1:7 samples synthesized on GDE Type II and post-treated differently.

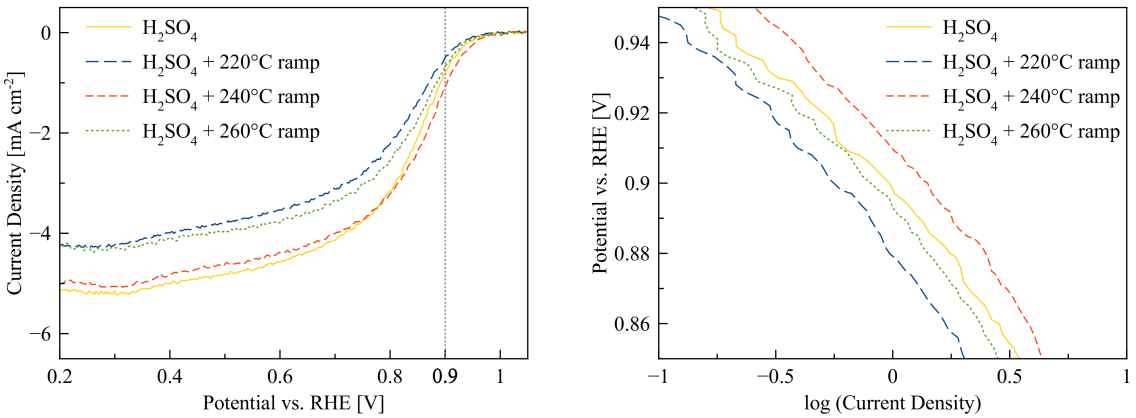

(a) ORR curves in O_2

(b) Tafel plot

Figure 3.31: ORR curves in O_2 and the corresponding Tafel plots of 1:7 samples synthesized on GDE Type II and post-treated differently.

3.10 Conclusions on the Optimization of PtFe/C catalysts

Concluding all optimization experiments, catalysts with a Pt loading of $1.0\,mg\,cm^{-2}$ and a Pt:Fe ratio of 1:7, which were reduced for 10 min at 240 °C, showed the most promising catalytic activity. The activity was enhanced by leaching of the catalyst in H_2SO_4 for 30 min and heat-treatment at 240 °C (ramped with $5\,°C\,min^{-1}$, held for 1 h).

3.10.1 Comparison to Pt/C Standard

Shown in Fig. 3.32 and 3.33, two catalysts synthesized with this synthesis procedure (no. 35 on Type I GDE and no. 47 on Type II GDE) are compared to a commercially available Pt/C catalyst from elcomax GmbH München, which was synthesized with the same impregnation method, but without the post-treatment. This commercial Pt/C catalyst has a higher Pt loading than the newly synthesized PtFe/C with only a Pt loading of $1.0\,mg\,cm^{-2}$. The dispersion solution of the Pt/C catalyst was adapted in order to make the CV and ORR curves comparable.

The CV curves of the Pt/C standard and the PtFe/C Type I sample exhibit nearly the same area of Pt−H desorption peak. Only PtFe/C Type II has a significantly bigger ECSA. Both PtFe/C catalysts have a higher current in the double-layer region. The shape of the Pt−OH and Pt−O formation region is nearly the same for all three catalysts, indicating that Pt atoms represent the main active sites for the ORR [50]. However, the peak is slightly shifted to a more positive potential. Stamenkovic et al. [23] relate this later onset of OH* formation to a lower OH* coverage, which is the desired effect in order to enhance ORR activity.

Interestingly, all three ORR curves exhibit nearly the same shape and Tafel slope. However, in the Tafel plot it can be seen that the curves of PtFe/C catalysts are above the Pt/C standard curve. This indicates slightly better catalytic behavior, although the calculated SCD and MA values are nearly the same.

Although the catalytic activity of PtFe/C catalysts is nearly the same as measured for the Pt/C, the stability is significantly higher. As can be seen in Table 3.18, the ECSA loss after the third AST cycle of the PtFe/C catalysts was about 30-35% compared to the 49% for the Pt/C catalyst, respectively. This indicates the suitability of the newly developed catalysts for fuel cell application, as the catalyst's stability is one of the main issues regarding the long-time stability of HT-PEMFCs. In order to visualize this improvement in catalyst's stability, the corresponding AST CV curves are compared in Fig. 3.34. Especially the big ECSA loss of the Pt/C catalyst after the first AST cycle is conspicuous compared to the PtFe/C catalyst.

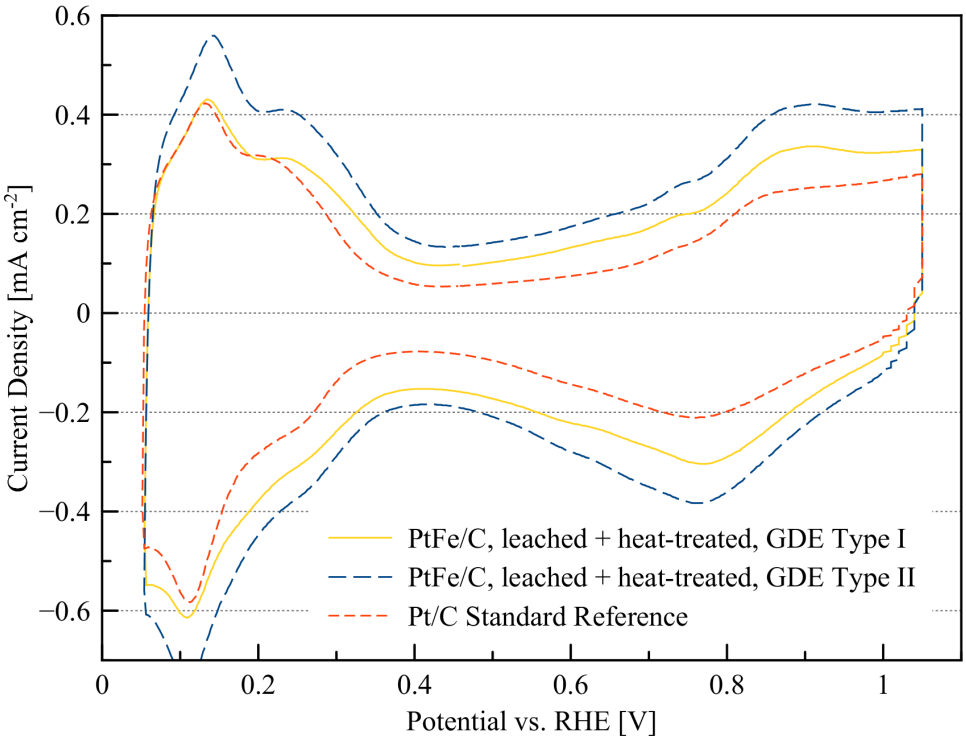

Figure 3.32: CV curves in N_2 of optimized PtFe/C catalysts compared to a similar synthesized Pt/C standard.

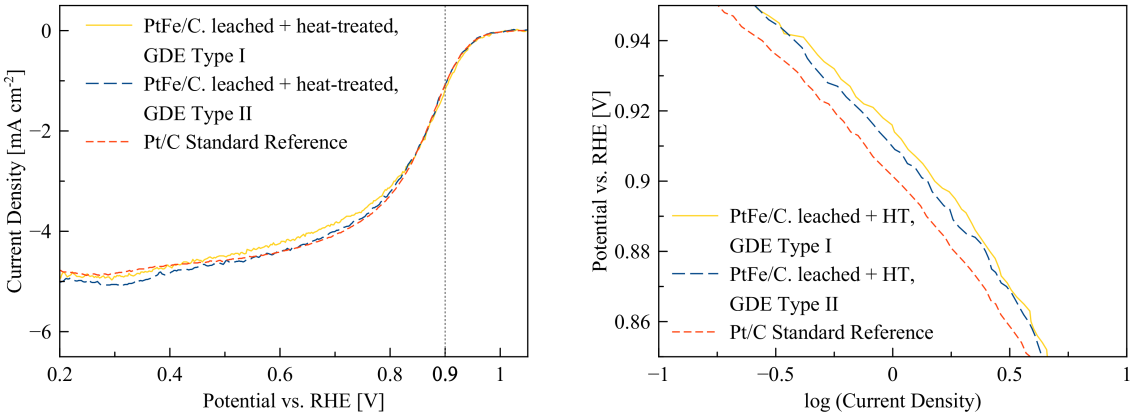

(a) ORR curves in O_2

(b) Tafel plot

Figure 3.33: ORR curves in O_2 and the corresponding Tafel plots of optimized PtFe/C catalysts compared to a similar synthesized Pt/C standard.

Table 3.17: Measured catalytic properties of optimized PtFe/C catalysts compared to a similar synthesized Pt/C standard.

No.	Ratio	Post-Treatment	ECSA [$cm^2\,mg^{-1}$]	SCD [$mA\,cm^{-2}$]	MA [$A\,mg^{-1}$]	Tafel Slope [$mV\,dec^{-1}$]
Standard	only Pt	-	260	0.188	0.049	67
35	1:7	H_2SO_4, 240 °C ramp/1h	260	0.208	0.054	68
47	1:7	H_2SO_4, 240 °C ramp/1h	332	0.148	0.049	68

Table 3.18: AST results of optimized PtFe/C catalysts compared to a similar synthesized Pt/C standard.

No.	Post-Treatment	Intial ECSA [$cm^2\,mg^{-1}$]	% Loss 1^{st} AST cycle	% Loss 2^{nd} AST cycle	% Loss 3^{rd} AST cycle
Standard	-	260	29%	42%	49%
35	H_2SO_4, 240 °C ramp/1h	260	17%	26%	29%
47	H_2SO_4, 240 °C ramp/1h	332	18%	27%	35%

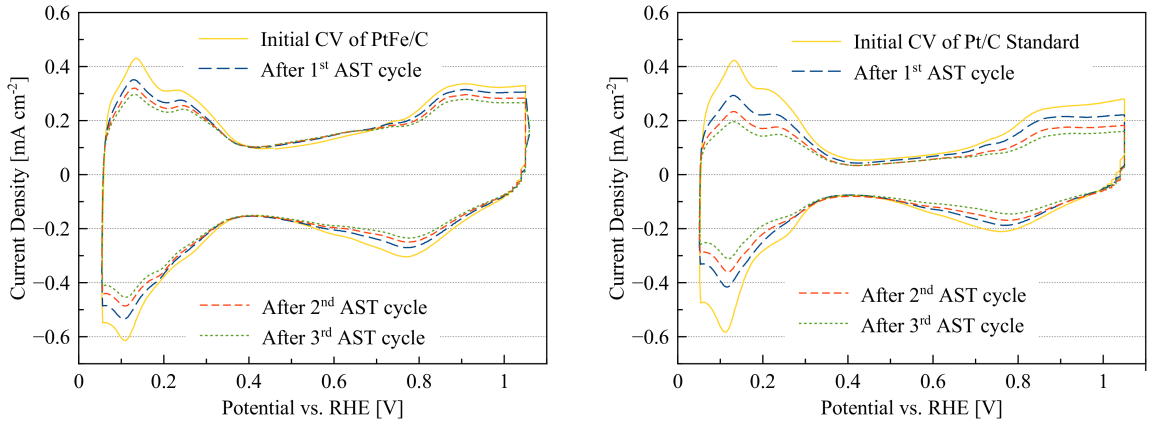

(a) AST of PtFe/C catalyst

(b) AST of Pt/C standard

Figure 3.34: Comparison of the AST cycles of optimized PtFe/C catalysts compared to a similar synthesized Pt/C standard.

3.10.2 Comparison to $NaBH_4$ Batch Synthesized PtFe/C Catalyst

The newly developed PtFe/C catalysts exhibited a good catalytic performance compared to the similar manufactured Pt/C catalyst. Therefore, the next step was to compare them to other PtFe/C catalysts, which were synthesized via a more classical batch synthesis procedure. The aim was to evaluate if the simple impregnation procedure yields catalysts with comparable activities and stabilities. For this, the PtCo/C synthesis procedure by Spanos et al. [38] was chosen due to its promising results and its simple adaptability toward PtFe/C catalysts. In short, in this synthesis procedure nanoparticles were synthesized via direct reduction of the respective Pt and Fe precursor salts (dissolved in ethylene glycol) onto the carbon support with $NaBH_4$ working as the reducing agent. Thereby, the precursors were added step-wise in order to achieve a slow growth rate and thus a small size of the nanoparticles. This batch reaction was performed at room-temperature under constant sonication in an ultrasonic bath and under N_2-flow. In order to make the results comparable to the PtFe/C catalysts on the GDE sheets, the Pt:Fe molar ratio and the Pt:C mass ratio were adapted to the same ratios. Furthermore, the batch synthesized catalyst was leached in H_2SO_4 and heat-treated at 240 °C (ramped with 5 °C min^{-1}, held for 1 h). The exact synthesis procedure including all weighed masses is described in the experimental section 5.2.2 on page 80.

As pure carbon was used as nanoparticle support, the RDE application technique by Garsany et al. [42] using a turned over and rotated RDE rotator (described in sec. 5.3) was applied. Because of the addition of water to the dispersion solution, a defined droplet on the rotated RDE glassy carbon tip could be achieved. The applied amount of Pt on the RDE was different for the three synthesized catalysts (no post-treatment, leached and leached + heat-treated). Therefore, the mass specific current (in mA mg^{-1}) instead of the area normalized current density is shown in the CV, ORR and Tafel plots, allowing it to compare the trends and the activity parameters. In order to calculate the Pt loading on the RDE, the amount of Fe had to be taken into account. For the untreated sample, both Pt and Fe are deposited on the carbon. However, after leaching it was assumed that no Fe remained on the carbon, as the results of Spanos et al. [38] suggested, who measured an almost complete loss of the transition metal after leaching. Thus, a higher Pt weight percentage on the carbon had to be considered in the calculations. This may lead to bigger variations in the results compared to the PtFe/C catalysts synthesized by the impregnation technique, where a defined area of the GDE sheet with a defined amount of Pt was suspended.

As can be seen in Fig. 3.35, the post-treatment had a big impact on the ECSA, which is in accordance with the effects observed for the impregnated PtFe/C catalysts (though with them the effect was even more pronounced). Leaching in H_2SO_4 increased the ECSA by nearly a

third, which is probably due to the dissolution of excess Fe from the PtFe nanoparticles, leaving behind a bigger Pt surface [38]. Further heat-treatment led to another small increase of the ECSA, which can probably assigned to a more thorough removal of the utilized solvent ethylene glycol (boiling point 196-198 °C). The shape of all three CV curves is nearly identical, with a similar-shaped Pt−H desorption peak and a similar onset potential of Pt−OH/Pt−O formation. The slightly broader double-layer region could be again due to surface oxidation of the carbon support (see sec. 3.5.3).

The ORR curves are similarly shaped and SCD and MA values are also in the same range compared to the results of the impregnated PtFe/C catalysts. Interestingly, the MA of the leached + heat-treated sample was lower than for the only leached sample. Although the ECSA of the leached + heat-treated sample was slightly higher, all in all, the heat-treatment did not improve the catalyst's performance. Noteworthy is the higher Tafel slope of the two post-treated samples, indicating a change in the catalytic pathway through surface modifications caused by H_2SO_4 leaching.

All in all, the ECSAs and MAs measured for these batch synthesized samples are in the same range as for the impregnated PtFe/C catalyst. This means, that the less time-consuming, inexpensive and in principal continuous impregnation approach studied in this work, yields PtFe/C catalysts with comparable catalytic properties.

As can be seen in Table 3.20 stability measurements performed via AST cycles, revealed a much higher degradation rate and a more tremendous ECSA loss compared to the impregnated PtFe/C catalysts. Surprisingly, the post-treatment seemed to have a negative influence on the catalyst's stability, leading to an ECSA loss of over 40% after the third cycle, which is about the same as was measured for the only Pt/C catalyst (see sec. 3.10.1).

Although there are even more complex and laborious synthesis procedures for PtFe/C catalysts as the chosen one by Spanos et al. [38], the results from these experiments show, that the inexpensive and straightforward impregnation process studied and optimized in this work yields catalysts with comparable catalytic activity and significantly higher stability, as is indicated by the AST experiment results.

Table 3.19: Measured catalytic properties of a batch synthesized PtFe/C catalyst reduced with $NaBH_4$ after different post-treatment steps.

No.	Ratio	Reduction	Post-Treatment	ECSA [$cm^2\,mg^{-1}$]	SCD [$mA\,cm^{-2}$]	MA [$A\,mg^{-1}$]	Tafel Slope [$mV\,dec^{-1}$]
49 a	1:7	$NaBH_4$	-	236	0.118	0.028	58
49 b	1:7	$NaBH_4$	H_2SO_4	309	0.128	0.040	69
49 c	1:7	$NaBH_4$	H_2SO_4, 240 °C ramp/1h	329	0.098	0.032	71

Table 3.20: AST results of a batch synthesized PtFe/C catalyst reduced with $NaBH_4$ after different post-treatment steps.

No.	Post-Treatment	Intial ECSA [$cm^2\,mg^{-1}$]	% Loss 1^{st} AST cycle	% Loss 2^{nd} AST cycle	% Loss 3^{rd} AST cycle
49 a	-	236	23%	33%	38%
49 b	H_2SO_4	309	30%	38%	44%
49 c	H_2SO_4, 240 °C ramp/1h	329	34%	37%	45%

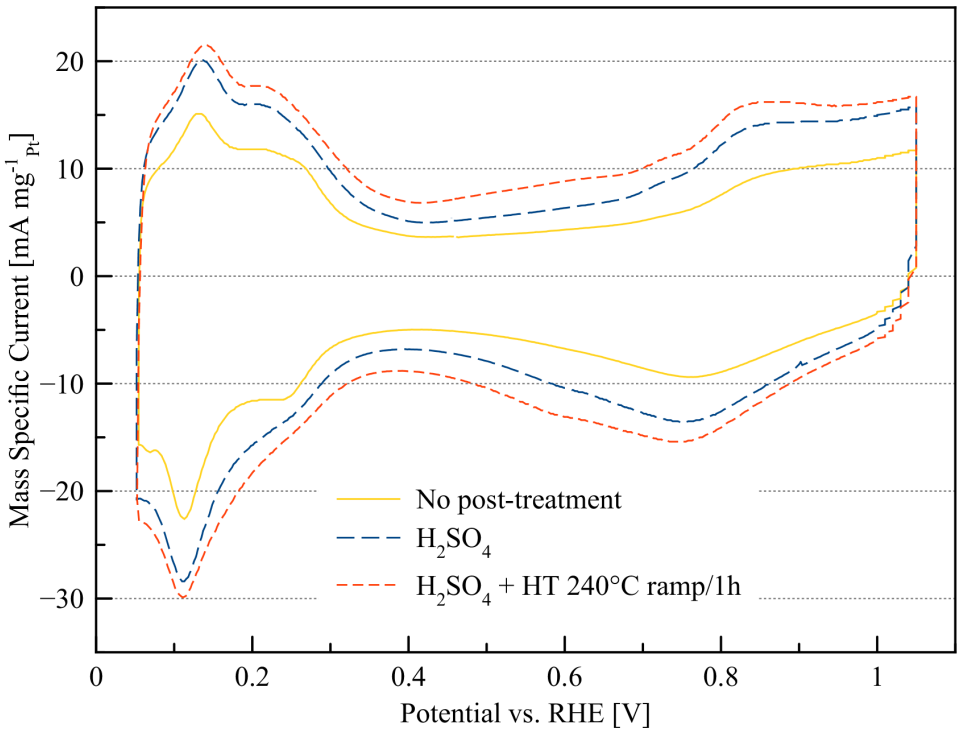

Figure 3.35: CV curves in N_2 (with mass normalized current) of a batch synthesized PtFe/C catalyst reduced with $NaBH_4$ after different post-treatment steps.

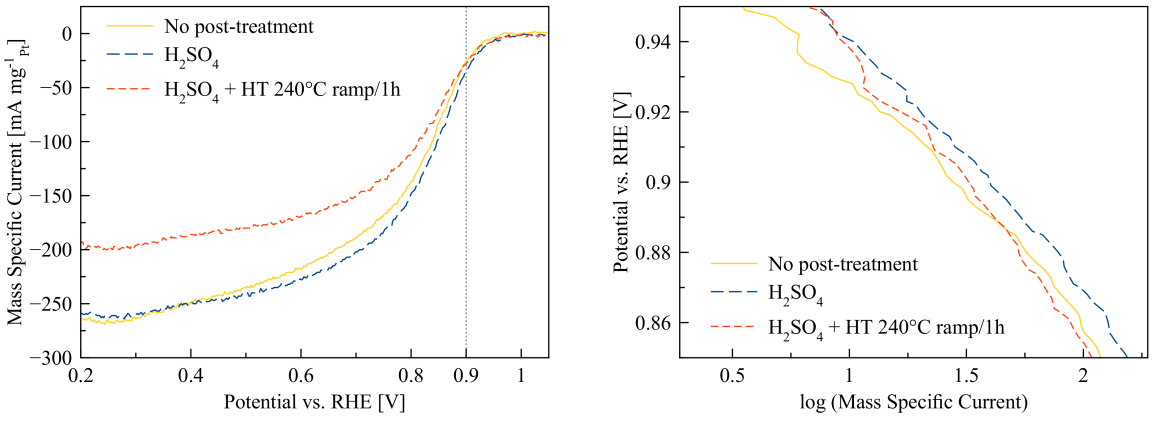

(a) ORR curves in O_2

(b) Tafel plot

Figure 3.36: ORR curves in O_2 and the corresponding Tafel plots (with mass normalized current) of a batch synthesized PtFe/C catalyst reduced with $NaBH_4$ after different post-treatment steps.

3.11 HT-PEM Fuel Cell Testing

Because the results from the ex-situ cyclic voltammetry experiments were very promising, in-situ testing in a fuel cell was performed. For this, a bigger GDE sheet (10 x 10 cm) had to be prepared (using GDE Type I). Due to the bigger size of the catalyst sheet crumbling of the carbon layer was expected to occur. Therefore, the usual impregnation solution composition with the volumetric ratios of 1:1:1.4 for 2-propanol/ultra-pure water/ethylene glycol, was changed to a less viscous solution composition. Reducing the amount of the viscous ethylene glycol to a volumetric ratio of 0.7 (equals 7 electronic equivalents related to Pt and Fe), resulted in a better wetting of the GDE so that in the end the GDE sheets were not damaged by the impregnation and reduction procedure. The post-treatment included again leaching of the sheet in H_2SO_4 and heat-treatment at 240 °C (ramped with 5 °C min^{-1}, held for 1 h).

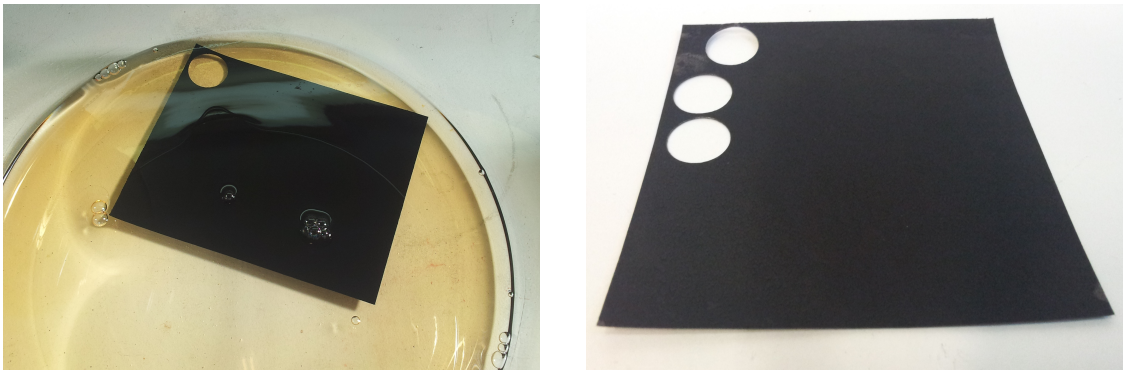

(a) Leaching in H_2SO_4 (b) Final GDE

Figure 3.37: 10 x 10 cm GDE sheet during the leaching step and the final sheet after leaching + heat-treatment.

In order to monitor the synthesis process, disks for CV measurements were stamped out of the big GDE sheet after each step. The results of the ex-situ measurements are shown in Fig. 3.38 and 3.39 and Table 3.21.

In accordance with previous results on impregnated PtFe/C catalysts, the ECSA was significantly raised after the H_2SO_4 leaching. The ECSA was decreased again after the heat-treatment. Probably this was caused by a smoothing of the leached and thus corrugated Pt surface and by a rearrangement of the nanoparticle surfaces. Interestingly, this time the heat-treatment did not have an activity enhancing effect on the catalyst. Although the ORR curve exhibited a well-defined step, it was significantly shifted to lower potentials compared to the leached sample, which results in a very low SCD and MA value. This indicates that the heat-treatment step still needs to be further investigated in order to raise the reproducibility. However, the values

Table 3.21: Measured catalytic properties of samples taken after each synthesis step from one bigger GDE layer manufactured for HT-PEMFC testing.

No.	Ratio	Reduction	Post-Treatment	ECSA	SCD	MA	Tafel Slope
				$[cm^2\,mg^{-1}]$	$[mA\,cm^{-2}]$	$[A\,mg^{-1}]$	$[mV\,dec^{-1}]$
50 a	1:7	240 °C	-	167	0.196	0.033	68
50 b	1:7	240 °C	H_2SO_4	308	0.189	0.058	64
50 c	1:7	240 °C	H_2SO_4, 240 °C ramp/1h	254	0.114	0.029	62

of the Tafel slope were all in the same range, slightly above the ideal range of $60\,mV\,dec^{-1}$, indicating similar catalytic reaction pathways in all three manufacturing steps.

Table 3.22: AST results of samples taken after each synthesis step from one bigger GDE layer manufactured for HT-PEMFC testing.

No.	Post-Treatment	Intial ECSA	% Loss	% Loss	% Loss
		$[cm^2\,mg^{-1}]$	1^{st} AST cycle	2^{nd} AST cycle	3^{rd} AST cycle
50 a	-	167	16%	23%	27%
50 b	H_2SO_4	308	25%	39%	46%
50 c	H_2SO_4, 240 °C ramp/1h	254	23%	30%	33%

The AST experiments showed a surprisingly high degradation after the H_2SO_4 leaching. Heat-treatment lowered the degradation rate again to slightly above 30% after the third AST cycle. This is in about the range of the previously studied PtFe/C catalysts, and significantly better than the Pt/C standard and the batch synthesized PtFe/C catalysts. Interestingly, there was already a high degradation after the first AST cycle followed by a lower degradation rate when cycled further as is shown in Fig. 3.40. This indicates that the first high potential cycles have the strongest modifying effect on the catalyst nanoparticles and the carbon support.

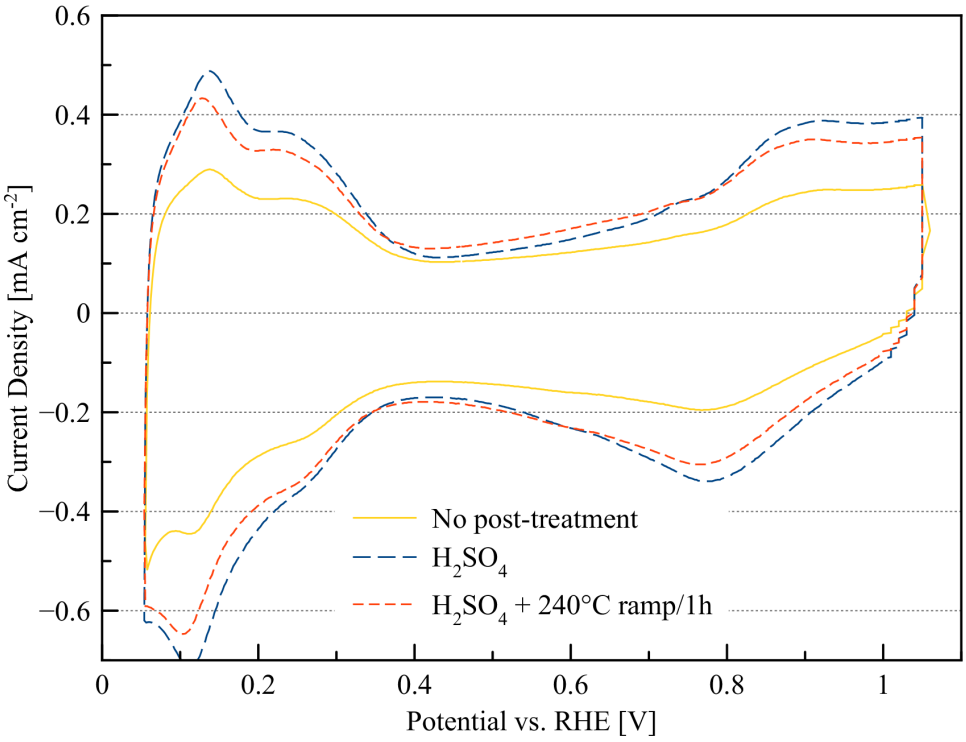

Figure 3.38: CV curves of samples taken after each synthesis step from one bigger GDE layer manufactured for HT-PEMFC testing.

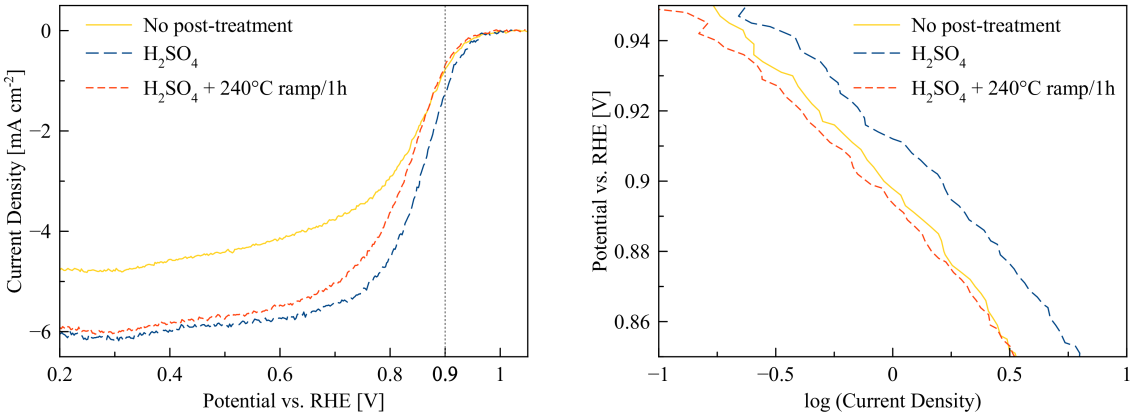

(a) ORR curves in O_2

(b) Tafel plot

Figure 3.39: ORR curves in O_2 and the corresponding Tafel plots of samples taken after each synthesis step from one bigger GDE layer manufactured for HT-PEMFC testing.

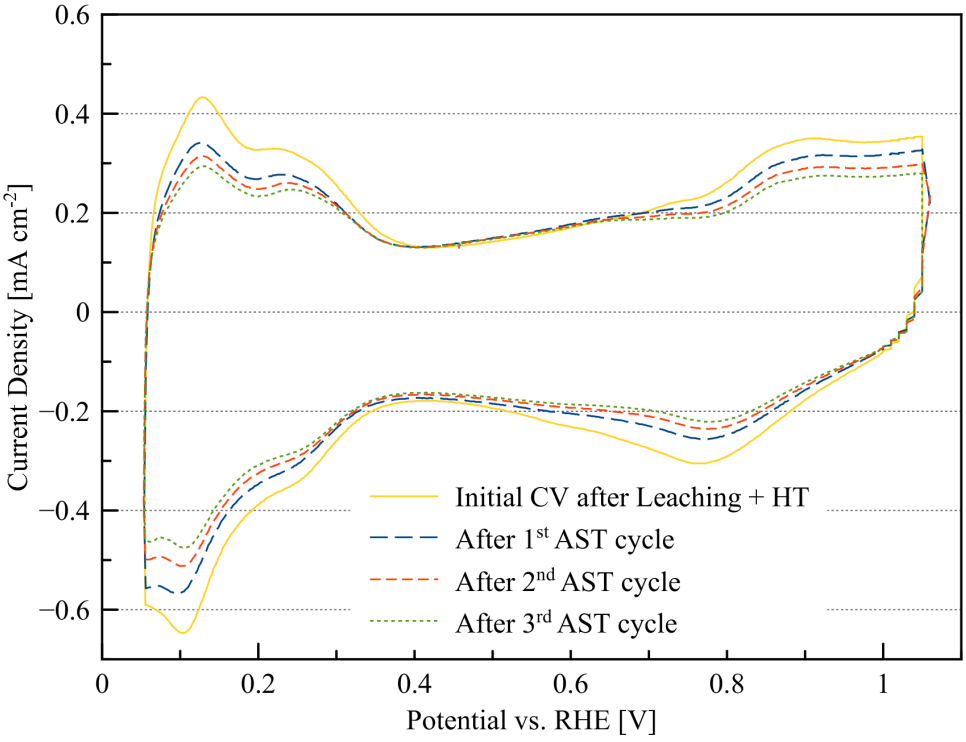

Figure 3.40: CV curves before and after the AST and of sample no. 50 c (leached in H_2SO_4 and heat-treated at 240 °C with ramp).

The cathode catalyst layer was then tested in a single cell HT-PEMFC set-up at 160 °C working temperature using either H_2 or synthetic reformate as anode gases. The cathode side was supplied with air. The anode catalyst was pure Pt and a polybenzimidazole (PBI) membrane was utilized. The proton conductivity was assured by doping the catalyst layer with phosphoric acid. The acid together with the elevated operating temperature of 160 °C induce a high stress on the catalyst material, which poses the main issue regarding long-term HT-PEM fuel cell operation.

The recorded U/I polarization curves are shown in Fig. 3.41. At zero current a OCV of 860 mV was measured, which is a drop of 370 mV from the theoretical OCV at 1.23 V. Raising the current, the voltage drops significantly (about 200 mV) due to activation losses. Above 0.05 A cm^{-2} the lowering of the cell voltage is nearly linearly, which can be attributed to the internal ohmic resistances in the cell. In this region the performance of the cell fuelled with synthetic reformate is lower compared to the U/I curve of the H_2 supplied set-up. This results in a significantly lower current and thus power density at the stopping point of the experiment at 350 mV. This indicates that, although the type of fuel does not have a big impact in the low current density

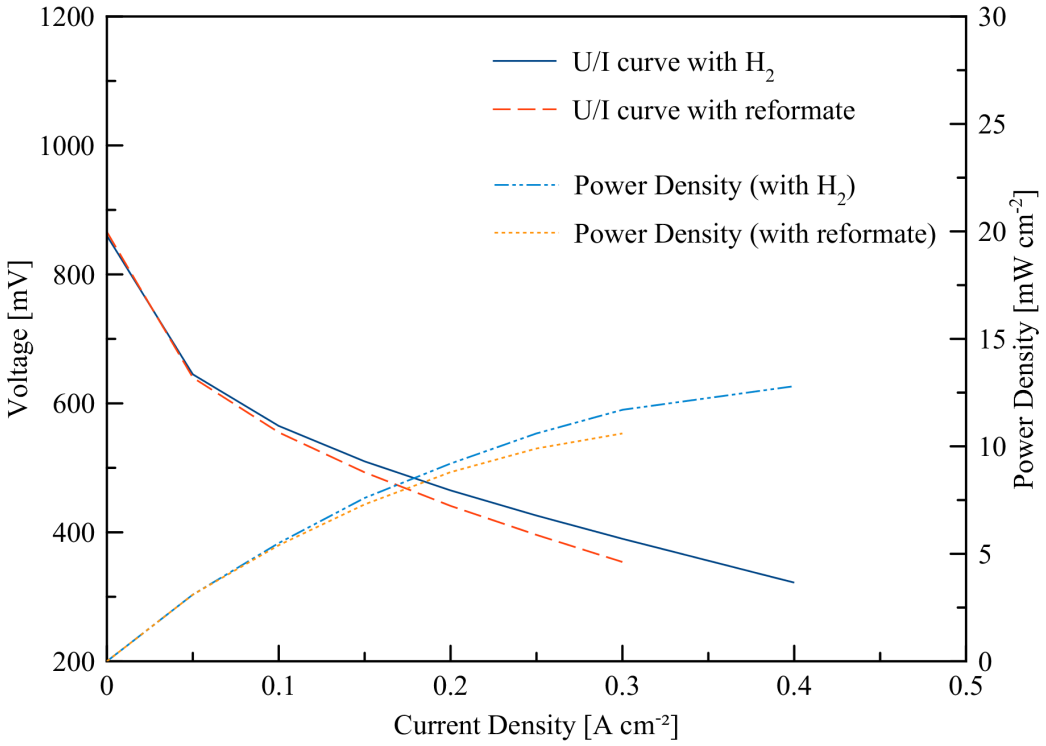

Figure 3.41: Recorded U/I polarization curve and the corresponding power density of a PtFe/C cathode catalyst in a HT-PEMFC single cell test supplied either with H_2 or reformate as anode gas.

region, contaminations by the present CO in the reformate can limit the power output of the fuel cell.

In conclusion, the first testing of the synthesized PtFe/C catalysts in real HT-PEMFC operating conditions showed acceptable and promising results, especially when considering that the Pt loading on the cathode was reduced to $1.0\,\mathrm{mg\,cm^{-2}}$. However, long-term tests and further optimization of the post-treatment steps needs to be done in order to make these catalysts competitive against pure state-of-the-art industrial Pt/C catalysts. Furthermore, it would be interesting to study the performance of PtFe/C catalysts with an even lower Pt loading of $0.8\,\mathrm{mg\,cm^{-2}}$.

4 Summary and Outlook

In this work PtFe/C catalysts for the oxygen reduction reaction on the cathode of high temperature PEM fuel cells were synthesized. The focus was thereby on the development of the process and post-treatment steps and the subsequent optimization of the synthesis parameters in order to manufacture catalysts with good catalytic properties and a high stability. The transferability of the procedure to a simple and up-scalable production process was always taken into account.

Preprepared gas diffusion electrodes, knife-coated with high surface area carbon, were impregnated with a precursor solution containing dissolved Pt and Fe salts in the optimized molar ratio of 1:7. After the vaporization of excess solvent, the respective salts were reduced at 240 °C using ethylene glycol as reducing agent in order to form PtFe nanoparticles on the carbon support. Improvement of the catalytic performance was achieved by introducing post-treatment steps.

Leaching of the PtFe/C catalyst sheets in 10% H_2SO_4 solution led to an increased electrochemical surface area through the dissolution of Fe atoms, leaving behind a so called "Pt-skeleton" surface. The catalytic improvement can thereby be ascribed to leaching induced strain-effects rather than to electronic ligand effects, which are less pronounced because of the low Fe content after the leaching. Besides the positive effect of an increased Pt surface, through this pre-leaching step no metal ions and other contaminations can damage the HT-PEMFC during operation (which would have been leached out anyway due to the very acidic fuel cell environment). With pre-leaching they were already removed.

The second post-treatment step applied was heat-treatment of the catalysts at temperatures between 200-300 °C with or without a heat-ramp. Thereby the nominal composition of the nanoparticles stayed the same, however the surface was rearranged and smoothed, which led to a slightly lower Pt surface area but a higher stability of the catalysts. A third observed effect was the cleaning of the surface from organic remains of the reduction process (e.g. tenside, ethylene glycol and oxidation products) and of the leaching process. This had again a positive effect on the ECSA. Of all the investigated temperature programs, ramped heat-treatment (5 °C min^{-1} starting from 30 °C) up to 240 °C (held for 1 h) under N_2-atmosphere, yielded the best results

regarding the activity and stability, although many tested heat-treatment procedures showed similarly good results.

All in all, the leaching step had an overall bigger influence on the catalyst's properties than the heat-treatment, which should be further studied in order to clarify the influencing parameters. The final goal would be to achieve a higher reliability and reproducibility of the synthesis pathway and to obtain PtFe/C catalysts with an even higher stability in the very acidic operating conditions of HT-PEMFCs. It is important to note that in the ex-situ performed accelerated stress test the synthesized PtFe/C catalysts exhibited already a significantly higher stability than a comparable Pt/C standard and a batch synthesized PtFe/C catalyst. Of course, in-situ long-term HT-PEMFC testing is necessary to confirm this very promising property as long-term stability is one of the major challenges of HT-PEMFC big-scale commercialization.

However, the optimization investigations so far showed that PtFe/C catalysts seem to be a very promising alternative to other Pt alloy catalysts such as PtCo/C, with the advantage of using a much cheaper and abundant non-noble metal. Furthermore, by introducing an up-scalable and in principal continuous production process, future commercialization can be achieved more easily. The aim for each synthesis step was to keep it as simple as possible by using common chemicals, short production times and rather low temperatures. Furthermore, it was attempted to lower the cost of the catalyst by reducing the amount of Pt.

Future projects would need to further investigate the influence of heat-treatment on the PtFe/C catalysts by varying time, temperature and the ambient atmosphere. Also the utilization of the new GDE Type II needs to be further optimized, especially through adjusting the viscosity of the impregnation solution. With this, the synthesis should become more reproducible and reliable so that in the end robust PtFe/C catalysts for HT-PEMFC operation are obtained.

5 Experimental

5.1 Materials and Methods

5.1.1 Chemicals

All chemicals were used as purchased without further purification.

- High surface carbon gas diffusion electrodes provided by elcomax GmbH München
  - Type I: crystalline carbon (thicker layer)
  - Type II: turbostratic carbon (thinner layer, higher surface area)
- $H_2PtCl_6 \cdot 6\,H_2O$ ACS grade $\geq$ 37.5% Pt basis (Sigma-Aldrich)
- $Fe(NO_3)_3 \cdot 9\,H_2O$ ACS grade 99.99% (Sigma-Aldrich) and ACS $\geq$ 98% (Sigma-Aldrich)
- Ethylene Glycole $\geq$ 99.5% (Fluka Analytical)
- 2-propanol ACS grade $\geq$ 99.8% (Sigma-Aldrich)
- Ultrapure 18 MΩ H_2O
- Brij30® $M_n \sim 362$ (Sigma-Aldrich)
- H_2SO_4 ACS grade 95-98% (Sigma-Aldrich)
- HCl p.a. $\geq$ 32% (Fluka Analytics)
- Black carbon VXC 72 (Cabot Corporation)
- 0.1 M $HClO_4$ acid concentrate for 1 L standard solution (Fixanal®, Fluka Analytical)
- Nitrogen (5.0, Messer Group GmbH)
- Oxygen (5.0, Messer Group GmbH))
- Alumina Suspension 0.05 µm (MasterPrep, Bühler)

5.1.2 Instruments

- Bi-potentiostat/galvanostat by Metrohm Autolab B.V. Type PGSTAT302N (Software: NOVA 1.7.8 by Metrohm Autolab B.V.)
- Ring-Disk Electrode System by Princeton Applied Research, Model 636
- Ring disk electrode (glassy carbon area 0.196 cm^2) by Pine Instruments (model AFE5T050GC)
- Hydrogen Reference Electrode by Gaskatel HydroFlex
- Platinized titanium rod counter electrode by Bank Elektronik - Intelligent Controls GmbH
- Muffle Furnace by Elsklo, Type LNT15G/1320 °C/5.5 kW/Dicon
- Ultrasonic Bath Bandelin Sonorex by Bandelin electronic, Type RK31

5.2 Synthesis and Sample Preparation

5.2.1 Sample Preparation on gas diffusion electrode sheets

Gas Diffusion Electrodes

The gas diffusion electrode sheets (Type I and II) were provided by elcomax GmbH München.

Impregnation Solution

For impregnating the GDE sheets a solution containing platinum and iron precursor salts, a reducing agent, solvents and a tenside was prepared.

Due to the hygroscopic nature of $H_2PtCl_6 \cdot 6\,H_2O$, a Pt stock solution was prepared by weighing in $H_2PtCl_6 \cdot 6\,H_2O$ in a glove box and dissolving it with a known quantity of ultra-pure water/2-propanol 1:1. The necessary amount of Fe salt was stoichiometrically related to pure Pt. Ultra-pure water and 2-propanol as solvents and ethylene glycole as the reducing agent were added in the ratios 1:1:1.4 (or 1:1:0.7 in the case of solution no. 8 in order to get a lower viscosity of the solution). The non-ionic tenside Brij30® was added with a concentration of 0.036 mg mL^{-1}. The appropriate amounts of each lead to a Pt concentration of either 15.4 mg mL^{-1} or 19.4 mg mL^{-1}. The 15.4 mg mL^{-1} solutions were prepared for the catalyst sheets with a Pt loading of 0.80 mg cm^{-2} and the 19.4 mg mL^{-1} solution in order to get a Pt loading of 1.00 mg cm^{-2} on the GDE.

The solution was prepared in this order: first $Fe(NO_3)_3 \cdot 9\,H_2O$ was dissolved in water, 2-propanol, ethylene glycol and Brij30®. Then an appropriate amount of the Pt stock solution was added.

Table 5.1: List of utilized impregnation solution compositions.

Solution	**Pt:Fe**	**Pt**	**Fe**	**H_2O**	**IPA**	**EG**	**Brij30**
	molar ratio	[mg mL^{-1}]	[mg mL^{-1}]	vol. ratio	vol. ratio	vol. ratio	[mg mL^{-1}]
1	1:1	15.4	4.4	1	1	1.4	0.036
2	1:3	15.4	13.2	1	1	1.4	0.036
3	1:5	15.4	22.0	1	1	1.4	0.036
4[a]	1:7	15.4	30.9	1	1	1.4	0.036
5	1:10	15.4	44.1	1	1	1.4	0.036
6	3:1	15.4	1.5	1	1	1.4	0.036
7[b]	1:7	19.4	38.8	1	1	1.4	0.036
8[c]	1:7	19.4	38.8	1	1	0.7	0.036

[a] Used for 1:7 samples with 0.8 mg cm^{-2} Pt loading

[b] Used for 1:7 samples with 1.0 mg cm^{-2} Pt loading

[c] Used for 1:7 samples with 1.0 mg cm^{-2} Pt loading; less ethylene glycol

Reduction and Post Treatment Procedures

2.2 · 2.2 cm high surface carbon gas diffusion layer sheets were pre-dried in the drying oven for 30 min at 100 °C and then evenly impregnated with 250 µl of the freshly prepared precursor solution to obtain a Pt concentration of 0.80 mg cm^{-2} or 1.00 mg cm^{-2}, depending on the Pt concentration of the precursor solution. Differently sized GDE sheets were impregnated with the appropriate amount of precursor solution to obtain the same Pt loading. The GDE sheets were then evenly dried in the drying oven for at least 30 min at 100 °C until all solvents were vaporized. Generally, bigger GDE sheets needed a longer drying period up to 2 h. The reduction of the precursor salts was performed in the muffle furnace at varying elevated temperatures (e.g. 240 °C) for 10 min under N_2-flow (100 L h^{-1}).

After the reduction process the samples were treated in five different ways, which are listed as follows:

- *No post-treatment:* The samples were put in water/IPA 1:1 for 30 min to wash off remains of the reduction process and then dried overnight at room temperature.

- *Acid leaching:* The samples were leached by putting them in 10% acid solution (either H_2SO_4 and/or HCl) in water/IPA 1:1 for 30 min, washed in water/IPA 1:1 for 30 min and then dried overnight at room temperature.
- *Heat-treatment:* The samples were washed in water/IPA 1:1 for 30 min and dried overnight. Then they were heat-treated in the muffle oven in N_2 atmosphere with varying temperature programs (listed in Table 5.2).
- *Acid leaching + heat treatment:* Both post-treatment steps were combined. First the samples were leached in 10% acid, washed and dried overnight and then heat treated in the muffle oven.
- *Heat treatment + acid leaching:* Both post-treatment steps were performed the other way around. The samples were washed, dried and heat treated in the muffle oven and then leached in 10% acid, washed again and dried overnight.

Table 5.2: List of the different used temperature programs.

Temperature	Time	Ramp
160 °C	6 h	-
200 °C	1 h	-
200 °C	1 h	5 °C min^{-1}
220 °C	1 h	-
220 °C	1 h	5 °C min^{-1}
240 °C	1 h	-
240 °C	6 h	-
240 °C	1 h	5 °C min^{-1}
260 °C	1 h	-
260 °C	1 h	5 °C min^{-1}

5.2.2 $NaBH_4$ Batch Synthesis Method for PtFe Nanoparticles

This nanoparticle precipitation technique is based on the carbon supported Pt_xCo_{1-x} synthesis by Spanos et al. [38] and modified for carbon supported PtFe nanoparticles. For a better comparability the weighted mass are adapted to obtain a Pt to C mass ratio of 1:23.8, which correlates to a Pt loading of 1.00 mg cm^{-2} on a GDE sheet, and molar ratio of Pt to Fe of 1:7.

414 mg (1.025 mmol, 7 eq.) $Fe(NO_3)_3 \cdot 9\,H_2O$ were dissolved in 15 mL ethylene glycol in a glass vial and sonicated for 15 min under N_2 flow. In a second vial 75,8 mg (0,146 mmol, 1 eq.)

H_2PtCl_6, in form of a prepared stock solution (see sec. 5.2.1) were dissolved in 15 mL ethylene glycol and sonicated as well for 15 min under N_2 flow. 40 mL of a 0.1 M $NaBH_4$ solution in water was prepared in a third vial in order to serve as the reducing agent. In a 250 mL 3-necked round bottom flask with a glass stopper, a septum with a long cannula for degassing and a gas outlet, 120 mg Vulcan X carbon were dissolved in 30 mL ethylene glycol and sonicated for 15 min, while degassing the solution with N_2. 0.2 mL of 33% NH_3 solution in water as added to raise the pH to 10.

For Pt seed formation, 0.6 mL of the Pt solution were added drop-wise to the carbon dispersion under constant sonication and N_2 flow followed by the addition of 2 mL of $NaBH_4$ solution. After a 2 min waiting period, 1 mL Fe solution and 1 mL Pt solution were added drop-wise followed by the addition of another 2 mL of $NaBH_4$ solution. This was done repeatedly under constant sonication and direct degassing of the solution over a time-span of about 45 min until both metal precursor solutions were used up. From time to time the pH value was slightly corrected to pH 10 by adding some droplets of 33% NH_4 solution. The black dispersion was kept in the ultrasonic bath for another 2 hours.

The fine black product was vacuum filtrated (Pore 3) over a circular filter paper, which was pre-treated with carbon to minimize product loss into the paper, and washed twice with ultra-pure water. The product on the filter paper was dried at 100 °C then scratched off and dried again. The final product was a fine black powder with a Pt loading of 13.9 wt%.

100 mg of the product were leached in 4 mL 10% H_2SO_4 solution for 30 min in an ultrasonic bath. Then the leached product was filtrated again over pre-treated filter paper and washed four times to remove all acid remains. The product on the filter paper was dried at 100 °C then carefully scratched off and dried again.

25 mg of the leached PtFe catalyst were heat treated in the muffle furnace. The sample was heated up to 240 °C with 5 °C min^{-1} and kept at that temperature for 45 min. Afterwards the catalyst was removed from the oven and cooled down at room temperature. For evaluating the Pt loading of the final product the complete dissolution of Fe in the co-catalyst through the leaching process had to be assumed. This led to a Pt loading of 22.2 wt% for the leached and the leached + heat-treated samples.

5.3 Characterization Methods

In order to prepare the catalyst pads for CV measurements an ink-like carbon dispersion was prepared. For this a 16 mm diameter disk was stamped out of the pad and suspended for about 15 min in either 2.92 mL or 3.64 mL of IPA (depending on the Pt loading on the GDE sheet)

in an ultrasonic bath until a homogeneous dispersion was obtained. Representative 10 µl of the dispersion were pipetted carefully in two 5 µl portions onto the glassy carbon disk of the RDE (area 0.196 cm^2), resulting in a Pt loading of 28 µg cm^{-2} (geometric surface area) on the working electrode. The excess solvent was dried off slowly at room temperature, resulting in a smooth dispersion on the glassy carbon surface.

For the batch synthesized catalyst a different RDE preparation method was used [42]: 4.6 mg of the batch synthesized catalyst were suspended in 2 mL ultra-pure water/IPA 70:30 in an ultrasonic bath to form a homogeneous dispersion. In order to form an even catalyst film on the GDE the electrode was fixed onto the upside-down rotator and rotated with 700 rpm. A representative 10 µl of the dispersion were pipetted onto the rotating RDE and dried for 20 min at room temperature giving a Pt loading of 16.3 µg cm^{-2} (untreated sample) or 22.6 µg cm^{-2} (leached and leached + heat treated), respectively.

The CV measuring set-up consisted of a potentiostat/galvanostat connected to a ring-disk electrode system. All measurements were performed at room temperature. Preceding the catalyst's loading onto the RDE, the ring disk was polished with a 0.05 µm alumina dispersion and washed clean with ultra-pure water. The glass measuring cell was cleaned in hot diluted H_2SO_4 solution, heated again in deionized water and rinsed thoroughly with ultra-pure water to wash off all acid remains. The measurements were done in 0.1 M $HClO_4$ in ultra-pure water. As counter electrode a platinized titan rod was used. The reference electrode was a frequently calibrated hydrogen electrode and all reported potentials are in reference to RHE. The set-up was completed with a gas inlet for N_2, O_2 and H_2, which was positioned in a way that gas bubbles did not interfere or destroy the catalyst's surface on the RDE.

The first measurements were performed in nitrogen saturated electrolyte beginning with an impedance measurement (frequency 100 000 Hz, amplitude 0.01, integration time 0.127 s) to evaluate the internal resistance. Usually the intercept point in the Nyquist plot gave a resistance of about 30 Ω. Then five CV cycles were done to do a preliminary testing of the catalyst, followed by 250 fast cycles up to 1.255 V to clean the catalyst until a steady CV curve was obtained. Afterwards three analysis cycles from 0.050 V to 1.055 V with a scan rate of 50 mV s^{-1} were recorded for further data processing.

The ORR was recorded in oxygen saturated electrolyte under constant O_2 flow with a scanning range of 0.050 V to 1.055 V and a scan rate of 50 mV s^{-1}, while the electrode was constantly rotated at 1600 rpm.

The accelerated stress test was set up to determine the stability of the catalyst and consisted of 3 times 555 degradation cycles in nitrogen saturated electrolyte up to 1.400 V and a fast

scan rate of 500 mV s^{-1}. After each of the three 555 cycles an analysis scan was performed for evaluating the amount of degradation.

A summary of the measuring settings for each procedure can be seen in Table 5.3.

Table 5.3: Cyclic voltammetry measurement settings.

Procedure	Gas	Start/Stop [V]	Range [V]	Scan Rate [mV s^{-1}]	Cycles	Rotation [rpm]
Warm Up	N_2	0.455	0.050−1.050	100	5	0
Cleaning	N_2	0.455	0.050−1.255	500	250	0
ECSA Analysis	N_2	0.455	0.050−1.055	50	3	0
ORR Analysis	O_2	0.455	0.050−1.055	50	3	1600
AST	N_2	0.455	0.050−1.400	500	555	0
AST ECSA Analysis	N_2	0.455	0.050−1.055	50	3	0
Reference Potential	H_2	0.455	−0.050−1.055	50	1	1600

5.4 Data Processing

Nova software was used to integrate the area under the Pt-H desorption peak of the third CV analysis scan. To do so correctly, all currents connected to double layer formation and not to Pt-H desorption had to be deducted by drawing a new baseline as can be seen in figure 2.9(a) (dashed green line). This integrated value in W divided by the scan rate in V s^{-1} gave then the charge $Q_{H-desorb}$ in C. Together with the Pt charge constant Q_{Pt} with a literature value of $210 \cdot 10^{-6}$ C cm^{-2}, the Pt loading on the RDE in mg cm^{-2} and the area of the RDE, in this case 0.196 cm^2, the electrochemical surface area (ECSA) in cm^2 mg^{-1} was calculated according to Eq. 5.1.

$$ECSA = \frac{Q_{H-desorb}}{Q_{Pt} \cdot l_{RDE} \cdot a_{RDE}} \tag{5.1}$$

The reference potential corrected potential of the third CV analysis cycle was plotted against the current density in mA $cm^{-2}{}_{geo}$ related to the geometrical area of the RDE for comparability reasons.

The second cycle of the ORR analysis measurement was used for determining the specific current density of the catalyst in mA cm^{-2} and the mass activity in A $mg^{-1}{}_{Pt}$. In order to obtain only the currents related to the oxygen reduction and not the Pt−H, Pt−O or Pt−OH

formation and decomposition, the CV analysis cycle measured in nitrogen was deducted from the ORR curve. Furthermore the potential was corrected by the reference hydrogen potential and by the inner resistance. After the correction, the first complete positive sweep of the ORR measurement was plotted in a potential/current density ($\mathrm{mA\,cm^{-2}_{geo}}$) diagram.

The current i was determined from the corrected curve at 0.9 V, which is a typical value in literature to benchmark Pt catalysts. Together with the diffusion limited current i_{lim} at 1600 rpm, which is the lowest current of the ORR in the plateau between 0 and 0.7 V, the kinetic current i_k was calculated according to the equation for mass-transport correction (see Eq. 5.3), which is a transformed version of Eq. 5.2.

$$\frac{1}{i} = \frac{1}{i_k} \cdot \frac{1}{i_{diff}} \tag{5.2}$$

$$i_k = \frac{i_{diff} \cdot i}{i_{diff} - i} \tag{5.3}$$

The specific current density (SCD) of the catalyst in $\mathrm{mA\,cm^{-2}}$ was calculated via normalization of the current i_k, determined from equation 5.3 with the total platinum area on the RDE. This area in turn is determined by dividing the measured charge $Q_{H-desorb}$ with the platinum charge constant Q_{Pt} ($210 \cdot 10^{-6}\,\mathrm{C\,cm^{-2}}$) (Eq. 5.4).

$$SCD = \frac{i_k}{\frac{Q_{H-desorb}}{Q_{Pt}}} \tag{5.4}$$

In order to obtain the mass activity (MA) of the catalyst in $\mathrm{A\,mg^{-1}_{Pt}}$, the current i_k was divided by the total platinum mass on the RDE, which is determined by multiplying the area of the RDE with the platinum loading (Eq. 5.5).

$$MA = \frac{i_k}{l_{RDE} \cdot a_{RDE}} \tag{5.5}$$

The so called Tafel plot was obtained by plotting the GDE area normalized i_k from Eq. 5.3 logarithmically against the potentials from 0.85 V to 0.95 V. i_k is thereby not only calculated with the measured current i at 0.9 V but with the values from the whole potential range. The Tafel slope, which corresponds to the factor b in the Tafel equation (see Eq. 2.6 on page 13) was determined by a linear fit in the range of 0.88 V to 0.96 V in the Tafel plot.

Information about the stability of the catalyst was determined by calculating the relative decrease of the ECSA in percent after each of the three stress test runs (each 555 cycles) using

equation 5.6. As with the initial ECSA the Pt−H desorption peak of the third ECSA analysis scan was integrated in order to obtain $Q_{H-desorb}$ and the corresponding degraded $ECSA_{AST}$ for all three cycles.

$$Degradation[\%] = \frac{ECSA_{initial} - ECSA_{AST}}{ECSA_{initial}} \cdot 100 \tag{5.6}$$

5.5 Fuel Cell Testing

For HT-PEM fuel cell testing a 10 x 10 cm PtFe/C cathode catalyst layer was manufactured by the synthesis route described in section 5.2.1 using the impregnation solution no. 8 (see Table 5.1). Following the reduction process, the catalyst sheet was post-treated by H_2SO_4 leaching and heat-treatment at 240 °C (ramped with 5 °C min^{-1}, held for 1 h).

After the manufacturing of the PtFe/C cathode catalyst layer, it was sent to elcomax GmbH München, who performed the HT-PEM fuel cell test. There a membrane electrode assembly (MEA) was manufactured. For this, the synthesized PtFe/C cathode catalyst (Pt loading of 1.0 mg cm^{-2}) layer was doped with phosphoric acid. Together with a standard anode Pt catalyst layer and a polybenzimidazole (PBI) membrane, both provided by elcomax GmbH München, the cathode layer was hot pressed into a MEA at 150 °C.

The test was performed in a single cell with an active area of 50 cm^2 at 160 °C. The flow rates through the serpentine channel flow field was controlled with mass flow controllers. As anode gases either H_2 (3.0, Westfalen AG) or synthetic reformate (76% H_2, 1.2% CO and 22.8% CO_2, Westfalen AG) was used with the stoichiometry of 1.2. The cathode side was supplied with air with a stoichiometry of 2.0.

With this set-up, polarization curves under H_2 and reformate gas as the anode gases were recorded. The power density was calculated by multiplying the voltages with the respective current density.

6 References

[1] *International Energy Outlook 2013*. U.S. Energy Information Administration (EIA), July 2013.

[2] T.F. Stocker et al. "IPCC, 2013: Summary for Policymakers". In: *Climate Change 2013: The Physical Science Basis, Contribution of Working Group I to the Fifth Assessment Report of the Intergovernmental Panel on Climate Change*. Cambridge, United Kingdom and New York, NY, USA: Cambridge University Press, Oct. 2013.

[3] A. Boudghene Stambouli. "Fuel cells: The expectations for an environmental-friendly and sustainable source of energy". In: *Renewable and Sustainable Energy Reviews* 15.9 (Dec. 2011), pp. 4507–4520.

[4] Annett Rabis, Paramaconi Rodriguez, and Thomas J. Schmidt. "Electrocatalysis for Polymer Electrolyte Fuel Cells: Recent Achievements and Future Challenges". In: *ACS Catalysis* 2.5 (May 4, 2012), pp. 864–890.

[5] Johnson Matthey Plc. *Platinum Today - The world's leading authority on platinum group metals*. URL: `http://www.platinum.matthey.com/prices/price-charts` (visited on 03/30/2014).

[6] Ermete Antolini, Jose R.C. Salgado, and Ernesto R. Gonzalez. "The stability of Pt–M (M=first row transition metal) alloy catalysts and its effect on the activity in low temperature fuel cells". In: *Journal of Power Sources* 160.2 (Oct. 2006), pp. 957–968.

[7] Ifan E. L. Stephens et al. "Understanding the electrocatalysis of oxygen reduction on platinum and its alloys". In: *Energy & Environmental Science* 5.5 (2012), p. 6744.

[8] *PEM fuel cell electrocatalysts and catalyst layers: fundamentals and applications*. In collab. with Jiujun Zhang. London: Springer, 2008. 1137 pp.

[9] Jianlu Zhang et al. "PEM Fuel Cell Fundamentals". In: *Pem Fuel Cell Testing and Diagnosis*. Elsevier, 2013, pp. 1–42.

[10] Nguyen Viet et al. “Novel Pt and Pd Based Core-Shell Catalysts with Critical New Issues of Heat Treatment, Stability and Durability for Proton Exchange Membrane Fuel Cells and Direct Methanol Fuel Cells”. In: *Heat Treatment - Conventional and Novel Applications*. Ed. by Frank Czerwinski. InTech, Sept. 26, 2012.

[11] Y. Shao-Horn et al. “Instability of Supported Platinum Nanoparticles in Low-Temperature Fuel Cells”. In: *Topics in Catalysis* 46.3 (Nov. 27, 2007), pp. 285–305.

[12] Jianlu Zhang et al. “The Effects of Temperature on PEM Fuel Cell Kinetics and Performance”. In: *Pem Fuel Cell Testing and Diagnosis*. Elsevier, 2013, pp. 121–141.

[13] Hubert A. Gasteiger et al. “Activity benchmarks and requirements for Pt, Pt-alloy, and non-Pt oxygen reduction catalysts for PEMFCs”. In: *Applied Catalysis B: Environmental* 56.1 (Mar. 2005), pp. 9–35.

[14] Jianlu Zhang et al. “High temperature PEM fuel cells”. In: *Journal of Power Sources* 160.2 (Oct. 2006), pp. 872–891.

[15] Jianlu Zhang et al. “High-Temperature PEM Fuel Cells”. In: *Pem Fuel Cell Testing and Diagnosis*. Elsevier, 2013, pp. 243–282.

[16] Shuo Chen et al. “Platinum-Alloy Cathode Catalyst Degradation in Proton Exchange Membrane Fuel Cells: Nanometer-Scale Compositional and Morphological Changes”. In: *Journal of The Electrochemical Society* 157.1 (2010), A82.

[17] Gang Liu et al. “Studies of performance degradation of a high temperature PEMFC based on H3PO4-doped PBI”. In: *Journal of Power Sources* 162.1 (Nov. 2006), pp. 547–552.

[18] V. R. Stamenkovic et al. “Improved Oxygen Reduction Activity on Pt3Ni(111) via Increased Surface Site Availability”. In: *Science* 315.5811 (2007), pp. 493–497.

[19] Ifan E. L. Stephens et al. “Tuning the Activity of Pt(111) for Oxygen Electroreduction by Subsurface Alloying”. In: *Journal of the American Chemical Society* 133.14 (Apr. 13, 2011), pp. 5485–5491.

[20] J. Greeley et al. “Alloys of platinum and early transition metals as oxygen reduction electrocatalysts”. In: *Nature Chemistry* 1.7 (Sept. 23, 2009), pp. 552–556.

[21] Anand Udaykumar Nilekar and Manos Mavrikakis. “Improved oxygen reduction reactivity of platinum monolayers on transition metal surfaces”. In: *Surface Science* 602.14 (July 2008), pp. L89–L94.

[22] J. K. Nørskov et al. “Origin of the Overpotential for Oxygen Reduction at a Fuel-Cell Cathode”. In: *The Journal of Physical Chemistry B* 108.46 (Nov. 2004), pp. 17886–17892.

[23] Vojislav R. Stamenkovic et al. “Trends in electrocatalysis on extended and nanoscale Pt-bimetallic alloy surfaces”. In: *Nature Materials* 6.3 (Feb. 18, 2007), pp. 241–247.

[24] Marc T. M. Koper. “Structure sensitivity and nanoscale effects in electrocatalysis”. In: *Nanoscale* 3.5 (2011), p. 2054.

[25] Chao Wang et al. “Monodisperse Pt3Co nanoparticles as electrocatalyst: the effects of particle size and pretreatment on electrocatalytic reduction of oxygen”. In: *Physical Chemistry Chemical Physics* 12.26 (2010), p. 6933.

[26] A.R. Malheiro, J. Perez, and H.M. Villullas. “Surface structure and electronic properties of Pt-Fe/C nanocatalysts and their relation with catalytic activity for oxygen reduction”. In: *Journal of Power Sources* 195.10 (May 2010), pp. 3111–3118.

[27] Vojislav Stamenkovic et al. “Changing the Activity of Electrocatalysts for Oxygen Reduction by Tuning the Surface Electronic Structure”. In: *Angewandte Chemie* 118.18 (Apr. 28, 2006), pp. 2963–2967.

[28] Vojislav R. Stamenkovic et al. “Effect of Surface Composition on Electronic Structure, Stability, and Electrocatalytic Properties of Pt-Transition Metal Alloys: Pt-Skin versus Pt-Skeleton Surfaces”. In: *Journal of the American Chemical Society* 128.27 (July 2006), pp. 8813–8819.

[29] J. K. Nørskov et al. “Towards the computational design of solid catalysts”. In: *Nature Chemistry* 1.1 (Apr. 2009), pp. 37–46.

[30] Takako Toda et al. “Enhancement of the Electroreduction of Oxygen on Pt Alloys with Fe, Ni, and Co”. In: *Journal of The Electrochemical Society* 146.10 (1999), p. 3750.

[31] V. Stamenković et al. “Surface Composition Effects in Electrocatalysis: Kinetics of Oxygen Reduction on Well-Defined Pt $_3$ Ni and Pt $_3$ Co Alloy Surfaces”. In: *The Journal of Physical Chemistry B* 106.46 (Nov. 2002), pp. 11970–11979.

[32] Markus Nesselberger et al. “The Particle Size Effect on the Oxygen Reduction Reaction Activity of Pt Catalysts: Influence of Electrolyte and Relation to Single Crystal Models”. In: *Journal of the American Chemical Society* 133.43 (Nov. 2, 2011), pp. 17428–17433.

[33] Chao Wang et al. “Design and Synthesis of Bimetallic Electrocatalyst with Multilayered Pt-Skin Surfaces”. In: *Journal of the American Chemical Society* 133.36 (Sept. 14, 2011), pp. 14396–14403.

[34] L. Dubau et al. “Further insights into the durability of Pt3Co/C electrocatalysts: Formation of hollow Pt nanoparticles induced by the Kirkendall effect”. In: *Electrochimica Acta* 56.28 (Dec. 2011), pp. 10658–10667.

[35] Li-Jun Wan et al. “In situ STM imaging of surface dissolution and rearrangement of a Pt–Fe alloy electrocatalyst in electrolyte solution”. In: *Chemical Communications* 1 (2002), pp. 58–59.

[36] Takako Toda, Hiroshi Igarashi, and Masahiro Watanabe. “Enhancement of the electrocatalytic O2 reduction on Pt-Fe alloys”. In: *Journal of Electroanalytical Chemistry* 460.1 (1999), pp. 258–262.

[37] A.R. Malheiro, J. Perez, and H.M. Villullas. “Dependence on composition of electronic properties and stability of Pt–Fe/C catalysts for oxygen reduction”. In: *Journal of Power Sources* 195.21 (Nov. 2010), pp. 7255–7258.

[38] Ioannis Spanos et al. “Investigating the activity enhancement on PtxCo1-x alloys induced by a combined strain and ligand effect”. In: *Journal of Power Sources* 245 (2014), pp. 908–914.

[39] Arthur R. Malheiro, Joelma Perez, and H. Mercedes Villullas. “Well-Alloyed PtFe/C Nanocatalysts of Controlled Composition and Same Particle Size: Oxygen Reduction and Methanol Tolerance”. In: *Journal of The Electrochemical Society* 156.1 (2009), B51.

[40] Chao Wang et al. “Rational Development of Ternary Alloy Electrocatalysts”. In: *The Journal of Physical Chemistry Letters* 3.12 (June 21, 2012), pp. 1668–1673.

[41] W. Yuan, K. Scott, and H. Cheng. “Fabrication and evaluation of Pt-Fe alloys as methanol tolerant cathode materials for direct methanol fuel cells”. In: *Journal of Power Sources* 163.1 (Dec. 2006), pp. 323–329.

[42] Yannick Garsany, Irwin L. Singer, and Karen E. Swider-Lyons. “Impact of film drying procedures on RDE characterization of Pt/VC electrocatalysts”. In: *Journal of Electroanalytical Chemistry* 662.2 (Nov. 2011), pp. 396–406.

[43] Carl H Hamann and Wolf Vielstich. *Elektrochemie*. Weinheim: Wiley-VCH, 2005.

[44] Yannick Garsany et al. “Experimental Methods for Quantifying the Activity of Platinum Electrocatalysts for the Oxygen Reduction Reaction”. In: *Analytical Chemistry* 82.15 (Aug. 2010), pp. 6321–6328.

[45] K.J.J. Mayrhofer et al. “Measurement of oxygen reduction activities via the rotating disc electrode method: From Pt model surfaces to carbon-supported high surface area catalysts”. In: *Electrochimica Acta* 53.7 (Feb. 2008), pp. 3181–3188.

[46] Shuo Chen et al. “Origin of Oxygen Reduction Reaction Activity on PtCo Nanoparticles: Atomically Resolved Chemical Compositions and Structures”. In: *The Journal of Physical Chemistry C* 113.3 (2009), pp. 1109–1125.

[47] A.S. Aricò et al. “Performance and degradation of high temperature polymer electrolyte fuel cell catalysts”. In: *Journal of Power Sources* 178.2 (Apr. 2008), pp. 525–536.

[48] Christoph Grimmer. “Activity and Stability Enhancement of Platinum Cobalt Catalysts for HTPEM Fuel Cells”. PhD thesis. Graz: Technische Universität Graz, Feb. 2013. 72 pp.

[49] Dennis van der Vliet et al. “On the importance of correcting for the uncompensated Ohmic resistance in model experiments of the Oxygen Reduction Reaction”. In: *Journal of Electroanalytical Chemistry* 647.1 (Aug. 2010), pp. 29–34.

[50] Huimin Wu et al. “Pt1-xCox nanoparticles as cathode catalyst for proton exchange membrane fuel cells with enhanced catalytic activity”. In: *Materials Chemistry and Physics* 124.1 (Nov. 2010), pp. 841–844.

7 List of Figures

8 List of Tables